Ultrasonic spray pyrolysis and electroless deposition for the synthesis of nanostructured metal/carbon microspheres

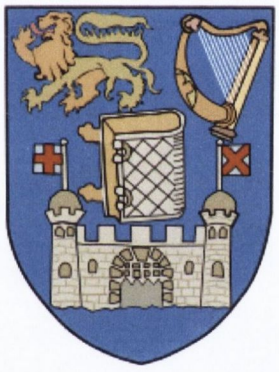

A thesis submitted to the University of Dublin for the degree of Doctor of Philosophy

by

Paul Duffy B. A. (Mod.)

Under the supervision of Dr. Paula Colavita

Declaration

I declare that this thesis has not been submitted as an exercise for a degree at this or any other university and it is entirely my own work. I agree to deposit this thesis in the University's open access institutional repository or allow the library to do so on my behalf, subject to Irish Copyright Legislation and Trinity College Library conditions of use and acknowledgement.

I declare that this report details entirely my own work. Due acknowledgements and references are given to the work of others where appropriate.

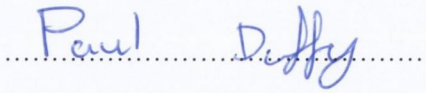

Paul Duffy B. A. (Mod.)

Acknowledgements

I would like to thank Dr Paula Colavita for her support and patience over the course of my PhD studies. She has been a constant guide in the implementation of this study and was always available for discussions and insight.

I would also like to thank Dr Laura Soldi and Dr Dilushan Jayasandra the post docs in my group. Both gave immense help in the implementation of my studies, practically and via ideas and suggestions. I would also like to acknowledge all the support given to me by the other members of our research group. I would also like to acknowledge all the people at the chemistry department, without training on instrumentation and background support and service, none of this would have been possible. In particular, I would like to thank Dr Manuel Ruether for much help over the years. Also Dr Karsten Rode for help in data interpretation.

I would also like to acknowledge Dr Kevin Metz, our coffee lovin American collaborator. Many good talks were to be had on the way to SEM sessions.

Lastly, I would like to thank family and friends for supporting me throughout my PhD studies.

I gratefully acknowledge support from the Environmental Protection Agency, Ireland (EPA, Ireland) for funding, Trinity College Dublin for its start up funds and the School of Chemistry.

Abstract

The objective of this work is to synthesis various nano-metallic carbon microsphere composite materials for environmental and catalytic applications. Ultrasonic spray pyrolysis and electroless deposition techniques were used to achieve this. The composites materials were characterised and their subsequent activity was demonstrated.

Carbon microsphere particle of various morphology and surface area have been synthesised using ultrasonic spray pyrolysis. These particles were characterised using a combination of Raman spectroscopy, scanning electron microscopy (SEM), BET adsorption, FTIR and zeta potential measurements. SEM imagery determined the shape and morphology of the various carbon materials. It was demonstrated via Raman spectroscopy that carbon microparticles were graphitic in nature, however, FTIR and Zeta potential measurements demonstrated the presence of carboxylate groups on the carbon microsphere surface.

It was demonstrated that carbon microspheres synthesised using ultrasonic spray pyrolysis had controllable size by leveraging precursor concentrations. This was confirmed via a combination of SEM images and dynamic light scattering experiments. FTIR and zeta potential experiments demonstrated that CM surfaces display chemistry which allowed the grafting of differing chemical moieties via diazonium chemistry.

Using electroless deposition techniques, nanoparticles of three metal materials were nucleated and grown on the CM surfaces. In particular, Palladium and silver metal were nucleated on the CM surface from metal salts using coffee as a green reducing agent, at room temperature. Metal composite materials were characterised using a combination of SEM, x-ray diffraction (XRD), energy dispersive x-ray spectroscopy (EDS) and thermogravimetric analysis (TGA). XRD confirmed the metallic nature of the

particles observed via SEM. Using TGA and EDS in combination, mass loadings where estimated with Ag/C and Pd/C mass ratios of (13.5 ± 1.5)% and (7.4 ± 1.0)% w/w, respectively.

Suzuki coupling reaction confirmed the viability of the Pd/C composite material for catalytic applications. Ag/C composite reduced 4-nitrophenol, achieving reaction rates which are comparible to other support silver nanoparticles in the literature.

Iron and iron oxide nanoparticles were synthesis at the carbon microsphere surface using electroless deposition. The reported electroless deposition approach produced a composite Fe/FeO_x/carbon microsphere with nanoparticles of a narrowly dispersed size. A combination of X-ray powder diffraction (XRD) and X-ray absorption spectroscopies (EXAFS and XANES) was used in order to determine the structure and composition of the Fe/FeO_x/carbon microspheres. Microspheres were found to display (14 ± 1)% iron content (w/w), whereby (12 ± 3)% of iron atoms were present as metallic iron and the remaining as maghemite (Fe_2O_3). Finally, we show that the removal capacity of Fe/FeOx/carbon microspheres for Cr(VI) is (20 ± 2) mg $g^{-}1$ and that the maximum surface density for Cr adsorbates is (60 ± 6) mg m^{-2}, thus suggesting that these are promising materials for the removal of water pollutants from aqueous solution.

Table of Contents

List of figures

List of Tables

Chapter 1

Introduction

1.1 Background

Contrary to popular belief, nanotechnology is not exclusive to modern science. Colloidal gold nanoparticles (NPs) was discovered over 2500 years ago [1]. Colloidal gold was used to make ruby glass and to imbue ceramics with colour, and these applications are still continuing now. This was due to the intense colours that colloidal noble metal NPs make. Also, of interest was the use of colloidal gold NPs in the diagnosis of syphilis in the middle age. A method which remained active and in use until the 20^{th} century, a method which also happens to be completely unreliable [2]. However, even though NPs had been around for this long, it wasn't until Faraday showed that the intense colour is due to metallic gold in colloidal form that understanding of the potential applications of NPs was slowly realised [3,4]. In 1908, Mie explained the phenomena of coloured colloidal metal particles by solving Maxwell's equations for the absorption and scattering of electromagnetic radiation by spherical metallic particles [5]. Interestingly, these two results indicated that metal nano materials had different optical properties than their bulk counterparts, know as quantum size effects [6,7]. These effects are not a result of a scaling factor but are directly due to the size and shape of the NPs. In fact, many of the properties of bulk materials change when the material is put into the nano scale. Optical, physical, chemical and electrical properties have all been observed to be size dependent for various materials [8,9]. Effects such as this due to small particle size led to great curiosity about the properties of nano-sized materials in the scientific community which has continued to this day. In fact, in the last ten years alone, the number of research papers on nanomaterials has grown exponentially in numbers, indicating that research into nanomaterials is still a relatively new and unexplored field [10]. This research is driven by a desire to discover materials with new properties and to understand the science behind quantum size effects for differing materials in the hope of discovering interesting applications which could be of significant benefit to society.

All of this research has led to many potential applications of nanomaterials from biological, optics, environmental and catalysis. However, in this report we will be focusing on the nanomaterials which have potential catalytic and environmental applications.

Synthesis of nanomaterials and particle is generally achieved in two ways, top down approach and bottom up approach. Top down approach general involved the use of photochemistry or electron beam lithography for etching surfaces to create nanometre sized structures and features [11,12]. This route for synthesis of nanomaterials will not be discussed or reported on herein.

The bottom up approach generally involves the nucleation of particles followed by subsequent growth of the particle. The easiest method for obtaining NPs using this approach is utilising wet chemistry. This type of synthesis starts off with molecular precursor solutions. Typically, they include a metal salt, a reducing agent and a support/stabilising agent. Generally the metal ion in solution is reduced to its metallic state, forming a particle. This process is governed by the theory of nucleation and growth[6]. Other methods for bottom up synthesis have been achieved. Specifically, methods involving spray pyrolysis [13,14], electro-deposition [15,16], and sol gel. Synthesis of nanostructures using electro-deposition is discussed in more detail in section 1.5.3.

1.2 Introduction to supported nanoparticle systems

1.2.1 Stabilising agents

In synthesizing metal NPs for any application two of the biggest issues are the size of the NPs and the stability of NPs in solutions. As many of the unique properties of NPs are size and shape dependent [17], controlling these parameters in synthesis can be

crucial for many potential applications. Instability in solution comes from attractive forces between NPs in solutions such as van der vaals forces and magnetic interactions [18]. If bottom up methods are being used there must be a mechanism for restricting growth of the NP to keep it in the desired size range. This is generally achieved using stabilising agents and support materials.

By introducing stabilising support materials, it is possible to manipulate the size of NPs during synthesis and NP stability post synthesis. The stabilisation of NPs is generally of the form electrostatic, steric, electrosteric and use of ligands. Stabilisers work by creating an energetic barrier to counteract the van der Waals and magnetic (magnetic materials) attractions between nanoparticles. This can be used to inhibit growth in the nucleation processes of NP formation or to stabilise dispersions of NPs in solution [6].

1.2.1.1 Polymers

An example of a steric stabilising agent is polymers. Figure 1.1 shows poly(N-vinyl-2-pyrrolidone) (PVP) and poly(2,5-dimethylphenylene oxide) (PPO) which are used in the synthesis of NPs because they behaves as steric and ligand stabiliser.

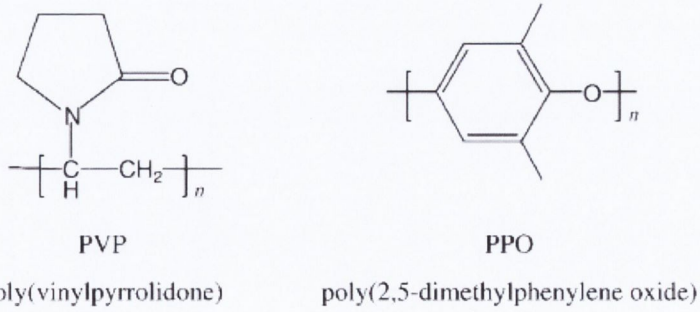

PVP

poly(vinylpyrrolidone)

PPO

poly(2,5-dimethylphenylene oxide)

Figure 1.1: Two polymer families used as metal NP supports for catalysis [10].

Using this polymer, Pt, Pd and Rh NPs have been synthesised which catalyse olefin and benzene hydrogenation reactions [19]. However throughout the literature a vast number of polymers have been used in NP synthesis, including, polyacrylic acid [20], oligosaccharides, polyethylene glycol [21], chitosan [22] and polyelectrolyte films [23].

1.2.1.2 Dendrimers

Dendrimers have also seen use for supporting and stabilising metal NPs. Metals NPs such as Cu, Au, Pt, Pd, Fe, Ag and Ru have all been synthesis using dendrimers [24-26]. Dendrimers behave similarly to polymers in that they encapsulate the NP, particularly if hetero atoms of the metal are located in the dendrimer interior. The branches of the dendrimer than control access to the nucleating NP, which limits growth and stabilise the NP in solution. Figure 1.2 shows the strategy pioneered by crook et al for the synthesis of NPs via encapsulation in a dendrimer [24].

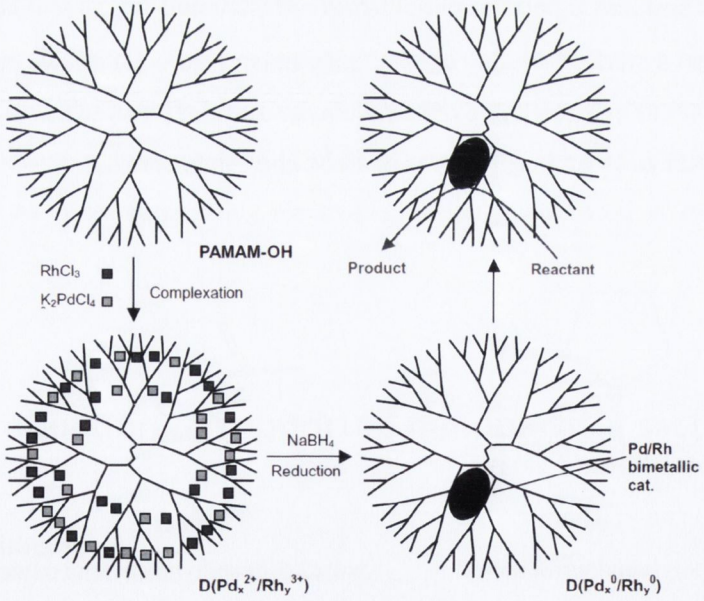

Figure 1.2: Nanoparticles encapsulated in PAMAM or PPI dendrimers: complexation of a metal cation, then reduction to metal(0) by $NaBH_4$, and aggregation giving the NPs inside the

dendrimer. Specifically, the preparation of dendrimer-encapsulated bimetallic NPs is shown [27].

Other forms of stabilisers used include Ligands [1], micro-emulsions, reverse micelles [9] and surfactants [10]. These methods achieve stabilisation and controlled particle growth by using the same principles and concepts as examples previously outlined above. Hence, they will not be discussed further in this report. In general, use of some form of stabilising agents is essential in order to obtain nano-sized materials using a bottom up solution based approach.

1.2.1.3 Solid support systems

In recent literature, there is an increasing number of reports on NPs are being placed on various solid supports are being published. The benefit of anchoring NPs at a solid surface is in creating synergies between the desirable properties of metal nanoparticles and those of the solid matrix. For example, ease of removal and handling of NP system from a reaction medium and minimisation of particle aggregation are significant benefits. Another application for solid supports is in use as a template material in order to achieve structured nanomaterials. For example, Kim et al[28], nucleated a Pd film by heat treating silica spheres which had palladium acetylacetonate (Pd(acac)2) adsorbed at the silica surface. Subsequent etching of the silica sphere with HF left a hollow Pd metal sphere nanostructure. Menon et al utilised a polycarbonate membrane as a template for synthesis Au nanoelectrodes in the 10 nm size range [29]. In the literature, most solid supports take the form of metal oxides. For example, Si [30], Al [31], and Ti [32] oxides have all been utilised as solid support materials for NPs. Oxide supports are not exclusive to these metals and will not be discussed further in this report.

More recently, carbon materials have seen use as solid support materials for NPs. The use of carbon materials for nanoparticle support offers a number of highly attractive

properties for a variety of applications. Carbon provides many advantages over polymeric or inorganic supports due to its resistance to corrosion and its relatively good biocompatibility. Furthermore, the surface chemistry of carbon can be fine tuned to display different chemical groups that can for instance impart charge, regulate basicity/acidity, control wetting behaviour or prompt biological recognition. Finally, carbon supports can be designed to display a large specific surface area which can be leveraged for the delivery of large loads of nanoparticles or small molecules. For this reason, there have recently been increased efforts aimed at developing new methodologies for the controlled deposition/embedding of metal nanoparticles at carbon scaffolds [33-36].

Examples of carbon materials for nanomaterials support include: Metz et al. have synthesized nano-structured composite Au/C and Pt/C electrodes for energy storage and conversion applications, by using vertically aligned carbon nano-fibres (VACNF) as a scaffold [36-38].

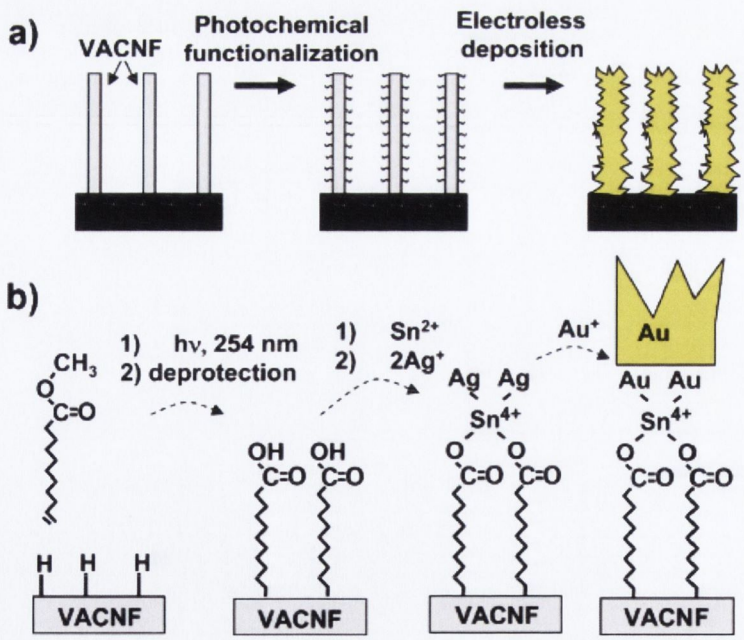

Figure 1.3: (a) Schematic illustration of the steps involved in the functionalization of carbon nanofibers and subsequent proceudure for electroless deposition. (b) Chemical transformations involved in the nanofiber modification [39].

Figure 1.3 shows how Metz and co workers used solid carbon fibres as a support for growing gold nano - electrodes. The carbon fibres act as a template in order to shape the growth of the metal nano material. Lipshuts et al [40] use of Nickel on Charcoal Ni/C as an Inexpensive Heterogeneous Catalyst for Cross-Couplings between Aryl Chlorides and Organometallics is another example of a carbon supported nanomaterial.

1.3 Applications of nanoparticles

In this section the use of nanomaterials with regard to specific areas will be discussed. The first part will consist of nanomaterials for catalysis. A short review will be given, followed by application in catalysis for the two metals utilised in this report for catalysis. Part two will consist of nanomaterials for environmental applications. Herein, a review will be given of current technologies in environmental remediation, the potential of nanomaterials and the problems with implementation of nanomaterials in this field.

1.3.1 Nanomaterials for catalysis

The use of nanomaterials in catalysis was first recorded in the 19th century. Notable examples included the use of silver NPs (AgNP) in photography and the use of platinum NPs (PtNP) in the decomposition of hydrogen peroxide [41]. However, research continued with progress made in the 20th century where progress in catalysis was made for a number of metal NPs. Hirai et al demonstrated that gold nanoparticles (AuNP) catalysed olefin hydrogenation [42,43]. Palladium nanoparticles (PdNP) found important applications as catalysts in heck C-C bond coupling [15,44]. Over the years of research many metal NPs have been shown to have catalytic properties, however, of particular importance has been the discovery of Pd catalysts in the formation of C-C

bonds, making it possible to functionalise olefins and aromatics in a facile manner. Moreover, significant numbers of diverse reactions can be catalysed by various noble metal NPs, which are beyond the scope of this report [10]. For this report, we will utilise Pd and Ag metals in order to achieving the aims stated previously (see section 1.6.2).

1.3.1.1 Palladium nanomaterials in catalytic application

Pd nanoparticles find important applications as catalysts in hydrogenation and C-C bond forming reactions like Suzuki, Heck and Sonogashira coupling [45,46]. However, problems with catalyst recovery meant the presence of undesired metal contaminants in the end products in reactions for which it was utilised. Immobilization of catalytically active Pd nanoparticles at solid supports facilitates catalyst removal and reaction work up when compared to homogeneous catalysts. Therefore, much effort has recently been devoted to developing anchoring protocols for Pd nanoparticles, thus forming a composite material that preserves the original catalytic properties while improving handling and reaction work up. Mei et al used polyelectrolyte brushes and core shell micro gels in order to encapsulate the PdNP [26]. Other groups have used carbon nanotubes [47,48], silica [49,50], polyelectrolyte films [51], and graphite [52]. Importantly the results obtained by many of these researchers indicate that the nature of the support used can have an impact on the rate of catalysis. This is not unexpected as catalysis is a heterogeneous process. Therefore, any material that blocks access to the NP surface has the potential to reduce catalytic performance.

1.3.1.2 Silver nanomaterials in catalytic application

Silver nanoparticles have numerous applications, e.g. in fuel cells [53-55], optical sensors and biological applications [56-58]. However, many of these applications rely on the ability to control nanoparticle aggregation and consequent loss of function, while at the same time preserving their chemical, optical and/or catalytic properties

[25,59]. In order to achieve this goal, several research groups have focused on developing supported Ag nanoparticles, e.g. Ag/polysaccharide [22,58], Ag/graphene [60] or Ag/ polymer [61] nanocarrier composites, improving transport and modulating aggregation of Ag nanoparticle active centres. Similar to Pd particles, the support system chosen can influence the rate of catalysis for AgNPs. This means selection of an appropriate support material can be essential for utilising NPs in catalytic applications in an efficient manner (See section 1.4).

1.3.2 Nanomaterials for environmental applications

1.3.2.1 Review of the issues

Due to growing awareness about the effects of subsurface contaminants in soil and groundwater in the environment, increased research and funding is being allocated to the area of remediation technologies and contaminant management. Remediation of these contaminated sites is a vast and complex area. The vast scale of the problem is exasperated by the sheer number of contaminated sites. In the US there are over 1500 of what are known as superfund sites and on average a superfund site costs approximately $25 million to remediate. Recently, it has been estimated that Ireland has close to 2000 contaminated sites due old industries, unmanaged spills and other inadequate waste management procedures [62-64]. The complexity of the problem is in the variety of contaminants at the sites, variety of contaminant source type and locations and also the variety of soils and porous media which contain the contaminants. This means different methods for clean up have to be identified in a case by case basis. Traditional approaches to treating soil and groundwater contaminants have used pump and treat or containment methods via permeable reactive barriers (PRB). These methods have serious disadvantages. The biggest disadvantage is the cost associated with them. Installing, managing and removing PRB's is quite expensive and can be uneconomical for widespread use. Secondly, some

contaminant sources in deep aquifers and under buildings may not be accessible to these technologies [65-67].

In recent times the use of nanotechnology for environmental remediation has been investigated [18]. Nanoparticles have a higher proportion of atoms near or at the surface. This leads to a higher proportion of atoms having dangling bonds and higher surface energy. This means that these atoms have a much greater capacity to promote adsorption and to interact with other molecules in order to compensate for the excess surface energy. Already, nanomaterials exhibiting promising reactive and adsorptive properties have been successfully used in water purification and environmental remediation. Nanoparticles also have the advantage of being able to penetrate intraparticle pores of soils. This enables their use in slurry reactors for the remediation of contaminated soils and sediments. Currently, the most promising nanomaterials for environmental applications, considering remediation potential and cost are metallic iron and iron oxides.

1.3.2.2 Metallic iron as remediation material

In recent literature, metallic iron Fe^0 has been reported as a successful remediating agent for environmental contaminants. Fe^0 is an excellent electron donor in water, resulting in its use as a reductive agent that can effectively remediate contaminants such as inorganic anions [68-73], heavy metals [74-76], and organohalides [77-79]. In fact, metallic iron has been so versatile in remediating many different varieties of contaminants that an explosion of work has occurred in this research field in the last fifteen years.

Fe^0 particles can be described using a core shell model as shown in Figure 1.4. The core mainly consists of Fe whereas the outer shell consists of a mixture of Fe^{3+} and Fe^{2+} due to oxidation of the Fe^0 metallic core.

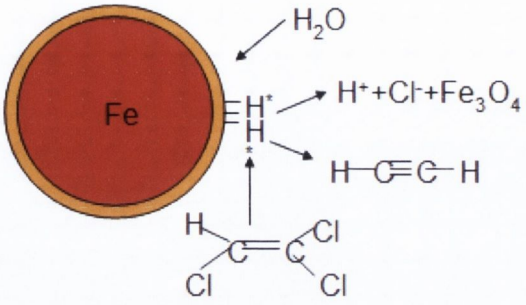

Figure 1.4: Core shell model of an iron nanoparticle[18]

Figure 1.4 also shows two of the main proposed mechanisms by which remediation occurs on particle surfaces in the case of a chlorinated organic compound. Several contaminants adsorb on the oxide phase layer, oxidation of the Fe^0 in the particle provides electrons for the reduction of trichloroethylene. The Fe^0 core shrinks and is used up in the reaction. The particles are no longer active as a reducing agent once all the Fe^0 is oxidised.

The reduction reaction induced by Fe^0 is a heterogeneous process. This means that the total number of active surface sites which can interact with contaminants depends only on the total surface area. Hence, by increasing the surface to volume ratio (*i.e* decreased particle size), the efficiency and performance of the reductive processes can be improved. This led to the interest in nano-sized Fe^0 across research groups for environmental remediation. Interestingly, Fe^0NPs have displayed properties unique to nano-sized particle indicating there are some quantum size effects. For example, nano iron can dechlorinate polychlorinated biphenyl compounds (PCBs) at room temperature and pressure whereas granular iron does not [80-82]. However, many reduction due to iron don't have any quantum effects. In fact when normalised for surface area, reaction rate constants are similar for many reductive reactions [65,80,83].

For successful use of nanomaterials at a large scale, cost effective and robust methods must be developed for production since environmental applications demand large

quantities of remediation agents at low costs. Fe^0NPs have been synthesised using a wide range of methods: decomposition of iron pentacarbonyl in organic solvents [84,85], electrodeposition of ferrous salts , vacuum sputtering [86], reduction of goethite and hematite particles with hydrogen gas at high temperature [87] and finally, reduction of Fe[III] and Fe[II] salts using sodium borohydride or other reducing agents. [88]. This last method uses aqueous based chemistry and is facile to implement. Fe^0 is prepared according to the following reaction:

$$4Fe^{3+} + 3BH_4^- + 9H_2O \rightarrow 4Fe^0 \downarrow + 3H_2BO_3^- + 12H^+ + 6H_2 \uparrow \quad \text{(eqn 1.1)}$$

When the reaction is carried out under constant stirring and under inert atmosphere it leads to the formation of polydisperse polycrystalline or amorphous nanoparticles, with diameters typically in the range 20-100 nm. This equation shows the basic reaction that occurs. It is important to note that many side reactions can occur here. For example, the reaction shown in eqn 1.2 below occurs

$$BH_4^- + 2H_2O \rightarrow BO_2^- + 4H_2 \quad \text{(eqn 1.2)}$$

This reaction causes the formation of the basic Metaborate ion. This can then lead to the formation of metallic Boron in our mixture via the half reaction

$$BO_2^- + 2H_2O + 3e^- \rightarrow B + 4OH^- \quad \text{(eqn 1.3)}$$

These reactions result in a Fe/B alloy. The Boron concentration of this alloy is sensitive to parameters such as pH, temperature, concentration of salts and the ratio of the ferrous salt to the Borohydride salt. These have been investigated in detail in the previous literature [89-91].

The increased performance of Fe^0 offers many advantages: (a) improved performance results in lower costs; (b) more effective remediation and (c) reduced production of

harmful by-product intermediates. Finally, nano-materials can be delivered directly into the contaminant source via injections of aqueous slurries containing nanoparticles. This injection capability enables sites such as contaminated deep aquifers to be selectively targeted [92-96], thus replacing costly excavations. However, a number of challenges must be overcome in order to implement nano Fe^0 in the field; key issues that represent an obstacle are outlined in the following section.

1.3.2.3 Challenges in the implementation of iron nanoparticles

The first problem with the implementation of Fe^0 is the presence of competing oxidants. In a contaminant plume Fe^0 not only reacts with contaminants but also with dissolved oxygen and water according to the following reactions:

$$2Fe^0_{(s)} + O_{2(g)} + 4H^+ \rightarrow 2Fe^{2+}_{(aq)} + 2H_2O_{(l)} \qquad \text{(eqn 1.4)}$$

$$2Fe^0_{(s)} + 2H_2O_{(l)} \rightarrow 2Fe^{2+}_{(aq)} + H_{2(g)} + 2OH^-_{(aq)} \qquad \text{(eqn 1.5)}$$

Fe^{2+} can be further oxidised to Fe^{3+} according to:

$$4Fe^{2+}_{(s)} + O_{2(g)} + 4H^+ \rightarrow 4Fe^{2+}_{(aq)} + 2H_2O_{(l)} \qquad \text{(eqn 1.6)}$$

These side reactions can affect the service lifetime of Fe^0 NPs based PRB's, since contaminant plumes can take several years to completely pass a point in the subsurface. This problem has therefore restricted the use of Fe^0 as a remediation agent to groundwater, which is a relatively anoxic medium. However, the biggest problem with further application of FeNPs is in its mobility in porous media [97].

Recent studies on bare unsupported Fe^0NPs have reported limited mobility in saturated porous media [97]. Transport distances of a few centimetres or inches have been reported. This poor mobility is caused via two mechanisms, successful filtration by soil matrices and aggregation of the Fe particles. Based on filtration theory there is

an optimum size range for particles in order to minimise their filtration by porous media. In general, smaller particles below 100-200nm are susceptible to adsorptive processes on soil grains. Electrostatic interactions, London van der vaals forces and Brownian motion all influence these absorptive processes; consequently, soil pH, ionic strength and water composition can all affect adsorption. Larger particles, above 1-2 μm in size, are susceptible to filtration via sedimentation instead. Therefore, depending on soil type and water conditions, the optimum range for particles to minimise filtration is in the order of 100 nm to 2000 nm. This means that Fe^0NPs are vulnerable to filtration by adsorptive process due to their small size [98,99].

The colloidal chemistry and ferromagnetic behaviour of Fe particles results in severe aggregation. Aggregation prevents particle flow through porous media such as soils after aggregates reach a few microns in diameter. Lowry et al have reported DLS measurements taken at different times after sonication of Fe^0 NPs dispersions, and observed that average particle size increased within 15 min from 100nm to 5000nm in a concentrated solution. Even following attempts to prepare extremely dilute dispersions it was not possible to reduce aggregation.

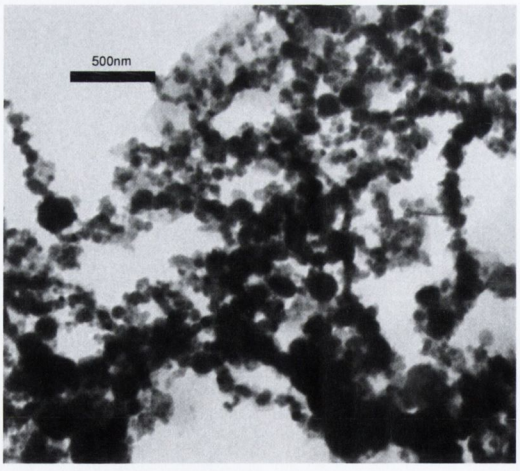

Figure 1.5: TEM showing FeNP aggregates; Scale bar 500 nm

Even with an improvement in the result and measurement quality, the aggregation appears to be still occurring. Figure 1.5 shows a TEM of FeNPs synthesised in our laboratory using the borohydride method outlined above. Large micrometer sizes chain like aggregates can be observed. Aggregation such as this, also have the effect of lowering reactivity due to subsequent lowering of specific surface area available for adsorption and reaction [100,101].

In recent times, many groups have tried to overcome these difficulties by use of surface modification and supports for the NPs. Surface modifications have involved the use of surfactants [99,102], carbohydrates [103,104], polyelectrolytes [105] and tri-block copolymers [106]. These approaches aim at preventing aggregation via electrostatic repulsion and/or steric stabilisation. In literature these methods have been shown to improve transport in model soils and to minimise agglomeration, increasing stability. However, this often occurs at a loss in reactivity since these surface modifications have the effect of simultaneously blocking and inhibiting reactive sites on the particle.

Therefore, there is a need for new methods and technologies that can improve transport and mobility in soils for the nanoparticles. These new technologies should aim to improve transport and mobility whilst maintaining the advantage of increased reactivity gained from using FeNP.

1.3.2.4 Iron oxide in environmental applications

Higher surface energies of metal oxide nanoparticles due to surface to volume ratio's make iron oxide nanoparticle more prone to adsorption effects. A large body of work has been done on adsorption mechanisms of ions onto metal oxide surfaces [107,108]. Surface hydroxides in metal oxides have a double pair of electrons with a dissociable H atom which allows ions to react in solutions and form complexes at the oxide surface

[18,109]. Iron oxide NPs have also been used in environmental applications. Iron oxide NPs have been shown to be effective in the adsorption of Cr(VI) [110], arsenite and arsenate [111].

1.4 Support material for Ag, Pd and Fe/Fe_xO_y particles

Porous carbon microspheres (CMs) are particularly advantageous for nanoparticle support since they can leverage all of the advantages of carbon materials while displaying a high specific surface and good transport/delivery properties, as recently shown by work in our group [112]; however, their applications as nanoparticle support have remained relatively unexplored.

Carbon materials displayed chemistry which facilitates the functionalisation of the surface [113-115]. This facilitates a mechanism for changing surface charge and chemistry in CMs. Surface charge modification can be measured using the zeta potential for suspended particles.

1.4.1 Zeta potential and surface charge

Most particles in a colloidal suspension have a surface charge associated with them. This surface charge attracts an excess of a counterion species in solutions. This leads to the formation of two layers of opposite charge. These are the fixed surface charge and the diffuse charge from ions in solution. This is known as the electrical double layer (EDL) [116].

In more complex models, there is also what is known as the Stern layer. This is represented by the location between the surface and the locus of counterions. The Stern layer is sometimes broken into two regions: the inner Helmholtz layer (IHL) and

the outer Helmholtz layer (OHL) to distinguish between moieties that have a chemical affinity for the surface as well as coulombic interactions. Tangential fluid flow along a charged surface can be caused by applying an electric field. It has been shown that a thin layer of fluid sticks to the surface. This is known as the hydrodynamically stagnant layer. This layer goes from the surface to some distance d^{ek} where a slip plane is assumed to exist and fluid flow begins again. This assumption means that the volume contained within the slip plane is constant and hence the space charge for everything within the slip plane is constant as everything is assumed to be static within the slip plane. The potential at this point is defined as the zeta potential. The slip plane will be a greater than or equal to distance from the surface as the OHL.

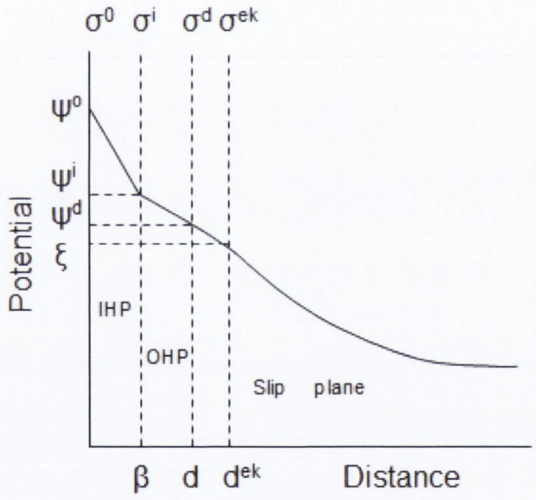

Figure 1.6: Model of Surface charges and potentials. All potentials are defined with respect to the potential in the bulk solution.

Figure 1.6 demonstrates a model depicting all these layers. It is accepted that the zeta potential is defined by the nature of the surface, its charge, the electrolyte concentration, pH and the nature of the solvent. These being fixed, the zeta potential should be a fixed number [116].

The zeta potential is not directly measurable but its value can be obtained via electrokinetic measurements coupled to modelling of the electrophoretic mobility. In our studies we have used this approach to investigate the effects of surface functionalisation on CM surface charge using methods outlined in section 2.2.2.

1.4.2 Carbon microsphere with controllable size

Also, CMs were synthesised utilising ultrasonic spray pyrolysis. Using this method CMs with varying porosity have been synthesised[117]. This method also has potential to control CM size (See section 2.1.1). Tufenkji–Elimelech model predicts that filtration effects are minimized for particles between 0.1 μm and 1 μm in diameter [118]; therefore, CM size is in the optimal range for applications requiring delivery of nanoparticles through porous matrices. These CM offer a vast range of selectivity and tuneable parameters for potential applications as a nanomaterials support. If control of CMs used for support can be gained, they would provide an excellent support for Ag, Pd and Fe/Fe_xO_y NP's in all there potential applications.

In this work, we report on the use of an electroless deposition approach to synthesize metal nanoparticle/carbon composite microspheres. Electroless deposition is used to synthesis Ag, Pd and Fe/Fe_xO_y at CM surfaces. The next section contains a review of electroless deposition and some information regarding applications of the technique for synthesis of nano materials.

1.5 Introduction to Electroless Deposition

1.5.1 Basics of Electroless Deposition

Electroless deposition (ED) is a heterogeneous electrochemical process which involves the growth of a metal on a substrate via a catalyzed chemical reduction of aqueous metal ions onto the substrate surface. It is generally accepted that ED proceeds via two simultaneous electrochemical processes: i) The cathodic reduction of the metal ion at a catalytic surface, ii) The anodic oxidation of the reductant in solution: However, unlike conventional electrodeposition processes, the catalytic oxidation of reductants is the source of electrons for reductive deposition of metals. Figure 1.7 shows a schematic representation of three types of ED occurring on a substrate. The reducing agent donates an electron, allowing the aqueous metallic salt to be reduced and deposited on the catalytic substrate in metallic form [119-122].

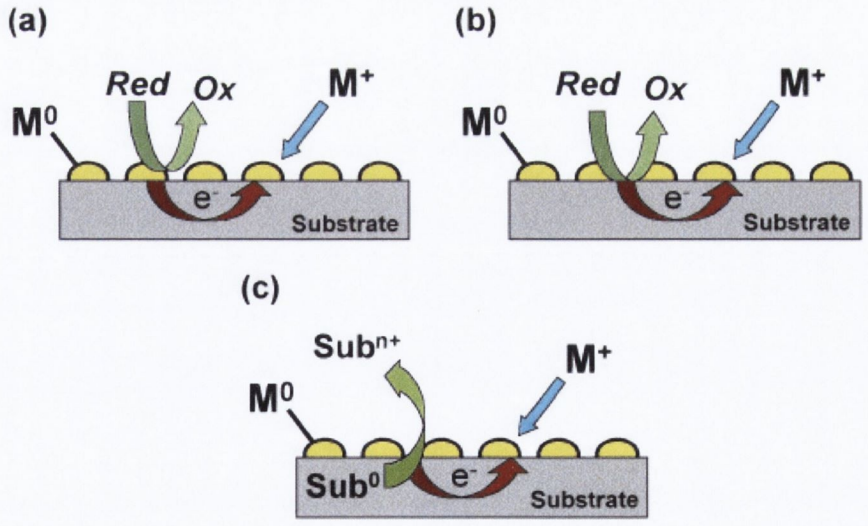

Figure 1.7: Electroless deposition processes: (a) Autocatalytic: The reduced noble metal serves as the catalyst for further reduction of the metal salt by the external reducing agent. (b) Substrate catalyzed: The substrate surface catalyzes the reduction of the metal salt by the reducing agent (c) Galvanic displacement: The surface serves as the reducing agent and electron source for reduction of the metal salt: [123].

In most ED processes, continued metallic deposition will occurs due to the deposited metallic sites having their own catalytic properties. The term autocatalytic is often used to describe this property of ED. Once ED is initiated, the autocatalytic property coupled with an electron source via the reducing agent, mean ED reactions can continue without the need of an external power supply. Subsequently, ED processes can be achieved on non-conducting and semi conductor surfaces, provided catalytically active regions are available to initiate autocatalysis

1.5.2 Key requirements for ED

In order to achieve successful ED, several key requirements are necessary:

i) Chemistry of bath such that the oxidation potential of the reductant is less noble than the reverse potential of the metal being deposited.

ii) Chemistry of bath such that the kinetics for the electron transfer between reducing agent and metal ions in solution are slow

iii) A catalytically active surface to accelerate the rate of metal ion reduction at the surface, initiating autocatalysis.

i) and ii)

Requirements i) and ii) ensure that the ED baths of this type are **thermodynamically unstable but kinetically stable.** This is essential because otherwise the metal ion would be reduced in the bulk solution via homogeneous electron transfer. Homogenous electron transfer is unwanted for many reasons. Firstly, it decreases the lifetime of ED baths due to homogenous reduction occurring simultaneously with heterogeneous reduction. This results in the metal ions and reducing agent being

consumed at a faster rate, leading to increased decomposition times for deposition solutions. This has cost implication due to the waste of expensive metal salts. Secondly, homogeneous reduction can result with precipitation of unwanted chemical compounds such as metal hydroxides. Precipitates can interfere with the heterogeneous process resulting in different physical and chemical properties of the deposited layer. Precipitates can also lead to bath failure by inhibiting catalytic activity.

To prevent this, many baths contain additives other than a source of metal ions and a reducing agent. Additives are used primarily to change the thermodynamic behaviour and kinetic behaviour of solutions in order to satisfy the criteria of having kinetic stability whilst retaining enough thermodynamic instability to ensure catalytic reductive deposition. Complexing agents are typically used to achieve this. These agents can act as either stabiliser agents or reaction inhibitors. Stabilisers can act as buffer agents to the formation of metal hydroxides and other metal precipitates which facilitate bath failures. Complexing agents are also used to inhibit rates of reaction by lowering the redox potential between the anodic and cathodic reaction, increasing kinetic stability.

Lowering the redox potential has also been achieved by controlling the pH of the bath. The potential of many of the reducing agents has been shown to be dependent on the solution pH [124,125]. However, for reactions that result in the formation or consumption of H^+ ions or OH^- ions, addition of a pH buffer may be necessary to ensure successful plating.

With all these possible additives, many ED procedures have very complex chemistry and are quite simply, not well understood [126-128]. It is well documented in literature that minor changes in bath composition can alter the physical properties of the metal deposits produced through ED [129]. This indicates that properties such as

resistivity, rate of deposition, morphology and purity depend on many factors besides the identity of the metal being deposited [129,130].

iii)

Requirement iii) ensures that ED can be initiated at the required surface. A catalyst accelerates the rate of metal ion reduction, allowing the heterogeneous reduction to vastly outpacing any competing homogeneous reduction. In this way, metal ions are reduced only at the surface, and the surface becomes coated with the desired metal. It has been shown that generally ED proceeds on metals that can be used in hydrogenation and dehydrogenation catalytic processes. This drastically minimises the type of surfaces which can be directly deposited on. However, researchers have overcome this using several methods. Maoz et al developed a method of nanofabrication using a conductive atomic force microscopy tip to locally oxidize the terminal CH_3 groups of a self-assembled monolayer [131]. The oxidized sites were then used for the selective self-assembly of vinyl terminated silanes, which drove the deposition of metals. Researchers have also achieved ED by nucleating catalytic metallic seed particles onto many surface types via ion exchange and galvanic coupling methodologies [38]. The seed particles act as an initiation site for the autocatalytic process. This allows ED to be implemented on surfaces such as glass, polymers, ceramics and other non metallic and non conductive surfaces [39].

1.5.3 Uses of electroless deposition for nanoparticle synthesis

Electroless deposition/plating has emerged as an effective method for growing nano structures and nanoparticles on supporting materials. Cu, Ag, Pd, Pt, Au and Co metals have all have nanostructures synthesised via ED [38,132-135]. This has been achieved by utilising several different methods, most of which use one or both of the following concepts

i) Controlling where the growth occurs

ii) Modifying rate of growth by modifying reaction kinetics.

i)

The use of growth templates to control shape and limit the uncontrolled growth has been shown to be effective. As ED is a bottom up method for producing nanostructures, use of a template will shape, guide and limit the growth, enabling the production of nanowires, nanotubes and nanoparticles. Notably, Martin and co-workers carried out work on the use of electroless deposition for the decoration of poly carbonate filter membrane supports (10 -30 nm pores) with noble metal nanostructures [29].

More recently, Metz et al. have shown that these methodologies can be used to deposit Au and Pt nanoparticles at nano-structured carbon supports [36,38,135]. The approach here typically consists of a spontaneous reduction of the metal at a surface that is **selectively** activated via formation of catalytic seed particles; plating only occurs at these catalytic centres.

ii)

Modifying the kinetics of an ED process has been achieved several ways. Firstly, Yoshino et al [136] has demonstrated that by using additives with inhibiting and accelerating effects it is possible to fill nanometre scale trenches in ultra – large scale integration interconnect technology. This approach involves controlling the kinetics of deposition by modifying bath chemistry. This approach is manipulating the rate of electron donation as a mechanism for controlling deposition rates.

Typically, heterogeneous kinetics is characterised by mass transport through solution, adsorption on the catalytic surface, mass transport on the surface and desorption of the reaction products. As ED is a heterogeneous process, electron transfer is not the only property which influences rate. Therefore, the dispersion and size of metal

nanoparticles can be, in principle, controlled by mass transport to the surface of the nano-structured solid support [137]. Figure 1.8 shows a schematic of the ED process. In general, it is desirable to reach step 3 and obtain a uniform metallic layer.

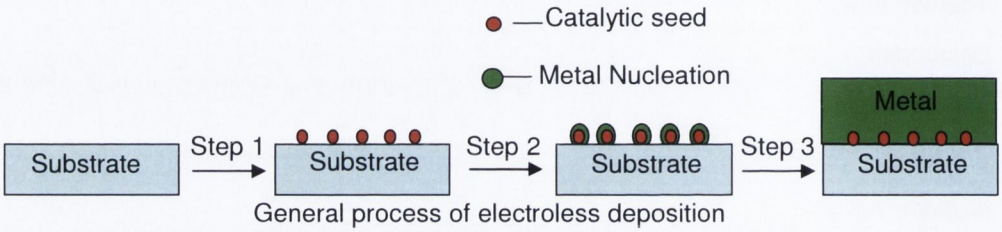

Figure 1.8: Schematic showing electroless deposition utilising catalytic seed particles

However, in this work we are going to combine controlled catalytic seed activation with controlled mass transport in order to achieve limited growth. This method will result in the ED process halting at step 2 in figure 1.8 and the synthesis of nucleated nanoparticles instead of a conformal metallic layer.

1.6 Aims of this work

1.6.1 Carbon microspheres

The first goal of this work is to synthesis CMs utilising USP and methods pioneered by Skrabalak et al [117,138]. Once synthesis, we will try to demonstrate the viability of the CM's as a support material for nanoparticle growth. In order to do this we will (a) demonstrate that CMs synthesised via USP have controllable size, important for transport in porous media and biological systems. (b) It will be shown that CMs display typical carbon surface chemistry by performing some simple diazonium grafting reactions. A surface charge change after functionalisation would indicate that it will be possible to modify the surface charge and chemistry of CMs, important for tailoring transport properties in various environments [97].

1.6.2 Synthesis of new Pd/C and Ag/C composite materials using Electroless deposition

Using CMs, Pd and Ag NPs will be nucleated at the carbon surface via green electroless deposition protocols. It will be shown that protocols used by metz et al, can be used to achievable nucleated catalytic seed particles at the CM surface. It will be shown that growth of catalytic seed particles at the CM surface is crucial to obtaining these composites and determining the size of the nanoclusters grown at the CM surface. Recently Varma and coworkers reported on the use of coffee or tea as a reducing agent for green synthesis of metal nanoparticles [139,140]. In this work we report on the use of coffee as a low-cost, green reagent for electroless deposition at room temperature. We have leveraged the reduction potential of coffee in order to grow Pd and Ag nanoparticles at the surface of porous carbon microspheres (CM) synthesized via ultraspray pyrolysis. It is also shown that both of the Pd and Ag composite materials are catalytically active by performing Suzuki coupling and 4-nitrophenol reduction respectively.

1.6.3 Synthesis of $Fe/Fe_xO_y/C$ composite materials using Electroless deposition

Using CMs, Fe/Fe_xO_y NPs will be nucleated at the carbon surface via electroless deposition. Metallic catalytic seed particles will be used again to start the ED process on the carbon surface in order to achieve this goal. Multiply ED protocols will be tried in order to achieve the synthesis of this composite material. It will be shown that it is possible to control the size of NPs grown at the CM surface using electroless deposition protocols by nakanishi et al [141]. Subsequently, it is demonstrated that the new composite material is very highly responsive towards the removal of Cr(VI) from aqueous solutions.

References

(1) Daniel, M.-C.; Astruc, D. *Chemical Reviews* **2004**, *104*, 293.

(2) Parida, U. K.; Nayak, P. *World* **2012**, *1*, 10.

(3) Kerker, M. *Journal of Colloid and Interface Science* **1985**, *105*, 297.

(4) Faraday, M. *Philosophical Transactions of the Royal Society of London* **1857**, *147*, 145.

(5) Mie, G. *Ann. Phys* **1908**.

(6) Burda, C.; Chen, X.; Narayanan, R.; El-Sayed, M. A. *Chemical Reviews* **2005**, *105*, 1025.

(7) Kamat, P. V. *The Journal of Physical Chemistry B* **2002**, *106*, 7729.

(8) Kamat, P. V.; Meisel, D. *Semiconductor nanoclusters--physical, chemical, and catalytic aspects*; Elsevier Amsterdam, 1997.

(9) El-Sayed, M. A. *Accounts of Chemical Research* **2001**, *34*, 257.

(10) Astruc, D.; Lu, F.; Aranzaes, J. R. *Angewandte Chemie International Edition* **2005**, *44*, 7852.

(11) Shenhar, R.; Rotello, V. M. *Accounts of Chemical Research* **2003**, *36*, 549.

(12) Jager, E. W.; Smela, E.; Inganäs, O. *Science* **2000**, *290*, 1540.

(13) Xia, B.; Lenggoro, I. W.; Okuyama, K. *Advanced Materials* **2001**, *13*, 1579.

(14) Okuyama, K.; Lenggoro, I. W.; Tagami, N.; Tamaki, S.; Tohge, N. *Journal of Materials Science* **1997**, *32*, 1229.

(15) Reetz, M. T.; Helbig, W. *Journal of the American Chemical Society* **1994**, *116*, 7401.

(16) Reetz, M. T.; Quaiser, S. A. *Angewandte Chemie International Edition in English* **1995**, *34*, 2240.

(17) Ahmadi, T. S.; Wang, Z. L.; Green, T. C.; Henglein, A.; El-Sayed, M. A. *Science-New york then Washington* **1996**, 1924.

(18) Lowry, G. V. . *M. R. Wiesner and J.-Y. Bottero, McGraw-Hill, New York,* **2007**, 297.

(19) Andres, R. P.; Bielefeld, J. D.; Henderson, J. I.; Janes, D. B.; Kolagunta, V. R.; Kubiak, C. P.; Mahoney, W. J.; Osifchin, R. G. *Science* **1996**, *273*, 1690.

(20) Demir, M. M.; Gulgun, M. A.; Menceloglu, Y. Z.; Erman, B.; Abramchuk, S. S.; Makhaeva, E. E.; Khokhlov, A. R.; Matveeva, V. G.; Sulman, M. G. *Macromolecules* **2004**, *37*, 1787.

(21) Pillai, U. R.; Sahle-Demessie, E. *Journal of Molecular Catalysis A: Chemical* **2004**, *222*, 153.

(22) Murugadoss, A.; Chattopadhyay, A. *Nanotechnology* **2008**, *19*, 015603.

(23) Gröschel, L.; Haidar, R.; Beyer, A.; Reichert, K.-H.; Schomäcker, R. *Catalysis letters* **2004**, *95*, 67.

(24) Crooks, R. M.; Zhao, M.; Sun, L.; Chechik, V.; Yeung, L. K. *Accounts of Chemical Research* **2001**, *34*, 181.

(25) Esumi, K.; Isono, R.; Yoshimura, T. *Langmuir* **2004**, *20*, 237.

(26) Mei, Y.; Lu, Y.; Polzer, F.; Ballauff, M.; Drechsler, M. *Chemistry of Materials* **2007**, *19*, 1062.

(27) Chung, Y.-M.; Rhee, H.-K. *Journal of Molecular Catalysis A: Chemical* **2003**, *206*, 291.

(28) Kim, S.-W.; Kim, M.; Lee, W. Y.; Hyeon, T. *Journal of the American Chemical Society* **2002**, *124*, 7642.

(29) Menon, V. P.; Martin, C. R. *Analytical Chemistry* **1995**, *67*, 1920.

(30) Lang, H.; Maldonado, S.; Stevenson, K. J.; Chandler, B. D. *Journal of the American Chemical Society* **2004**, *126*, 12949.

(31) Schauermann, S.; Hoffmann, J.; Johánek, V.; Hartmann, J.; Libuda, J.; Freund, H. J. *Angewandte Chemie International Edition* **2002**, *41*, 2532.

(32) Guczi, L.; Beck, A.; Horvath, A.; Koppány, Z.; Stefler, G.; Frey, K.; Sajo, I.; Geszti, O.; Bazin, D.; Lynch, J. *Journal of Molecular Catalysis A: Chemical* **2003**, *204*, 545.

(33) Schaetz, A.; Zeltner, M.; Stark, W. J. *ACS Catalysis* **2012**, *2*, 1267.

(34) Tang, S.; Vongehr, S.; Meng, X. *Journal of Materials Chemistry* **2010**, *20*, 5436.

(35) Zhang, P.; Shao, C.; Zhang, Z.; Zhang, M.; Mu, J.; Guo, Z.; Liu, Y. *Nanoscale* **2011**, *3*, 3357.

(36) Metz, K. M.; Tse, K. Y.; Baker, S. E.; Landis, E. C.; Hamers, R. J. *Chemistry of Materials* **2006**, *18*, 5398.

(37) Metz, K. M.; Goel, D.; Hamers, R. J. *The Journal of Physical Chemistry C* **2007**, *111*, 7260.

(38) Metz, K. M.; Colavita, P. E.; Tse, K.-Y.; Hamers, R. J. *Journal of Power Sources* **2012**, *198*, 393.

(39) Metz, K. M.; Tse, K.-Y.; Baker, S. E.; Landis, E. C.; Hamers, R. J. *Chemistry of Materials* **2006**, *18*, 5398.

(40) Lipshutz, B. H.; Blomgren, P. A. *Journal of the American Chemical Society* **1999**, *121*, 5819.

(41) Bradley, J., S. *Clusters and Colloids: Chaper 6*, 1994.

(42) Hirai, H.; Nakao, Y.; Toshima, N. J. *Macromol. Sci. Chem. A* **1979**, *13*, 727.

(43) Hirai, H.; Nakao, Y.; Toshima, N. J. *Macromol. Sci. Chem. A* **1978**, *12*, 1117.

(44) Reetz, M. T.; Breinbauer, R.; Wanninger, K. *Tetrahedron letters* **1996**, *37*, 4499.

(45) Lamblin, M.; Nassar - Hardy, L.; Hierso, J. C.; Fouquet, E.; Felpin, F. X. *Advanced Synthesis & Catalysis* **2010**, *352*, 33.

(46) Balanta, A.; Godard, C.; Claver, C. *Chemical Society Reviews* **2011**, *40*, 4973.

(47) Karousis, N.; Tsotsou, G.-E.; Evangelista, F.; Rudolf, P.; Ragoussis, N.; Tagmatarchis, N. *The Journal of Physical Chemistry C* **2008**, *112*, 13463.

(48) Mahouche Chergui, S.; Ledebt, A.; Mammeri, F.; Herbst, F. d. r.; Carbonnier, B.; Ben Romdhane, H.; Delamar, M.; Chehimi, M. M. *Langmuir* **2010**, *26*, 16115.

(49) Domínguez-Quintero, O.; Martínez, S.; Henríquez, Y.; D'Ornelas, L.; Krentzien, H.; Osuna, J. *Journal of Molecular Catalysis A: Chemical* **2003**, *197*, 185.

(50) Gude, K.; Narayanan, R. *The Journal of Physical Chemistry C* **2011**, *115*, 12716.

(51) Kidambi, S.; Bruening, M. L. *Chemistry of Materials* **2005**, *17*, 301.

(52) Scheuermann, G. M.; Rumi, L.; Steurer, P.; Bannwarth, W.; Mülhaupt, R. *Journal of the American Chemical Society* **2009**, *131*, 8262.

(53) Coutanceau, C.; Demarconnay, L.; Lamy, C.; Léger, J.-M. *Journal of Power Sources* **2006**, *156*, 14.

(54) Varcoe, J. R.; Slade, R. C.; Wright, G. L.; Chen, Y. *The Journal of Physical Chemistry B* **2006**, *110*, 21041.

(55) Singh, P.; Buttry, D. A. *The Journal of Physical Chemistry C* **2012**, *116*, 10656.

(56) Haes, A. J.; Hall, W. P.; Chang, L.; Klein, W. L.; Van Duyne, R. P. *Nano Letters* **2004**, *4*, 1029.

(57) Haes, A. J.; Stuart, D. A.; Nie, S.; Van Duyne, R. P. *Journal of fluorescence* **2004**, *14*, 355.

(58) Sanpui, P.; Chattopadhyay, A.; Ghosh, S. S. *ACS Applied Materials & Interfaces* **2011**, *3*, 218.

(59) Chi, Y.; Zhao, L.; Yuan, Q.; Yan, X.; Li, Y.; Li, N.; Li, X. *Journal of Materials Chemistry* **2012**, *22*, 13571.

(60) Bong, S.; Kim, Y.-R.; Kim, I.; Woo, S.; Uhm, S.; Lee, J.; Kim, H. *Electrochemistry communications* **2010**, *12*, 129.

(61) Zhang, Y.; Wang, L.; Tian, J.; Li, H.; Luo, Y.; Sun, X. *Langmuir* **2011**, *27*, 2170.

(62) Brogan, J.; Carty, G.; Crowe, M.; Leech, B. *eds. C. Ferguson and H. Kasamas, LQM Press, Nottingham, UK,* **1999**.

(63) Brogan, J.; Crowe, M.; Carty, G. *Environmental Protection Agency* **2002**.

(64) Ferber, U.; Grimski, D. *CLARINET Report, Austria,* **2002**.

(65) Wilkin, R. T.; Su, C. M.; Ford, R. G.; Paul, C. J. *Environmental Science & Technology* **2005**, *39*, 4599.

(66) O'Hannesin, S. F.; Gillham, R. W. *Ground Water* **1998**, *36*, 164.

(67) Blowes, D. W.; Ptacek, C. J.; Benner, S. G.; McRae, C. W. T.; Bennett, T. A.; Puls, R. W. *Journal of Contaminant Hydrology* **2000**, *45*, 123.

(68) Gandhi, S.; Oh, B. T.; Schnoor, J. L.; Alvarez, P. J. J. *Water Research* **2002**, *36*, 1973.

(69) Puls, R. W. *Environmental Protection Agency, Vienna, Austria,* **1998**.

(70) Westerhoff, P.; James, J. *Water Research* **2003**, *37*, 1818.

(71) Xiong, Z.; Zhao, D. Y.; Pan, G. *Water Research* **2007**, *41*, 3497.

(72) Sohn, K.; Kang, S. W.; Ahn, S.; Woo, M.; Yang, S. K. *Environmental Science & Technology* **2006**, *40*, 5514.

(73) Choe, S.; Chang, Y. Y.; Hwang, K. Y.; Khim, J. *Chemosphere* **2000**, *41*, 1307.

(74) Cantrell, K. J.; Kaplan, D. I.; Wietsma, T. W. *Journal of Hazardous Materials* **1995**, *42*, 201.

(75) Ponder, S. M.; Darab, J. G.; Mallouk, T. E. *Environmental Science & Technology* **2000**, *34*, 2564.

(76) Xu, Y. H.; Zhao, D. Y. *Water Research* **2007**, *41*, 2101.

(77) Zhang, W. X. *Journal of Nanoparticle Research* **2003**, *5*, 323.

(78) Li, X. Q.; Elliott, D. W.; Zhang, W. X. *Critical Reviews in Solid State and Materials Sciences* **2006**, *31*, 111.

(79) Laine, D. F.; Cheng, I. F. *Microchemical Journal* **2007**, *85*, 183.

(80) Liu, Y.; Majetich, S. A.; Tilton, R. D.; Sholl, D. S.; Lowry, G. V. *Environmental Science & Technology* **2005**, *39*, 1338.

(81) Lowry, G. V.; Johnson, K. M. *Environmental Science & Technology* **2004**, *38*, 5208.

(82) Wang, C. B.; Zhang, W. X. *Environmental Science & Technology* **1997**, *31*, 2154.

(83) Nurmi, J. T.; Tratnyek, P. G.; Sarathy, V.; Baer, D. R.; Amonette, J. E.; Pecher, K.; Wang, C. M.; Linehan, J. C.; Matson, D. W.; Penn, R. L.; Driessen, M. D. *Environmental Science & Technology* **2005**, *39*, 1221.

(84) Elihn, K.; Otten, F.; Boman, M.; Kruis, F. E.; Fissan, H.; Carlsson, J. O. *Nanostructured Materials* **1999**, *12*, 79.

(85) Karlsson, M. N. A.; Deppert, K.; Wacaser, B. A.; Karlsson, L. S.; Malm, J. O. *Applied Physics a-Materials Science & Processing* **2005**, *80*, 1579.

(86) Kuhn, L. T.; Bojesen, A.; Timmermann, L.; Nielsen, M. M.; Morup, S. *Journal of Physics-Condensed Matter* **2002**, *14*, 13551.

(87) Uegami, M.; Kawano, J.; Okita, T.; Fujii, Y.; Okinaka, K.; K. Kakuya; Yatagai, S. *U.S. Patent Application* **2003**.

(88) Elliott, D. W.; Zhang, W.-X. *Environmental Science & Technology* **2001**, *35*, 4922.

(89) Glavee, G. N.; Klabunde, K. J.; Sorensen, C. M.; Hadjipanayis, G. C. *Inorganic Chemistry* **1995**, *34*, 28.

(90) Schlesinger, H. I.; Brown, H. C.; Finholt, A. E.; Gilbreath, J. R.; Hoekstra, H. R.; Hyde, E. K. *Journal of the American Chemical Society* **1953**, *75*, 215.

(91) Shen, J. Y.; Li, Z. Y.; Yan, Q. J.; Chen, Y. *Journal of Physical Chemistry* **1993**, *97*, 8504.

(92) Teutsch, G.; Rügner, H.; Zamfirescu, D.; Finkel, M.; Bittens, M. *Land Contam. Recl* **2001**, 128.

(93) Gavaskar, A.; Tatar, L.; Condit, W. *Port Hueneme* **2005**.

(94) Cantrell, K. J.; Kaplan, D. I. *Journal of Environmental Engineering-Asce* **1997**, *123*, 499.

(95) Quinn, J.; Geiger, C.; Clausen, C.; Brooks, K.; Coon, C.; O'Hara, S.; Krug, T.; Major, D.; Yoon, W. S.; Gavaskar, A.; Holdsworth, T. *Environmental Science & Technology* **2005**, *39*, 1309.

(96) Saleh, N.; Sirk, K.; Liu, Y. Q.; Phenrat, T.; Dufour, B.; Matyjaszewski, K.; Tilton, R. D.; Lowry, G. V. *Environmental Engineering Science* **2007**, *24*, 45.

(97) Schrick, B.; Hydutsky, B. W.; Blough, J. L.; Mallouk, T. E. *Chemistry of Materials* **2004**, *16*, 2187.

(98) Yao, K. M.; Habibian, M. M.; Omelia, C. R. *Environmental Science & Technology* **1971**, *5*, 1105.

(99) Kanel, S. R.; Nepal, D.; Manning, B.; Choi, H. *Journal of Nanoparticle Research* **2007**, *9*, 725.

(100) Beke, D. L. *Crystal Research and Technology* **1998**, *33*, 1039.

(101) Phenrat, T.; Saleh, N.; Sirk, K.; Tilton, R. D.; Lowry, G. V. *Environmental Science & Technology* **2007**, *41*, 284.

(102) Sun, Y. P.; Li, X. Q.; Zhang, W. X.; Wang, H. P. *Colloids and Surfaces a-Physicochemical and Engineering Aspects* **2007**, *308*, 60.

(103) Joo, S. H.; Zhao, D. *Chemosphere* **2008**, *70*, 418.

(104) He, F.; Zhao, D. Y. *Environmental Science & Technology* **2005**, *39*, 3314.

(105) Hydutsky, B. W.; Mack, E. J.; Beckerman, B. B.; Skluzacek, J. M.; Mallouk, T. E. *Environmental Science & Technology* **2007**, *41*, 6418.

(106) Saleh, N.; Phenrat, T.; Sirk, K.; Dufour, B.; Ok, J.; Sarbu, T.; Matyiaszewski, K.; Tilton, R. D.; Lowry, G. V. *Nano Letters* **2005**, *5*, 2489.

(107) Al-Abadleh, H. A.; Grassian, V. H. *Surface Science Reports* **2003**, *52*, 63.

(108) Arai, Y.; Elzinga, E. J.; Sparks, D. L. *Journal of Colloid and Interface Science* **2001**, *235*, 80.

(109) Cornell, R. M.; Schwertmann, U. *The iron oxides: structure, properties, reactions, occurrences and uses*; Wiley. com, 2003.

(110) Zhong, L. S.; Hu, J. S.; Liang, H. P.; Cao, A. M.; Song, W. G.; Wan, L. J. *Advanced Materials* **2006**, *18*, 2426.

(111) Dixit, S.; Hering, J. G. *Environmental Science & Technology* **2003**, *37*, 4182.

(112) Duffy, P.; Magno, L. M.; Yadav, R. B.; Roberts, S. K.; Ward, A. D.; Botchway, S. W.; Colavita, P. E.; Quinn, S. J. *Journal of Materials Chemistry* **2012**, *22*, 432.

(113) Colavita, P. E.; Streifer, J. A.; Sun, B.; Wang, X. Y.; Warf, P.; Hamers, R. J. *Journal of Physical Chemistry C* **2008**, *112*, 5102.

(114) Colavita, P. E.; Sun, B.; Tse, K. Y.; Hamers, R. J. *Journal of the American Chemical Society* **2007**, *129*, 13554.

(115) Allongue, P.; Delamar, M.; Desbat, B.; Fagebaume, O.; Hitmi, R.; Pinson, J.; Saveant, J. M. *Journal of the American Chemical Society* **1997**, *119*, 201.

(116) Delgado, A. V.; Gonzalez-Caballero, E.; Hunter, R. J.; Koopal, L. K.; Lyklema, J. *Pure Appl. Chem* **2005**, 1753.

(117) Skrabalak, S. E.; Suslick, K. S. *Journal of the American Chemical Society* **2006**, *128*, 12642.

(118) Tufenkji, N.; Elimelech, M. *Environmental Science & Technology* **2004**, *38*, 529.

(119) Ohno, I.; Wakabayashi, O.; Haruyama, S. *Journal of The Electrochemical Society* **1985**, *132*, 2323.

(120) Osaka, T.; Misato, T.; Sato, J.; Akiya, H.; Homma, T.; Kato, M.; Okinaka, Y.; Yoshioka, O. *Journal of The Electrochemical Society* **2000**, *147*, 1059.

(121) Homma, T.; Komatsu, I.; Tamaki, A.; Nakai, H.; Osaka, T. *Electrochimica Acta* **2001**, *47*, 47.

(122) Malel, E.; Mandler, D. *Journal of The Electrochemical Society* **2008**, *155*, D459.

(123) Porter, L. A.; Choi, H. C.; Ribbe, A. E.; Buriak, J. M. *Nano Letters* **2002**, *2*, 1067.

(124) Dubin, V. M.; Shacham - Diamand, Y.; Zhao, B.; Vasudev, P.; Ting, C. H. *Journal of The Electrochemical Society* **1997**, *144*, 898.

(125) Shacham-Diamand, Y.; Dubin, V.; Angyal, M. *Thin Solid Films* **1995**, *262*, 93.

(126) Patterson, J.; Ni Dheasuna, C.; Barrett, J.; Spalding, T.; O'Reilly, M.; Jiang, X.; Crean, G. *Applied surface science* **1995**, *91*, 124.

(127) Mallory, G. O.; Haydu, J. B. *American Electroplaters and Surface Finishers Society, Orlando, FL* **1990**.

(128) Sargent, A.; Sadik, O. A. *Journal of The Electrochemical Society* **2001**, *148*, C413.

(129) Sargent, A.; Sadik, O. A. *Langmuir* **2001**, *17*, 2760.

(130) Iacovangelo, C.; Zarnoch, K. *Journal of The Electrochemical Society* **1991**, *138*, 983.

(131) Maoz, R.; Frydman, E.; Cohen, S.; Sagiv, J. *Advanced Materials* **2000**, *12*, 725.

(132) Shi, Z.; Wu, S.; Szpunar, J. A. *Chemical physics letters* **2006**, *422*, 147.

(133) Shi, Z.; Wu, S.; Szpunar, J. A. *Nanotechnology* **2006**, *17*, 2161.

(134) Wang, F.; Arai, S.; Endo, M. *Electrochemistry communications* **2004**, *6*, 1042.

(135) Metz, K. M.; Goel, D.; Hamers, R. J. *Journal of Physical Chemistry C* **2007**, *111*, 7260.

(136) Yoshino, M.; Nonaka, Y.; Sasano, J.; Matsuda, I.; Shacham-Diamand, Y.; Osaka, T. *Electrochimica Acta* **2005**, *51*, 916.

(137) De Leo, M.; Pereira, F.; Moretto, L.; Scopece, P.; Polizzi, S.; Ugo, P. *Chemistry of Materials* **2007**, *19*, 5955.

(138) Skrabalak, S. E.; Suslick, K. S. *Journal of Physical Chemistry C* **2007**, *111*, 17807.

(139) Moulton, M. C.; Braydich-Stolle, L. K.; Nadagouda, M. N.; Kunzelman, S.; Hussain, S. M.; Varma, R. S. *Nanoscale* **2010**, *2*, 763.

(140) Nadagouda, M. N.; Varma, R. S. *Green Chemistry* **2008**, *10*, 859.

(141) Nakanishi, T.; Masuda, Y.; Koumoto, K. *Journal of crystal growth* **2005**, *284*, 176.

CHAPTER 2

Experimental techniques

In this chapter, the theory behind some of the less well known experiment methods and techniques used in this report will be given. A background will be given for ultrasonic spray pyrolysis, dynamic light scattering and zeta potential measurements. A review of other techniques used in the report will not be given due to the ubiquitous nature of these techniques.

2.1 Review of experimental methods

2.1.1 Ultrasonic spray pyrolysis

Recent developments have shown that it is possible to achieve the synthesis of carbon microparticles by a process known as ultrasonic spray pyrolysis (USP) [1,2]. In USP a liquid precursor solution is nebulised into a mist using a high frequency piezoelectric transducer. The mist is then carried via inert or reactive gas flow to a furnace. The solvent evaporates in the furnace and the precursor decomposes thus leaving a solid particle that can be captured and isolated. Figure 2.1 shows a schematic of this process as carried out in the studies presented in the following chapters.

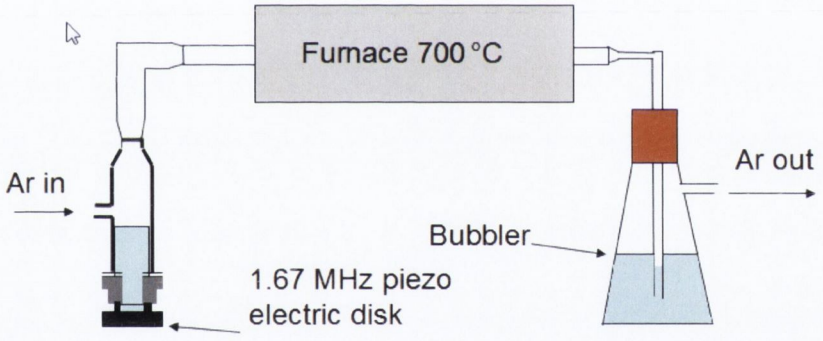

Figure 2.1: Schematic of the USP system used in our studies.

Using piezoelectric nebulisation it is possible in principle to obtain a narrowly dispersed particle size distribution [3]. The oscillations in the ultrasonic range of the piezoelectric disk cause capillary waves to form in the precursor solution. Eqn 2.1 provides a way of calculating the expected wavelength of capillary waves in a liquid reservoir:[3]

$$\lambda = \left(\frac{8\pi T}{\rho F^2} \right)^{\frac{1}{3}} \qquad (2.1)$$

Where ρ is the liquid density, T is the surface tension, F is the exciting frequency and λ is the wavelength of the capillary wave. When a wave has a large enough excitation vibration, build up in wave amplitude causes instability, resulting in wave peaks breaking loose and being expelled from the surface leading to the formation of droplets. The diameter of these droplets (D) is proportional to the capillary wavelength according to the following eqn 2.2 [3]:

$$D = 0.34\left(\frac{8\pi T}{\rho F^2}\right)^{\frac{1}{3}} \qquad \text{(eqn 2.2)}$$

The typical size dispersion of droplets generated with this method can thus be controlled by varying frequency or surface tension. These droplets can then be carried into the furnace on a stream of inert gas where the solvent evaporation and precursor decomposition can be controlled by maintaining control over furnace temperature and carrier gas flow rate.

Within the furnace each individual droplet acts as a separate reaction vessel containing limited amounts of dissolved precursor. Hence, upon decomposition, the resulting particle can only be of a limited size. Using mass balance, a given particles diameter is given by eqn 2.3 [3-5]:

$$d_p = \left(\frac{M}{\rho}\frac{D^3}{1000}C_S\right)^{\frac{1}{3}} \qquad \text{(eqn 2.3)}$$

Where M is the molecular mass, ρ is the expected density of the solid, D is the diameter of the droplet given by eqn 2.2 and C_s is the starting concentration of the precursor solution. Equations 2.2 and 2.3 indicate that control over microsphere size can be achieved in two ways: by varying piezo frequency and by varying precursor concentration.

2.2 Experimental Techniques

2.2.1 Dynamic Light Scattering (DLS)

Dynamic light scattering is an experimental technique used to determine the size of particles, typically in the submicron scale. DLS uses the Brownian motion of particles in a solution in order to estimate size; this estimation is done via the Stokes Einstein eqn 2.4 [6]:

$$d_h = \frac{kT}{3\pi\eta D} \qquad \text{(eqn 2.4)}$$

Where d_h is the hydrodynamic radius, k is Boltzmann's constant, η is the solvent viscosity, T is temperature and D is the translational diffusion coefficient. This equation means that, if the diffusion coefficient is known, it is possible to calculate the hydrodynamic radius as long as the temperature is constant and the particles are suspended in a solvent of known viscosity at this temperature. A main limitation of eqn 2.4 is that it assumes that particles are spherically shaped, so that the hydrodynamic radius is the diameter of a sphere with the same translational diffusion coefficient. Since the measured diffusion coefficient can be affected by surface structures and ions in the solvent medium, the same particle core size can yield slightly different d_h values. Also, the ionic strength of a medium affects particle diffusion speed by changing the size of the electric double layer. Surface structures affect the diffusion coefficient by varying degrees depending on their orientation and properties.

Figure 2.2 shows the basic experimental configuration of DLS measurements used for our studies of carbon microparticles. Light from a laser impinges on a dispersion of particles in a liquid and is scattered at different angles. A detector at a specific angle θ

measures the intensity of the scattered beam; the intersection of the incident and scattered beam defines the scattering volume *V*. According to the classical theory of light, the incident field can induce dipoles in the medium that oscillate at the same frequency thus creating scattering centres.

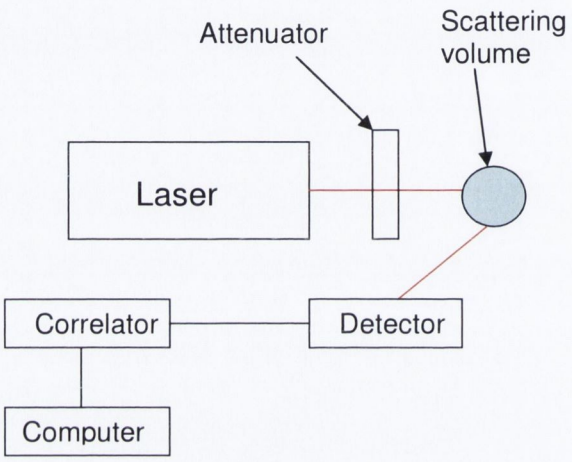

Figure 2.2: Optical setup for DLS measurements

Since the incident laser light is monochromatic and coherent the total scattered amplitude is the result of the superposition (interference) of the beams scattered by all infinitesimal volumes within *V*. If all the volumes are identical (have the same dielectric constant) it is always possible to find an infinitesimal volume that is in destructive interference with another at a scattering angle different from zero. Therefore, only forward scattering will be observed in this case, since only at zero degrees all of the beams superimpose in phase. If the scattering centres are different from each other scattered radiation is observed at all angles instead.

The amplitude scattered by a volume containing a suspension of particles depends on the dielectric constant of the dispersing liquid and on the number density, size and dielectric constant of the particles. Such a suspension is not a homogeneous medium and beams scattered by infinitesimal volumes will lead to scattering over all angles. At any instant in time the total scattered beam will depend on the particular arrangement

of the particles in space, however, Brownian motion causes the particles to move thus introducing fluctuations in the scattered amplitude. The time-scale of these fluctuations, in turn, contains information on the diffusion coefficient D and, consequently, on the hydrodynamic radius d_h of the particles. DLS determination of particle size and concentration therefore relies on extracting size, concentration and dielectric constant information from the time fluctuations of the scattered intensity. The DLS measurements in our experiments were performed at a fixed angle by using a digital correlator to process the intensity signal measured at the detector. A correlator generates the correlation function for the scattered signal which is used to extract the characteristic time scale for the observed intensity fluctuations. The normalised time auto-correlation function is given by eqn 2.5:

$$g(\tau) = \frac{\langle I(t)I(t+\tau)\rangle}{\langle I(t)\rangle^2} \qquad \text{(eqn 2.5)}$$

where I(t) is the intensity at time t to which the average value of the scattered intensity is substracted; I(t+τ) is the intensity after one sample time τ and the ‹› brackets indicate an average over all times.

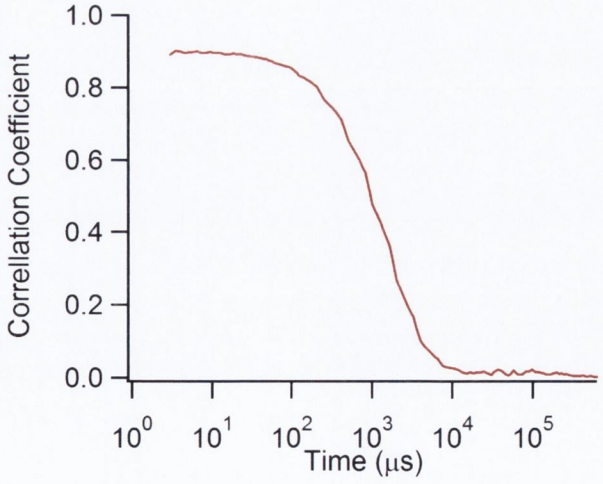

Figure 2.3: Example of an experimental correlation function

This is how the decay is collected in the instrument; Figure 2.2 gives an example of an experimental autocorrelation function. If a scattered signal from time t is compared to a signal a small time interval δt later a strong relationship can be observed; the two signals will be very similar because little particle movement has occurred over a short time. After very long delay times the particles can be very far away from their initial positions so that the two scattered intensities are also very different. Therefore, at $\tau = 0$ $g(\tau)$ should be 1 whereas at $\tau \rightarrow$ infinity the $g(\tau)$ should tend to zero. For a monodisperse sample this decay can then be made to fit with an exponential model according to eqn 2.6:

$$g(\tau) = A[1 + B\exp(-2\Gamma\tau)] \qquad \text{(eqn 2.6)}$$

Where A is the baseline of the function, B is the intercept of the function and Γ is the decay constant. The diffusion coefficient can be derived from the decay constant according to eqn 2.7:

$$\Gamma = D\left(\left(\frac{4\pi n}{\lambda_0}\right)Sin\left(\frac{\theta}{2}\right)\right)^2 \qquad \text{(eqn 2.7)}$$

where n is the refractive index of the dispersant, λ_0 is the wavelength of the laser light used and θ represents the angle at which scattering is detected. From the diffusion coefficient the hydrodynamic radius of the particles can be determined as seen in eqn 2.4. This type of modelling can also be used to model polydisperse samples by substituting the single exponential term in eqn 2.6 with a sum of exponential decays.

The instrument used in our experiments is a Zetasizer Nano-ZS manufactured by Malvern instruments. This instrument consists of 6 main parts. A He-Ne laser as a light source (632 nm). A sample contained in a cell and sample cell holder, a backscatter detector at 173° relative to the incident light. In order not to over saturate the detector there is also an attenuator after the laser to control incident light intensity.

The next component is the correlator which feeds into the final component, the computer. The manufacturer's software was used for modelling the data. For more detailed information on the principles and practice of DLS see the following reference[7,8].

2.2.2 Zeta Potential Measurements

This measurement is performed by exploiting the electrokinetic phenomena of electrophoresis. Electrophoresis is the movement of charged colloidal particles or electrolytes in a liquid, under the influence of an electric field. The particle experiences several forces in these conditions. Firstly an electrostatic force is applied to the particle via the electric field. The particle also experiences a friction or drag force opposing the direction of the electrostatic force. There is also an electrophoretic retardation force which opposes the electrostatic force. This force depends on the size of the Debye length. When equilibrium is reached and all of these forces are equal, the particles move at a constant velocity. The velocity of a particle per unit field is referred to as the electrophoretic mobility. The drift velocity is dependant on the following parameters: the strength of the electric field applied, the dielectric constant of the medium, the viscosity of the medium and the zeta-potential. The formula used in our experiments as a model is Henry's formula:

$$\mu_e = \frac{2}{3}\frac{\varepsilon\zeta}{\eta} f(ka) \qquad \text{(eqn 2.8)}$$

Where μ_e is the electrophoretic mobility, ε is the dielectric constant of the medium, η is the dispersant viscosity and ζ is the zeta potential. $f(\kappa a)$ is a number that varies between 1 and 1.5 depending on the sample being measured. The parameter a is the particle radius and κ is the inverse of the Debye length expressed by eqn 2.9:

$$\kappa = \left\{ \frac{\sum_{i=1}^{N} e^2 z_i^2 n_i}{\varepsilon_{rs} \varepsilon_0 kT} \right\}^{\frac{1}{2}} \qquad \text{(eqn 2.9)}$$

where e is the elementary charge, z_i, n_i the charge number and number concentration of ion i (the solution contains *N* ionic species), ε_{rs} the relative permittivity of the electrolyte solution, ε_0 the electric permittivity of vacuum, *k* the Boltzmann constant and *T* the thermodynamic temperature. When the radius of the particle is much larger than the Debye length then $\kappa a >> 1$, and $f(\kappa a)$ is approximated to 1.5. When the radius is comparable or smaller than the Debye length then $f(\kappa a) = 1$. This is referred to as the Huckel approximation. It is important to note that Henry's model has its limitations. First, it assumes that the samples are non conducting meaning that for conducting particles, it can only be used for zeta potential measurements below 50mV. The reason for this is that Smoluchowski's theory assumes that the electric field is independent of the presence of an electric double layer whereas in fact, they are interacting all the time. If ζ is greater than 50mV the interaction between the double layer and the electric field cannot be neglected and a different model must be used to account for surface conductivity. Such equations are the ones derived by Dukhim for symmetrical z-z electrolytes and Semenikhin or the equations of O,Brien and White. In our experiments we have applied only the Huckel model[9].

In the cell the electrophoresis is induced by applying a voltage across the sample cell. The field is reversed about every 1 second to help minimise electrode polarisation, which is caused by the build up of anions or cations around the positive or negative electrodes respectively. The measurement itself is performed using laser Doppler velocimetry; this technique uses a beam splitter to create two beams, an incident and reference beam. The incident beam is allowed to pass through the centre of the cell. The scattering light caused by the particles is detected at 13 degrees. This light is recombined with the reference beam. This produces a fluctuating intensity signal

which is proportional to the particle velocity in the cell. This is then converted into a zeta potential using the equations above. For a review see the following reference [9].

References

(1) Skrabalak, S. E.; Suslick, K. S. *Journal of the American Chemical Society* **2006**, *128*, 12642.

(2) Skrabalak, S. E.; Suslick, K. S. *Journal of Physical Chemistry C* **2007**, *111*, 17807.

(3) Lang, R. J. *Journal of the Acoustical Society of America* **1962**, *34*, 6.

(4) Lozano, A.; Amaveda, H.; Barreras, F.; Jorda, X.; Lozano, M. *Journal of Fluids Engineering-Transactions of the Asme* **2003**, *125*, 941.

(5) Barreras, F.; Amaveda, H.; Lozano, A. *Experiments in Fluids* **2002**, *33*, 405.

(6) Berne, B.; Pecora, R. *Dover Publications, Mineola, New York*.

(7) Chu, B. *Laser Light Scattering: Basic Principles and Practice, 2007*.

(8) Johnson, S. A.; Gabriel, D. A. *Laser Light Scattering, 1994*.

(9) Delgado, A. V.; Gonzalez-Caballero, E.; Hunter, R. J.; Koopal, L. K.; Lyklema, J. *Pure Appl. Chem* **2005**, 1753.

Chapter 3

Synthesis of Carbon Microspheres via ultrasonic spray pyrolysis

Porous carbon materials are of interest for their potential use in electrochemical, catalytic, adsorbent, and transport properties through porous matrices. Here, we report on the synthesis of Carbon microspheres (CMs) using ultrasonic spray pyrolysis (USP). It is demonstrated herein that the CMs have tuneable size, structure and surface chemistry via various characterisation techniques.

3.1 Introduction

In this chapter, we report on the use of ultrasonic spray pyrolysis (USP) as a method for synthesis Carbon microspheres (CMs) as previously reported by Skrabalek et al [1]. We have characterized the structure, morphology and composition of these CMs using a combination of SEM, Raman, FTIR and BET analysis. Subsequently, the versatility of USP technique was demonstrated by achieving size control over CMs using two different parameters. Finally, in order to demonstrate the surface chemistry of the CMs, functionalisation experiments were performed using Diazonium grafting reactions. Our results show that USP can be used to create CMs of differing morphology and porous structure using different precursor solutions in the USP apparatus, in agreement with previous reports. It is also demonstrated that resulting microspheres are all carbon in nature with various carboxylate and carbonyl groups on the surface. We have also confirmed that precursor solution concentration and nebuliser frequency can both be used to achieve CM size modification utilising USP methods. FTIR and zeta potential measurements confirm that CM surfaces can be modified via the use of Diazonium salt chemistry. On the light of these studies we discuss potential applications of CM produced using USP techniques.

3.1.1 USP Methods for carbon microsphere synthesis

In 2006, Skrabalak et al. utilised USP to obtain meso and macro porous CMs [1]. They proposed a design criterion for the choice of organic precursor solutions to obtain carbon microspheres. They assume that volatile stable leaving groups will dissociate from heated droplets of organic precursor solution, and due to subsequent pyrolysis, the organic salt breaks down into a halide salt and pyrolytic carbon. Hence, proposing

the formula below as a means to determine the end products of the thermal decomposition process.

$$M_mX_mC_n(CO_2 \text{ or } SO_3)_aH_bX_c$$

where M is an alkali metal ion, X is a halide or hydroxyl. By defining N = b – c, they were able to give the likelihood of obtaining CMs. They observed that for N values of 0 and 2, spherical and networked CMs where obtained. Outside of this range the carbon materials obtained were ill defined, indicating that ideally b should equal c to ensure the remnants from decomposition contain just carbon. They also observed that by only changing the alkali metal ion in various organic precursor solutions they were able to achieve CMs with varying surface area, porosity and morphology. They suggested the differences in morphology are due to the relative order and kinetics of the following processes [1,2].

i) Melting of organic salt
ii) Exothermically decompose of the organic salt may release MX
iii) Endothermic decarboxylation of the organic salt
iv) Melting of the inorganic salt MX.

3.1.2 Modification of surface chemistry and charge

Control over the surface charge and surface chemistry of carbon particles can be achieved via surface functionalisation reactions. One of the most exploited methods is using diazonium salt chemistry to attach aromatic groups to carbon surfaces. This approach will be used to impart charge to the particles by functionalizing them with ionisable moieties such as -ArCOOH or -$ArSO_3H$. Aryldiazonium salts can be grafted electrochemically and the mechanism involves the transfer of a reductive electron to the diazonium [3]. The reaction involves the cleavage of dinitrogen leading to the formation of an aryl radical; this radical then binds to the surface of the carbon via

covalent bonding as demonstrated in figure 3.1. In literature this reaction has been shown to happen spontaneously for carbon black and carbon nanotubes without electrochemical induction [4].

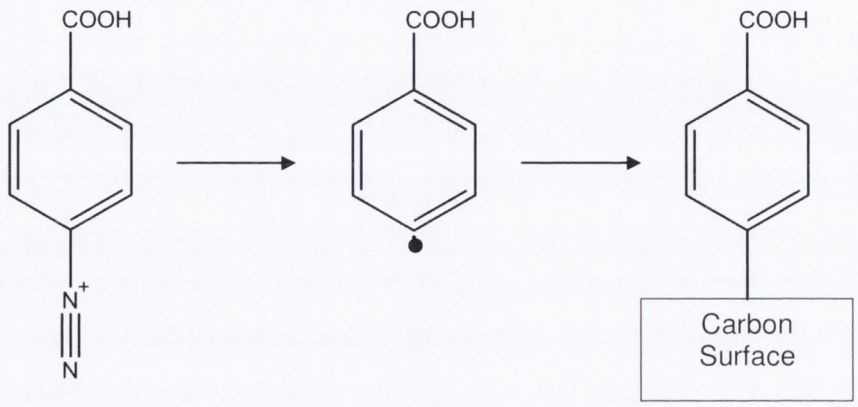

Figure 3.1: Schematic demonstrating an example of a diazonium grafting reactions.

The presence of acidic groups can be used to control the surface charge of the particles and therefore the transport and mobility of the carbon material in different chemical environments. The change in surface charge can be monitored via measurement of the particle zeta potential as described in detail in section 2.1.3.

3.2 Experimental

3.2.1 Materials

Reagent grade lithium hydroxide (96%; Sigma), sodium hydroxide (98%, Sigma), potassium hydroxide (98%, sigma), dichloroacetic acid (DCA, 99%, Sigma Aldrich), 4-amino benzoic acid (Compound 1), (99%, Sigma), sulfanilic acid (Compound 2), (99%; Sigma), n,n-diethyl-p-phenylenediamine (Compound 3) (97%; Sigma Aldrich), NaCl

(99% Sigma Aldrich), Hydrochloric acid (30%,), 4-carboxyphenyl diazonium, 4-diazo-*N*,*N*-diethylaniline fluoroborate, 4-sulfophenyl diazonium

3.2.2 Synthesis of Porous carbon microspheres

Porous carbon microparticles were prepared using the USP methodology described in Section 2.1.1. First the USP apparatus was set up as described in section 2.1.1 as demonstrated by the photo in Figure 3.2. A typical experiment involves making a 1.5 M precursor solution which is prepared volumetrically with deionised water. 250 mL of 3 M dichloroacetic acid and 250 ml of 3 M alkaline hydroxide were mixed in order to obtain the subsequent alkali dichloroacetate solution. The solution was made up to 500 mL as the reaction resulted in less than 500 ml volume.

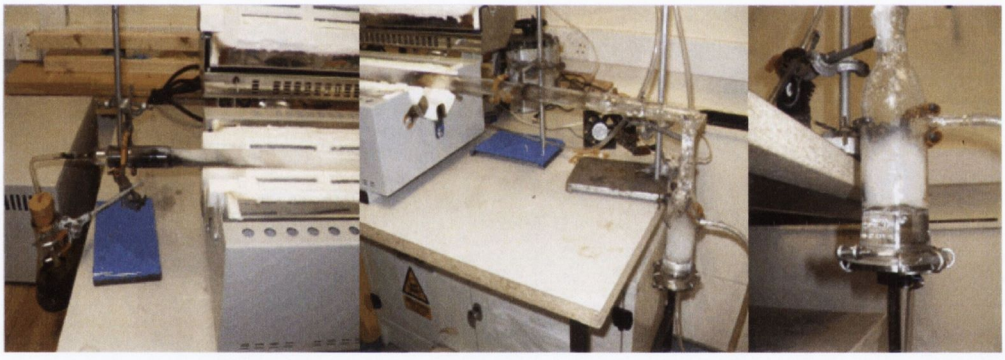

Figure 3.2: Photo of the USP setup used for the synthesis of CMs in our laboratory.

The solution was left to cool for 10 min. 100 ml of the alkali dichloracetate solution was placed in the atomisation vessel of the USP system via the solution addition arm. The reaction system was purged of oxygen by maintaining a constant flow of Argon at 2 standard litres per minute (SLPM). The furnace was preheated to 710 °C. The piezoelectric nebuliser (Piezo) was switched on thus generating a mist of the precursor solution. Precursor solution was added using a pipette via the solution addition arm in order to keep a constant liquid level. The process was allowed to continue until sufficient carbon particles were observed in the bubbler. Carbon particles were

purified via filtration through 0.45 μm membranes and washed with copious amounts of water to remove inorganic salts and with ethanol to remove any organic residues. The particles were then characterised using DLS, zeta potential measurements, FTIR, Raman and SEM imaging.

3.2.3 Functionalisation of carbon Microspheres

Synthesis of the Diazoniums salt mentioned in this report was performed by Deirdre Murphy in our Laboratory.

Synthesis of 4-carboxyyphenyl diazonium tetrafluoroborate: followed the method reported by D'Amours et al which involved using p-aminobenzoic acid as a precursor [5]. A light yellow powder was obtained. This was washed with ice cold ether and suction dried. A yield of 64% was obtained

Synthesis of 4-sulfobenzenediazonium tetrafluoroborate: followed the method reported by Hermans et al which involved using 4-aminobenzenesulphonic acid (sulfanilic acid) as a precursor [6]. A pale cream/white powder resulted which was vacuum filtered and washed with ether:methanol mix. A yield of 82.61% was obtained.

CMs were added to 25 ml of water to an end concentration of 0.04 g/l. This suspension was cooled to 4 °C followed by subsequent addition of diazonium salt to an end concentration of 0.5 M. The reaction vessel was left for 48 h in a 4 °C environment with occasional agitation. CMs were removed from the diazonium solution via filtration through 0.45 μM filter membranes. CMs were washed with copious amounts of cooled water, followed by washings of acetonitrile and ethanol. Samples were dried under a steady flow of Ar gas and subsequently stored in a vial containing Ar gas.

3.2.4. Characterisation techniques

Scanning Electron Microscopy (SEM) was performed at an accelerating voltage of 10 keV using a Zeiss Ultra microscope equipped with in lens, secondary and electron backscatter detectors. Particle size distributions were obtained via SEM from particle diameter determination of particles for LiDCA and NaDCA samples from images. Raman spectra were collected on a micro-Raman system (Renishaw 1000) equipped with a CCD camera and a Leica microscope. The 457 nm line of an Ar laser was used as the excitation source. A grating with 1800 lines/mm was used for all measurements, providing a spectral resolution of ~1 cm^{-1}. Spectra were collected in extended mode with 10 s exposure time, 10 accumulations, and a laser power of 0.25 mW to avoid laser burning of the carbon surfaces. z-Potential measurements were carried out on a Malvern Zetasizer Nano-ZS: HCl or NaOH was added to particle suspensions in order to vary the pH followed by an addition of NaCl in order to bring the total ionic strength to a value of 0.010 M. DLS measurements were carried out on a Malvern Zetasizer Nano-ZS: Deionised water filtered using 0.45 μm filter membranes was used in order to minimise contributions from larger particles in the solute, Also, particles were sonicated for 1 minute directly prior to measurement to ensure signal generated from any CM particle aggregates was at a minimum. FTIR measurements were performed on a Bruker Tensor 27 FTIR spectrometer at 2 cm^{-1} resolution equipped with a 13 mm pellet holder. Pellets for FTIR were prepared by compressing a mixture containing 0.1 g of dried KBr powder with 0.001 g of CM powder using a 13 mm die tool exerting a load of 6 ton for 1 min. The specific surface area of carbon spheres was determined via Brunauer–Emmett–Teller (BET) analysis (Quantachrome Nova Station) [7]. The sample was pre-treated at 100 °C under vacuum for 24 h prior to analysis using nitrogen as the adsorbing gas. The specific surface area was calculated using a multi-point BET plot over relative pressures in the range 0.08–0.3. Pore size was determined via the Barrett–Joyner–Halenda (BJH) [8] method using the desorption branch of

adsorption isotherms [9]; values reported represent the mode of the pore size distribution.

3.3 Results and Discussion

The results section will consist of two parts. Part (i) reporting results on the characterisation of CMs synthesized using USP. Part (ii) reporting results on size control and surface modification of the CMs. These sections will be followed by a discussion of the results, with suggestions for supplemental and follow-up experiments.

3.3.1 Characterisation of CMs

Carbon microspheres were produced from three different precursor solutions in our experiments; Lithium Dichloroacetate (LiDCA), Sodium Dichloroacetate (NaDCA) and Potassium Dichloroacetate (KDCA) precursor solution. CMs produced from the various precursor solutions will be subsequently referred to as the abbreviation for the precursor solution in order to differentiate between types. The microspheres were characterised using a combination of Raman, SEM and BET analysis in order to establish if pyrolysis occurred, particle morphology and specific surface area.

In order to gain information about the nature of the carbon materials in CMs synthesized via USP, Raman measurements were preformed on carbon powder. Figure 3.3 shows the Raman spectra of carbon microparticles obtained via USP for the three precursor solutions utilised. The Raman spectra are consistent with that observed for highly graphitic amorphous carbons and displays two scattering peaks with maxima at 1597 and 1350 cm^{-1} that we can assign to the G and D bands of amorphous carbons respectively [10]. The peak at 1597 cm^{-1} is named G after the E_{2g} mode of graphite and

is observed in other carbon materials that are rich in sp^2 bonded atoms; therefore its intensity increases with an increase of sp^2 carbons. The peak at ~1350 cm^{-1} is assigned to an A_{1g} mode of aromatic rings observed in graphite when disorder and symmetry breaking are introduced and is a characteristic signature of disordered carbon materials [11].

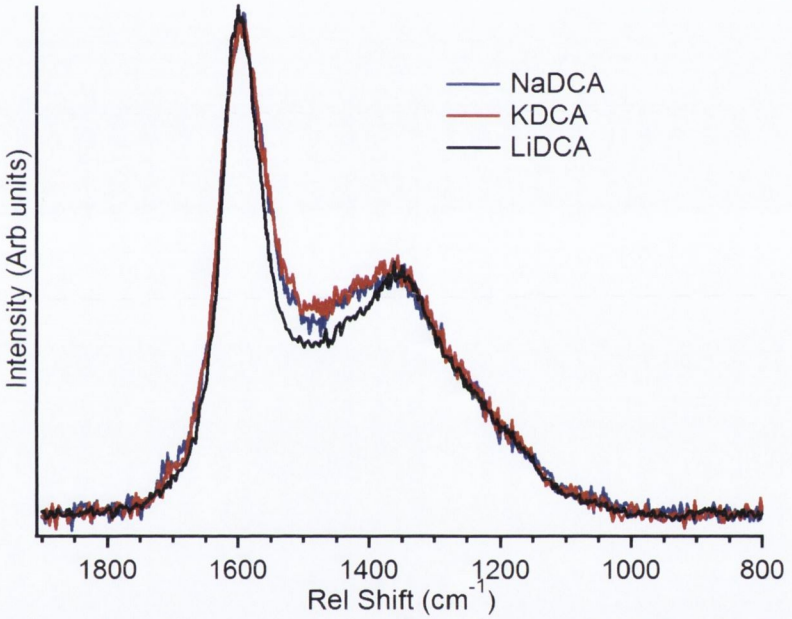

Figure 3.3: Raman spectrum of microspheres (exc. 457 nm); the profile displays the D and G bands that are characteristic of amorphous carbons.

The spectrum in figure 3.3 therefore confirms that the precursor is pyrolized to form a highly graphitic material. However, it does not exclude the presence of sp^3 or hydrogenated regions in the particles which would be "silent" or have much lower Raman cross-section [12].

The morphology of the various CMs was investigated via SEM imaging. Figure 3.4a shows an SEM image of a typical LiDCA CM and figure 3.4b shows the size distribution in percentage by number obtained for 1.5 M LiDCA particles as measured from SEM

images. The image shows spherical microspheres are obtained for this solution with microspheres having an average size of 920 nm with a standard deviation of 35%.

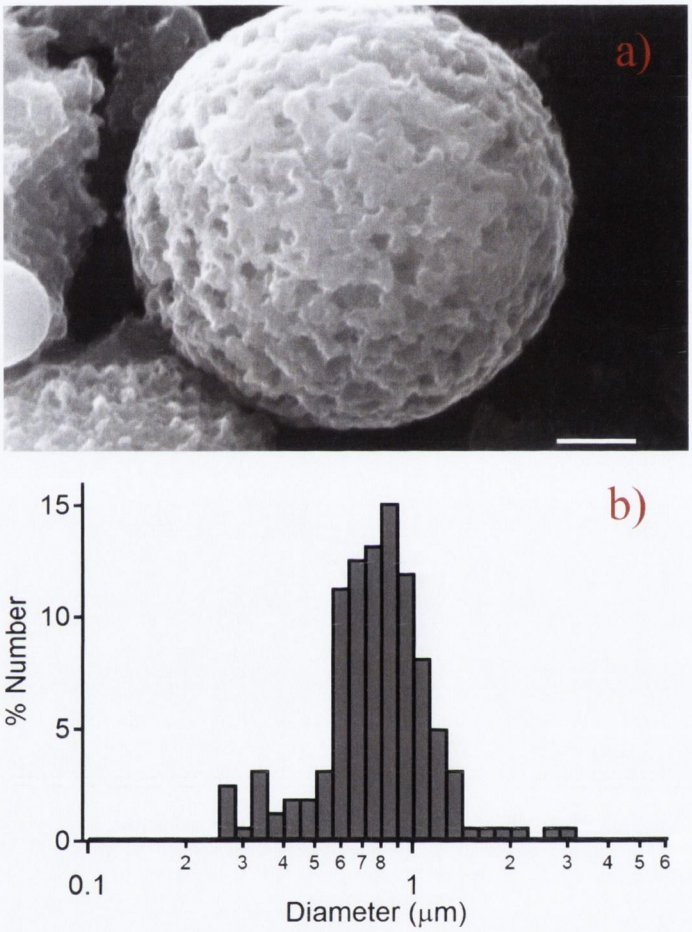

Figure 3.4: a) Shows SEM image of a CM synthesized using LiDCA as a precursor solution; Scale bar = 200 nm, b) Size distribution obtained from SEM images from 100+ particles for 1.5 M LiDCA precursor solution.

The image also demonstrates that the CMs obtained have a mesoporous structure via the small pores visible on the CM surface, each of which has a different porous structure. Figures 3.5a shows an SEM image of a typical NADCA CM and Figure 3.5b shows the size distribution obtained for 1.5 M NaDCA particles as measured from SEM images. The image shows spherical microspheres are obtained for this solution with microspheres having an average size of 1760 nm with a standard deviation of 30%.

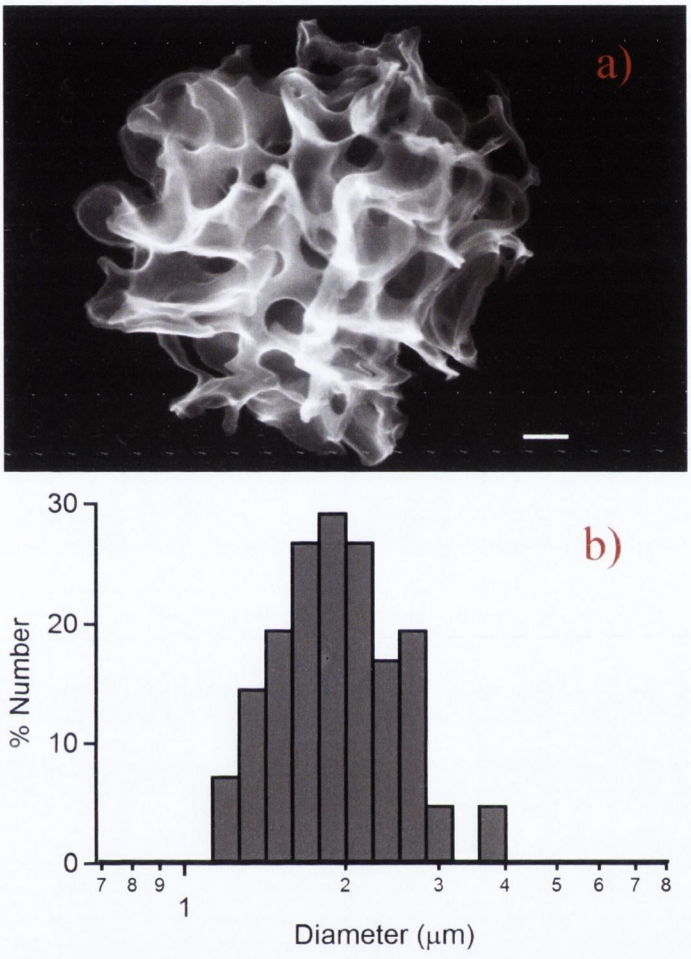

Figure 3.5: a) Shows SEM image of a CM synthesized using NaDCA as a precursor solution; Scale bar = 200 nm, b) Size distribution obtained from SEM images from 100+ particles for 1.5 M NaDCA precursor solution.

Not only does the size of the NaDCA differ to the LiDCA CMs, the morphology of the NaDCA CM is vastly different to that of LiDCA CM as observed via SEM. The image demonstrates that the NaDCA CMs obtained have a more open structure via the large 200 nm openings visible on the CM surface. Figures 3.6a shows an SEM image of a typical KDCA CM and Figure 3.6b shows the size distribution obtained for 1.5 M KDCA particles as measured from SEM images. The image shows spherical microspheres are obtained for this solution with microspheres having an average size of 1680 nm with a standard deviation of 32%.

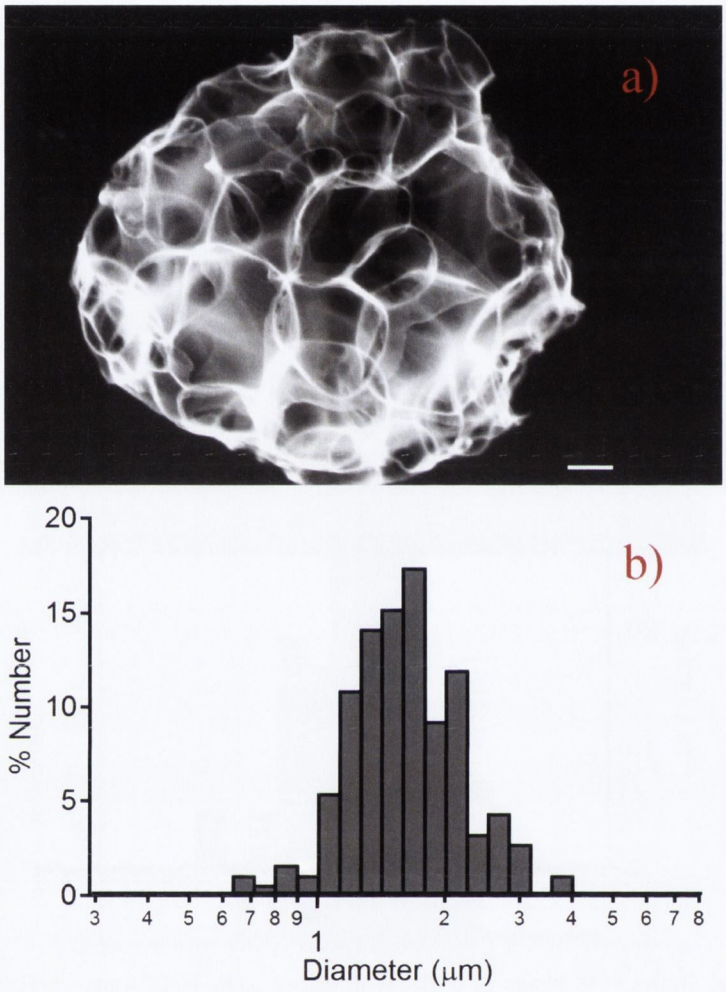

Figure 3.6: a) Shows SEM image of a CM synthesized using KDCA as a precursor solution; Scale bar = 200 nm, b) Size distribution obtained from SEM images from 100+ particles for 1.5 M KDCA precursor solution.

The image also demonstrates that the CMs obtained have similar structure to the CMs synthesised utilising NaDA. However, whilst similar the two CMs have slightly differing morphologies as demonstrated by comparing the SEM images. Also of note, the standard deviations obtained for the size distributions of the various solutions are very similar, regardless of significant size and morphology differences. This indicates that the primary source of particle size deviation is the USP system itself, where droplet formation by the piezo and subsequent drop coalescing on the carrier gas are likely to

be responsible for the deviations from uniform particle size. Also of note, is that a log normal distribution is obtained for all three solutions, as observed via the SEM size distributions, further supporting the USP system as the source of size variation.

BET adsorption experiments where performed to determine the surface areas of the various CMs. Table 3.1 shows the results of BET surface area experiments.

Precursor solution	Surface area (m^2/g)	Pore Size diameter (Å)
LiDCA	1040	17.1
NaDCA	544	163.4
KDCA	618	15.3

Table 3.1: Surface area and pore size results from BET analysis

The BET data fits well with observations in SEM. NaDCA and KDCA have similar but not identical surface areas, supporting qualitative observations about there morphologies based on SEM images. LiDCA appears to be vastly different to the other two carbon materials, with a very high specific surface area of 1040 m^2/g. This is most likely due to the mesoporous structures giving a larger surface area than the large pores observed for the NaDCA and KDCA, which can be seen on SEM images. Table 3.1 also shows pore sizes determined via the Barrett–Joyner–Halenda (BJH) [8] method using the desorption branch of adsorption isotherms. The values reported represent the mode of the pore size distribution. KDCA is shown to have a similar pore size diameter to LiDCA, with values of 15.3 Å and 17.1 Å obtained respectively. NaDCA is reported as having a significantly larger pore size of 163.4 Å. By taking the Raman, SEM and BET data together, it is possible to conclude that by using USP we can synthesis spherical carbon particles in the microsphere range, with different morphologies, porosities and surface areas.

3.3.2 Size control of carbon microspheres

Size distributions were also obtained using DLS for the 1.5 M LiDCA and NaDCA particles. Figure 3.7a and b show the typical size distributions obtained for the LiDCA and NaDCA CMs respectively. At least five distributions like these were taken and the number percentage maximum was averaged.

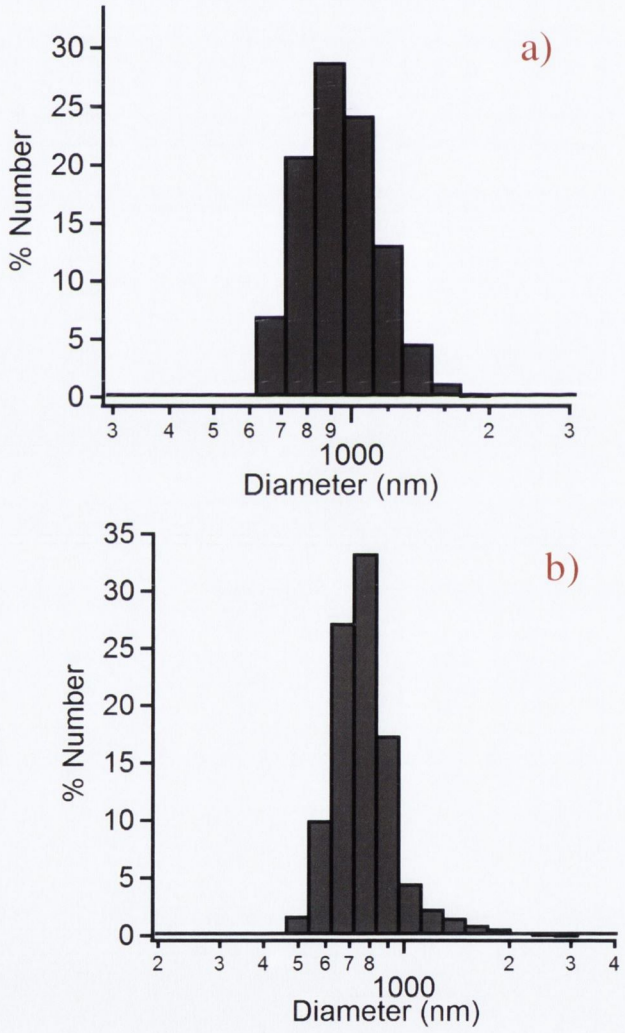

Figure 3.7: Typical DLS size distribution of carbon particles produced by USP of 1.5 M solutions of a) LiDCA and b) NaDCA.

Number maximum was used for all subsequent data as opposed to mean average size. An average number intensity maximum was calculated at 915 nm for LiDCA in good agreement with the number maxima of 850 nm obtained from analysis of SEM images. For figure 3.7b a particle number maxima is obtained at 955 nm which is in poor agreement with the number peak located at 1850 nm obtained via SEM images for NaDCA particles. These comparisons indicate that LiDCA particles are suitable for DLS measurements and give reasonable size data. However, NaDCA particles do not produce a reasonable size when using DLS. This is likely due to the presence of large openings in NaDCA microspheres which would likely require more complex modelling of effective particle refractive index and, possibly, diffusion coefficients. Therefore, we concluded that DLS was not a suitable method for size determination in the case of these large and more morphologically complex carbon particles. Therefore subsequent size control experiments were performed using LiDCA particle for simplicity. Figure 3.8 shows typical DLS results obtained for LiDCA particles synthesised at 0.125, 1.0 and 1.5 M concentration respectively.

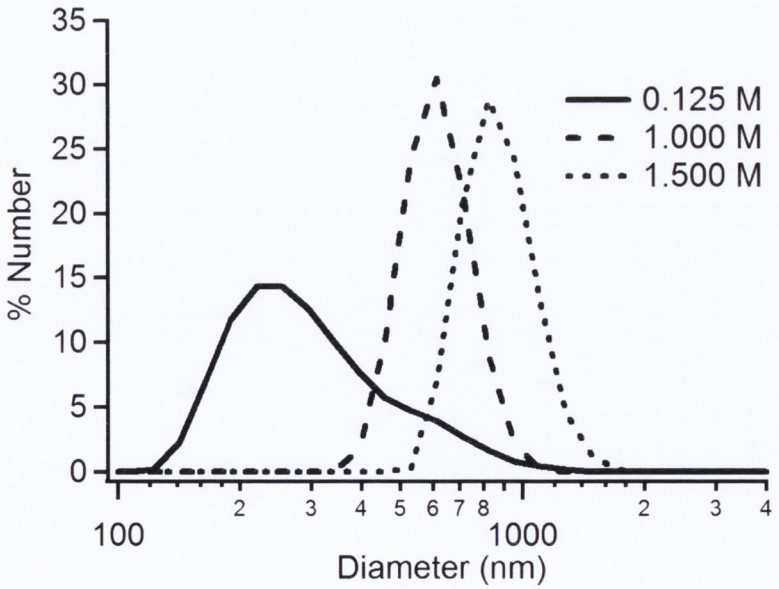

Figure 3.8: DLS size distributions for 0.125, 1.000 and 1.500 M concentration LiDCA precursor solution.

By averaging over 5 such distributions Number maxima are obtained at 900, 733 and 255 nm for the 1.5, 1.0 and 0.125 M concentrations respectively. These results indicate that it is possible to leverage precursor concentration as a method for controlling CM particle size, as would be expected for a USP system.

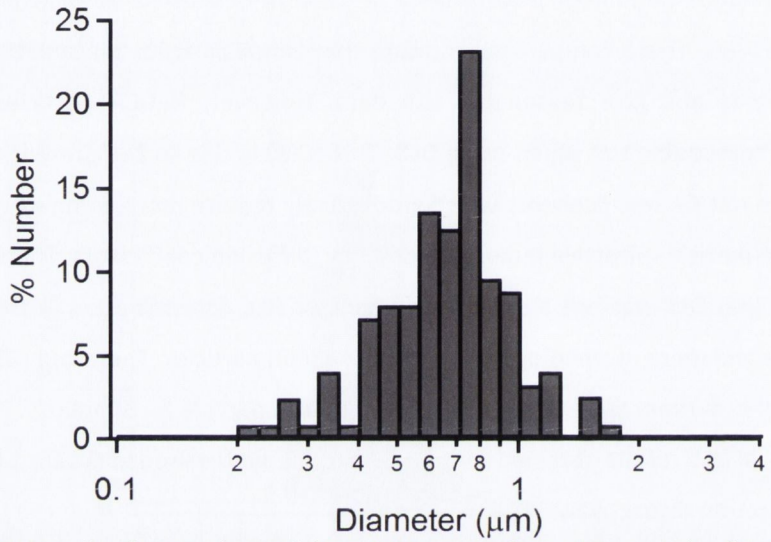

Figure 3.9: Size distribution obtained from SEM images from 100+ particles for 1.0 M LiDCA precursor solution.

Figure 3.9 shows a size distribution obtained via SEM images for 1.0 M LiDCA in order to confirm size control and further support DLS data. The graph has number maximum at approximately 750 nm in good agreement with the obtained DLS value of 733 nm, further supporting the suitability of LiDCA particles for characterisation via DLS. More importantly, it confirms that control of particle size can be achieved by leveraging precursor concentration due to distributions determined via SEM for 1.5 M LiDCA gave a number maximum of 850 nm, supporting all the DLS data obtained in figure 3.5.

For the next series of size data shown, the piezo used in order to generate the mist in the USP system was changed from 1.67 MHz to 2.54 MHz. Figure 3.10 shows typical distributions obtained via DLS for 0.125 M, 0.500 M and 1.00 M solutions of LiDCA respectively using a 2.54 MHz piezo. The graph demonstrates again that size control is achievable by varying the concentration of the precursor solution. However, by taking

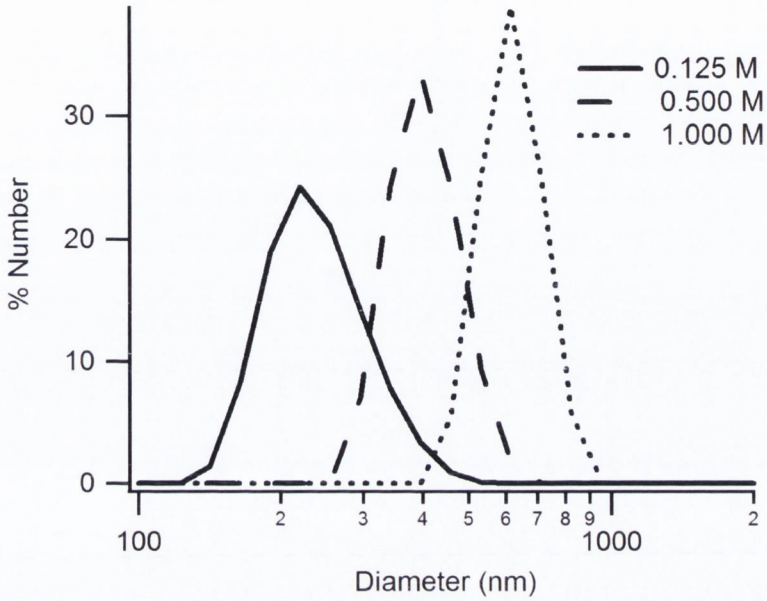

Figure 3.10: DLS size distributions obtained using 2.54 MHz Piezo electric disk for 0.125, 0.500 and 1.000 M LiDCA.

an average of five such distributions it is possible to demonstrate size change due to piezo frequency. The number maximum occurs at 220 nm and 255nm for the 2.54 MHz and 1.67 MHz respectively at 0.125 M precursor concentration. The number maxima for 1 M concentration of precursor was calculated at 630 nm and 733 nm for the 2.54 MHz and 1.67 MHz piezo respectively. This result indicates that it is possible to change CM size via changes to the piezo frequency in the USP system. These results are analysed in more detail in the discussion.

3.3.3 Surface charge and chemistry

Figure 3.11a shows a representative infrared transmission spectrum of microspheres used in our experiments. The infrared spectrum shows broad absorptions in the region 1700–1000 cm^{-1} characteristic of disordered graphitic carbons such as soots and

carbon blacks. A prominent broad and intense contribution around 1600 cm^{-1} can be assigned to C–C stretching modes of polyaromatic systems and suggests that microparticles consist mainly of sp^2 carbon [13,14]. This conclusion is supported by the presence of an aromatic C–H stretching peak at 3055 cm^{-1} [15].

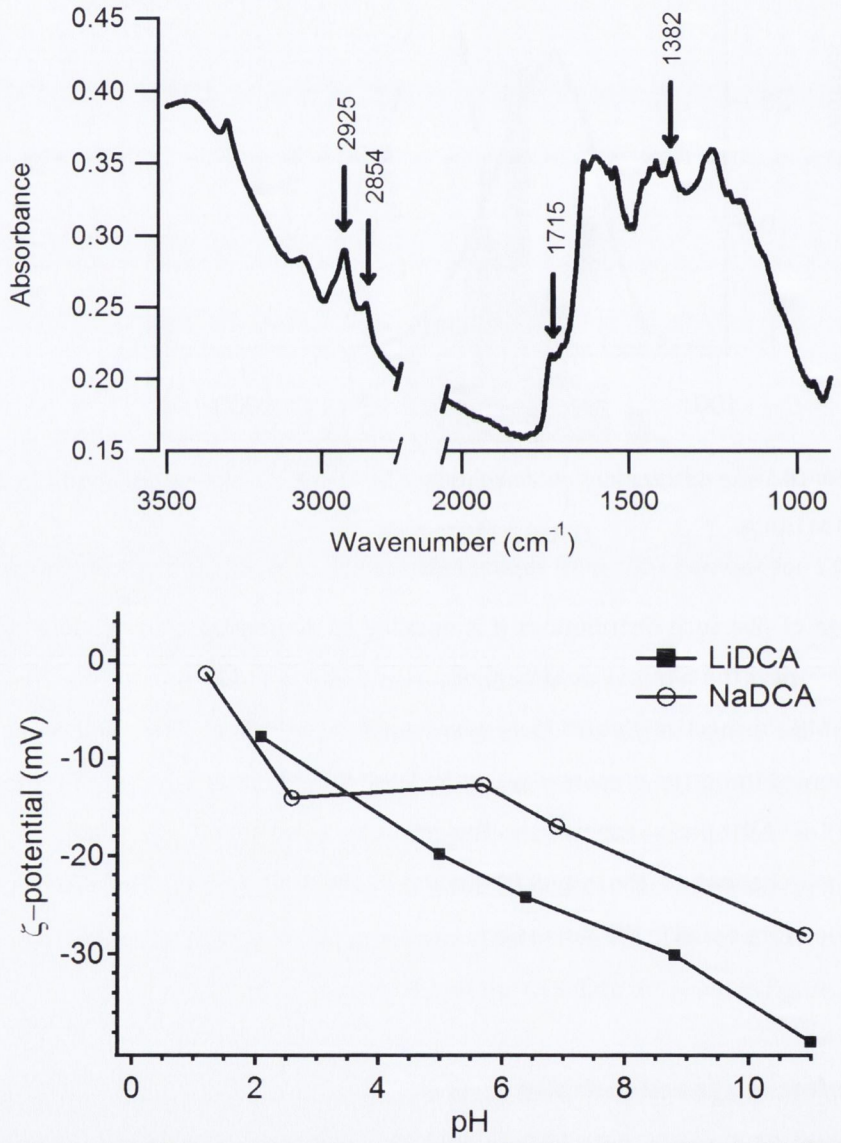

Figure 3.11: (a) Infrared transmission spectrum of carbon microspheres; (b) ζ-potential of carbon microspheres in aqueous suspensions as a function of pH.

The presence of aliphatic C–H stretching modes at 2854 and 2925 cm^{-1} and of methyl bending modes at 1382 cm^{-1} indicate that microspheres also contain residual sp^3 carbon after thermal decomposition of the organic precursor [15]. Finally, the infrared spectrum in Figure 3.11a shows a shoulder at 1715 cm^{-1} that can be assigned to the C=O stretching mode of carboxylic acid groups (–COOH) [13-15]. FTIR results suggest that acid groups, which can impart a negative surface charge to the microspheres, are likely present on the carbon surface after synthesis. The presence of carboxylic groups was further supported by ζ-potential measurements of pristine particles in aqueous suspensions, which yielded negative ζ-potential values over the 2–10 pH range. Figure 3.11b shows the ζ-potential of microspheres as a function of pH from which an estimated isoelectric point of pH_{iep} = 0.2 and 1.0 for LiDCA and NaDCA particles, respectively, was determined. Values of $pH_{iep} < 2$ are frequently observed for black carbons after mild activation treatment [16] and confirm that negatively charged groups are present on the particle surface under the pyrolysis conditions used for the synthesis.

Attempts to modify surface chemistry of two differing CM were made via grafting reactions of three diazonium salts. Figure 3.12a-c shows the FTIR spectrum obtained for the CMs modified with *p*-carboxybenzene diazonium, p-sulphonate diazonium and n,n-diethylaniline diazonium respectively. LiDCA CMs were used for the *p*-carboxybenzene diazonium, p-sulphonate diazonium and NaDCA CMs were used for the n,n-diethylaniline diazonium. For all graphs pristine carbon is the red line and functionalised is the blue line. In Figure 3.12a a peak is observed at 1690 - 1685 cm^{-1} in the functionalised carbon which is not observed in the pristine. This peak can be assigned to the aryl-COOH stretching [15], supporting the presence of COOH at the CM surface due to grafting of *p*-carboxybenzene diazonium. In figure 3.12b peaks are observed at 1035, 1126 and 1188 cm^{-1} when compared to the pristine carbon. The peak at 1035 cm^{-1} can be assigned to the symmetric stretching of S=O [17]. The peaks at 1126 and 1188 cm^{-1} can be assigned to stretching vibrations of the S=O [17,18].

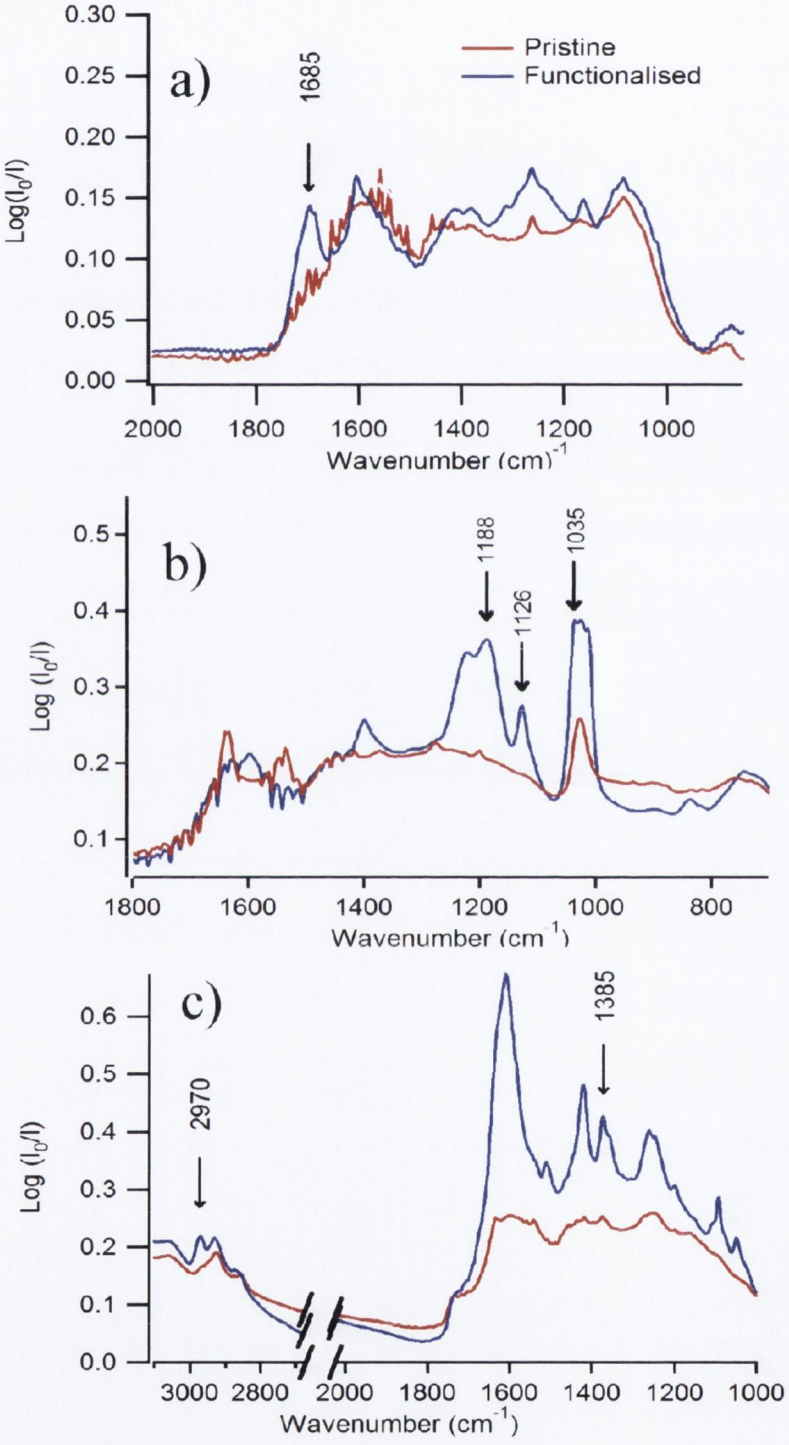

Figure 3.12: FTIR spectrums of pristine carbon (Red) vs CM functionalised (Blue) with a) *p*-carboxybenzene diazonium b) p-sulphonate diazonium and c) n,n-diethylaniline diazonium.

This indicates the presence of the SO_3 group in p-sulphonate diazonium which could suggest grafting at the CM surface. In figure 3.12c a peak is observed at 2970 cm^{-1} in the functionalised which can be assigned to the aliphatic -CH_2 or –CH_3 stretching [15]. The peak at 1385 cm^{-1} due to methyl bending modes increased significantly in the functionalised, further supporting an increase of -CH_3 groups at the CM surface. This would be expected if grafting occurred at the carbon surface of a molecule containing diethyl groups. Importantly, in all the FTIR spectrums, there was no peak observed near 2280 cm^{-1} which is observed for N≡N stretching mode. Coupling this with the observed peaks and data suggests that covalent grafting has occurred at the carbon surface for all the diazonium chemistries.

Zeta potential measurements of functionalised CMs are shown in Figure 3.13a-c. Figure 3.13a show that the ζ-potential shifts to more negative values for CM functionalised with the *p*-carboxybenzene diazonium chemistry. This result suggests that there are more negatively charged surface terminus groups on the CM surface. This is supported by the FTIR data which indicated that there were more COOH groups present on the surface when compared to pristine carbon. Figure 3.13b show the zeta results for functionalisations with the p-sulphonate diazonium chemistry. The figure shows that the potential is more negative for the functionalised CMs compared to pristine, across the pH range measured. Again, this indicates the presence of more negatively charged surface terminus groups when comparing to the pristine particles. This supports the FTIR data which indicated grafting at the CM surface. Figure 3.13c shows the zeta results for the n,n-diethylaniline diazonium chemistry. The figure shows that the potential is more positive for the functionalised CMs compared to the pristine, across the pH range measured, indicating more positively charge surface terminus groups. This would be expected for more methyl groups at the surface, indicating functionalisation has occurred.

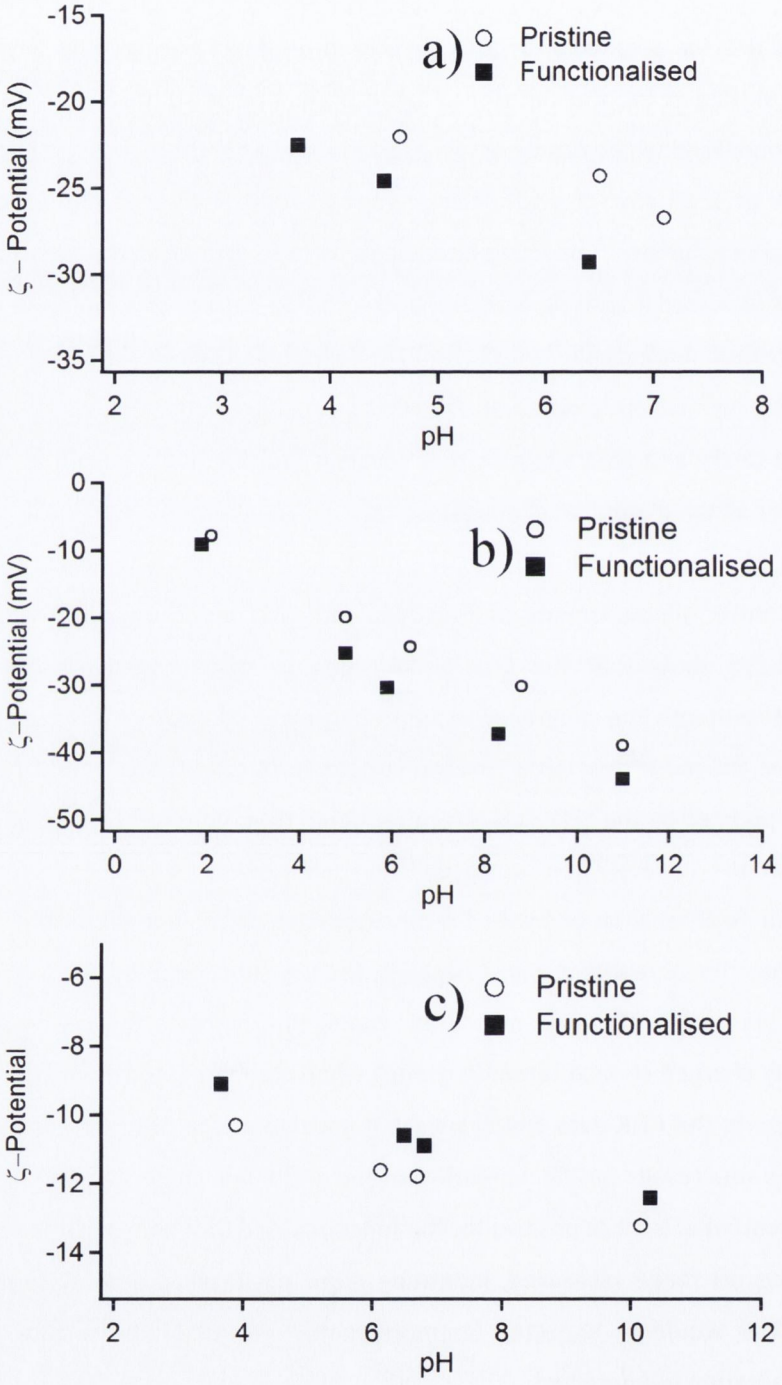

Figure 3.13: z-potential measurements of pristine CMs shown in comparison to z-potential of CMs functionalised with a) *p*-carboxybenzene diazonium b) p-sulphonate diazonium and c) n,n-diethylaniline diazonium.

In summary, Coupling the FTIR and ζ-potential data together suggests that it is possible to modify both surface charge and functionality of CMs surface via spontaneous diazonium grafting reactions

3.3.4 Discussion and summary

CMs were successfully synthesised via USP techniques using three different types of precursor solutions. Raman measurements confirm that the microspheres produced consist of carbon material. SEM and BET characterisation demonstrated that the CMs produced from the different precursors had vastly differing morphologies and porous structures. Combinations of SEM size distributions and DLS showed DLS is a suitable technique for measuring particle size of LiDCA particles but not NaDCA particles. Further DLS measurements on various concentrations of LiDCA produced particles demonstrated that it is possible to control CM size via use of precursor concentration and piezo frequency. FTIR, Raman and Zeta potential show that the CM surface contains carboxyl terminating groups as well as graphitic carbon. FTIR and Zeta potential measurements indicate that it is possible to graft various functional groups onto the carbon surface via diazonium salt chemistry. In this section, we discuss these results, implications and suggest some further experiments that may need to be performed to confirm assertions.

3.3.4.1 Carbon Microsphere characterisation

Raman spectra demonstrated peaks at 1350 and 1597 cm^{-1} characteristic of D and G peaks in carbon materials. The I(D)/I(G) height ratio is a useful parameter for determining the degree of order in amorphous carbons [10] By using a raman excitation of 514 nm, I(D)/I(G) for our particles was found to have a value of 0.61 ±

0.09. Based on the model developed by Robertson and co-workers[10] for the interpretation of Raman spectra of carbons, a G peak position of 1597 cm^{-1} and I(D)/I(G) = 0.61 suggest that the sp^2 content in these carbon microspheres is >80%, indicating that CM consist of highly graphitic material.

SEM images demonstrated spherical particles in the micrometer size range for all precursor solutions. CMs were observed to have differing morphologies dependent on the alkali ion in the precursor solution, in agreement with results obtained by others. LiDCA particles were observed to have a mesoporous structure which was drastically different from the spheres obtained using the NaDCA and KDCA precursors. These CMs had very similar but not identical macro-porous structures. Size distributions obtained via SEM images showed that the LiDCA particles have an average diameter of 920 nm with both NaDCA and KDCA having larger average particles sizes of 1684 and 1760 nm respectively. As all precursor solutions had a concentration of 1.5 M, it can be said each CM should consist of similar numbers of carbon atoms assuming complete pyrolysis occurs. LiCl, NaCl and KCl salts and taking the molar mass of each salt it is possible to estimate a volume difference between the inorganic salts after pyrolysis has occurred in the USP apparatus. NaCl and KCl occupy 83 % and 32% more volume, respectively, than LiCl for equal molar quantities. Considering the average particle size mentioned above, NaDCA and KDCA CMs occupy 600 % and 520 % more volume than the LiDCA particles. This would indicate that the difference in density of the salts templating the pore structures in the microspheres is not a significant factor in determining particles size differences observed between LiDCA and the other CMs. When comparing the Volume increase of NaCl compared to KCl and the volume change of NaDCA compared to KDCA we obtain figures of 39% and -12% respectively. These results are closer together and hence, it is possible that salt volume could be a parameter influencing particle size. It is possible to couple this volume analysis and similar morphologies observed via SEM to conclude that NaDCA and KDCA follow very similar but not identical pyrolysis kinetic processes in the furnace. It is equally possible by the same logic to conclude that LiDCA formation in the tube furnace must follow

much different orders and rates of pyrolysis compared to the other CMs. This is in agreement with results and hypothesis made by Skrabalak which states that carbon network formation for LiDCA occurs after the precursor melts whereas carbon network formation for NaDCA and KDCA particles occurs as a solid state reaction in the furnace [1]. This could offer a possible explanation to these observed size differences.

Multi point BET analysis gives further support for the assertions made above. 1040, 545 and 614 $m^2 g^{-1}$ are the surface areas obtained for LiDCA, NaDCA and KDCA carbons respectively. As the porous structure is formed by the pyrolysis of the precursor solution which occurs together with phase segregation of inorganic salt, differing orders and rates of decomposition could result in different porous structures. Again, NaDCA and KDCA have similar properties with surface area values which are close but not identical. However, LiDCA has a much larger surface area than either of the other conditions, consistent with the SEM images and previous statements about particle morphology. The larger surface area is likely due to significant numbers of mesoporous structures when compared to the NaDCA and KDCA. However, pore size analysis does not completely support this with KDCA and LiDCA having similar pores sizes of 17.1 and 15.3 Å respectively using the BJH method. It is important to consider that this method only gives the mode of the pore sizes. This could offer a possible explanation as to the similar sizes obtained. Pore size distribution measurements could be performed in order to weight accurately contributions from differing size pores. This would confirm the above about pore size being responsible for the surface area difference observed in the three carbon materials. However, most important for further applications of the CMs, all observed surface areas are quite large which makes potential use and further study of CMs as transport vehicles worthwhile. Assuming that all the carbon is graphitic in nature, all carbon atoms are surface atoms and all surfaces are planer, the maximum permitted surface area is 2400 m^2/g. However, specific surface areas > 1000 $m^2 g^{-1}$ are observed in the case of activated carbons,[19] and carbon nanocages, so the results obtained above are comparable to other forms of carbon. High specific surface area and small pore sizes, can in principle, allow the capture and delivery of small

molecules and nanoparticle for a variety of applications, from therapeutics, contrast agents and various environmental applications.

3.3.4.2 Size control of carbon microspheres

Size control was determined by measuring size distributions of various LiDCA produced CMs using DLS. Firstly, it was determined that DLS was a viable method for giving accurate size information for CMs diameters, by comparing size obtained via DLS to sizes obtained via SEM images. It was discovered that DLS is accurate for LiDCA CMs but not NaDCA CMs. This can be explained by considering the model used and assumptions made in our DLS experiments. DLS uses the Brownian motion of particles in a solution in order to estimate size; this estimation is done via the Stokes Einstein equation:[20]

$$d_h = \frac{kT}{3\pi\eta D} \qquad (2)$$

where d_h is the hydrodynamic radius, k is Boltzmann's constant, η is the solvent viscosity, T is temperature and D is the translational diffusion coefficient. A severe limitation of eqn 2 is that it assumes that particles are spherically shaped, so that the hydrodynamic radius is the radius of a sphere with the same translational diffusion coefficient as measured in the sample. Surface structures affect the diffusion coefficient by varying degrees depending on their orientation and properties. By looking at the SEM images obtained for the various CMs, it can be observed that microspheres produced by LiDCA are a much better approximation of a sphere than particles produced from NaDCA. In fact, NaDCA CMs have significant size surface structures relative to particle diameter which would shift these CMs drastically away from the model of a perfect sphere diffusing through a medium. This is the one possible explanation for the agreement between LiDCA CMs and not NaDCA CMs for DLS measurements and observed particle sizes via SEM. As our particles have sizes bigger than the wavelength of scattered light used, the effective refractive index of

spheres can have an effect on the intensity of scattered light and scattering cross section of particles [21,22]. However, in our measurements we modelled the refractive index over a range of 1.5-2.5 [23,24], the range for various carbon materials in literature. Whilst this did change the number maximum of the particles for NaDCA, a number maximum of 925 nm was the biggest achievable. This is still not comparible to the figures obtained via SEM images, indicating that DLS is still unsuitable for obtaining an accurate number size maximum for NaDCA CMs.

Using DLS, size distributions for different starting concentrations of LiDCA were obtained. It was observed that particle diameter was reduced with reduce concentration for LiDCA, in agreement with the theories and principles of USP generated using a piezo disk of fixed frequency. If the frequency is fixed, the diameter of the droplet generated should remain the same according to eqn 3 [25].

$$D = 0.34\left(\frac{8\pi T}{\rho F^2}\right)^{\frac{1}{3}} \quad (3)$$

Where D is the droplet diameter, T is the liquid surface tension, ρ is density of the liquid and F is the Frequency. Therefore, within the furnace each individual droplet acts as a separate reaction vessel containing limited amounts of dissolved precursor. Hence, upon decomposition, the resulting particle can only be of a limited size. Using mass balance, a given particles diameter is given by the following equation [25-27].

$$d_p = \left(\frac{M}{\rho}\frac{D^3}{1000}C_S\right)^{\frac{1}{3}} \quad (4)$$

Where M is the molecular mass, ρ is the expected density of the solid, D is the diameter of the droplet given by eqn 3 and C_s is the starting concentration of the precursor solution. Eqns 3 and 4 indicate that control over microsphere size can be achieved in two ways: by varying precursor concentration or by varying the frequency of the piezo disk in the nebuliser vessel in the USP system.

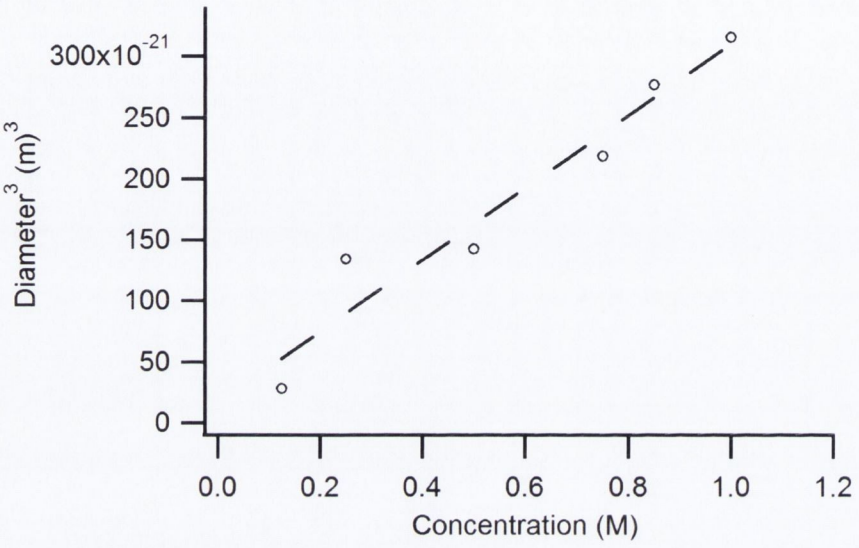

Figure 3.14: Plot of the particle diameter cubed, determined via DLS vs concentration of LiDCA solution.

Figure 3.14 shows a plot of d^3 vs C where d is the particle diameter and C is the precursor concentration, for solutions of LiDCA using the 2.54 MHz piezo. The diameter values are taken from the peak of size distributions by intensity as determined by DLS. From the plot a linear relationship is observed, indicating that for the precursor solutions used in our experiments, d_p and C hold the relation described in eqn 4 for the concentration ranges tested. To phrase it in more simple terms, the linear relationship means that CM volume is proportional to the concentration used. These results confirm that varying concentration is a facile method for controlling particle size in CM synthesis.

Particle size measurements also indicated that it was possible to control particle size by changing the piezo frequency. Table 3.2 summarises DLS measurements using the 1.67 and 2.54 MHz piezos for two different precursor concentrations. By using eqn 3 above we can determine that by changing the frequency from 1.67 MHz to 2.64 MHz there should be a 33% increase in particle diameter when going from the 2.64 MHz to

the 1.67 MHz piezo. However, analysis of our results suggest that a value of half that was obtained. A possible explanation for this could be due to an increase in droplet formation using the 2.54 MHz piezo. It was observed that significantly more mist was

Concentration	2.54 MHz	1.67 MHz	% increase
1.000 M	630	733	16.34
0.125 M	220	255	15.90

Table 3.2: Comparison of 2.54 and 1.67 MHZ using 1.000 and 0.125 M LiDCA

generated when using the higher frequency piezo. Increased number of droplets would correspond to an increased number of drops coalescing together. This in theory could cause the average particle size to increase. Performing an SEM size distribution and analysing the standard deviation of the distribution could potentially confirm this. As demonstrated for the 1.67 MHz piezo, the percentage deviation from the mean particle size is the same across all the precursor solutions, indicating that it is a property of the USP system itself. So if more coalasing is occurring with the 2.54 MHz piezo, it should be observable via a larger standard deviation in particle size distributions.

Figure 3.15a and b show SEM images obtained for the 0.125 M and 0.85 M LiDCA CM using the 2.54 MHz piezo. Figure 3.15b demonstrates that spherical CMs are formed using the 2.54 MHz piezo, which have the same morphology as those produced using the 1.67 MHz frequency. This was an important control to perform in order to verify that these particles would be suitable to DLS as those synthesized using the 1.67 MHz piezo, and validates all size DLS data given for the 2.54 MHz piezo. The image also supports DLS data which suggests a size reduction due to piezo frequency. Figure 3.15a show particles which are in the 100-350 nm range and figure b shows particles which are in the 400 – 700 nm range. However, to this date no size distributions have been performed using SEM images for particles produced using the 2.54 MHz piezo; this is now being carried out in the laboratory of a collaborator.

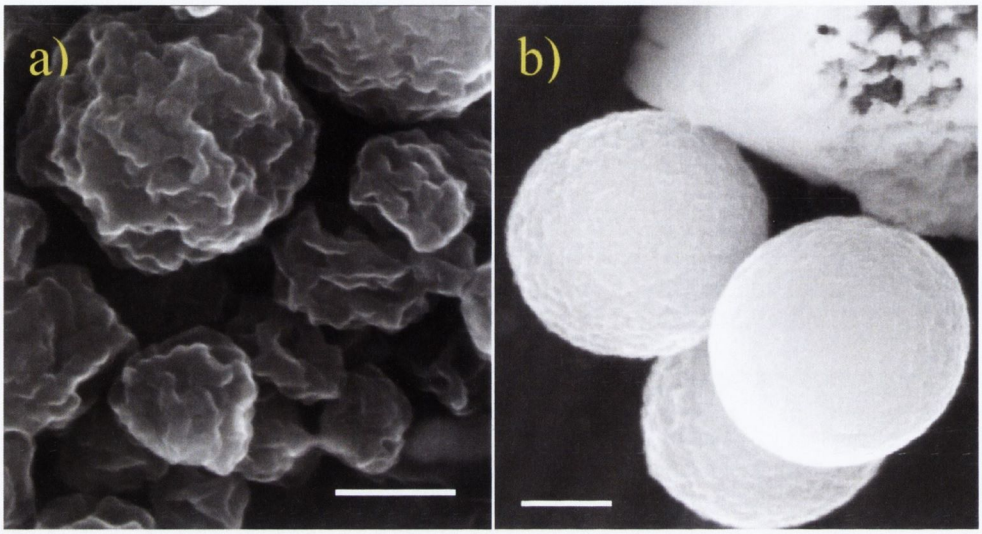

Figure 3.15: SEM images of CMs synthesised from the 2.54 MHz piezo using a) 0.125 M and b) 0.85 M LiDCA; Scale bar = 200 nm.

Interestingly, in figure 3.15a the 0.125 M particles appear to be less spherical than CM produced using the same precursor but at higher concentrations. This is likely due to the pore size becoming increasingly significant relative to total particle size, making the particles appear less spherical in this size range. This could indicate that the 0.125 M solution is quite near to a size limit for obtaining spherical particles using this protocol. Experiments utilising lower concentrations followed by SEM imaging would easily confirm what the size limit is for CMs produced using this protocol.

In order to confirm that size control was possible for CMs which had less spherical behaviour, similar experiments to those performed above on the LiDCA were performed on NaDCA CMs. Figure 3.16 shows size distribution data for 1 M NaDCA determined from SEM images. This gave a mean particle size of 1620 nm which is a decrease from the 1760 nm mean size determined earlier for 1.5 M NaDCA, indicating that size control is also possible for the NaDCA precursor solution.

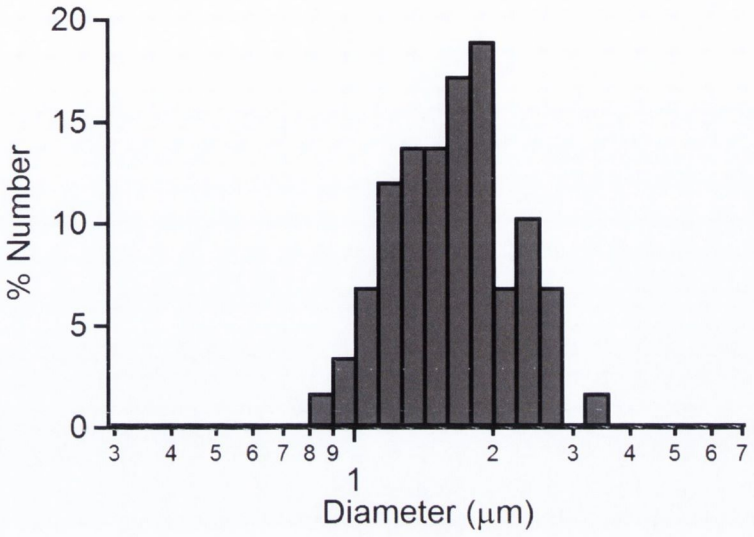

Figure 3.16: Size distribution via SEM of 60 CMs synthesised using 1.0 M NaDCA.

Figure 3.17a shows DLS size distributions obtained for 4 concentrations of NaDCA precursor solution. The plot confirms the assertion made above that DLS does not give an accurate size diameter for NaDCA particles. However, the DLS size distributions do decrease with decreasing concentration, indicating that DLS might perhaps be able to give information about relative particle size. Interestingly, for the 0.125 M solution a wider distribution is observed. This is most likely due to the more intense Raleigh scattering from larger particles having a significant affect on the measurement. Figure 3.17b shows a plot of d^3 vs C where d was determined by averaging at least 3 concurrent DLS measurements for NaDCA. The linear relation observed suggests that DLS might give relative information on particle diameter for NaDCA. Potentially, obtaining SEM size distribution and DLS for 4-5 NaDCA concentrations over a wide concentration range would allow a calibration curve to be made which could allow accurate particle size determination size from DLS measurements. However to this date not enough SEM distributions, over a wide enough range have been obtained; this work is currently being carried out in the laboratory of a collaborator.

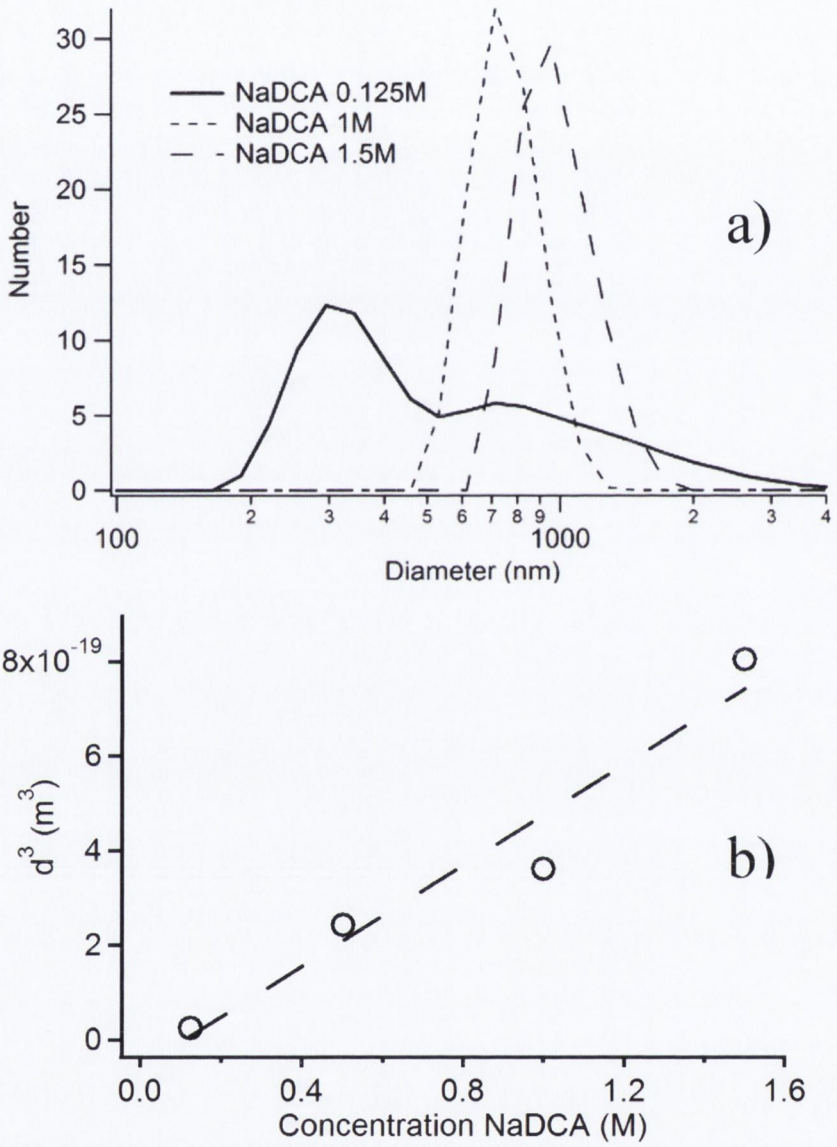

Figure 3.17: a) Typical DLS distributions obtained using NaDCA CMs b) Plot of the particle diameter cubed vs concentration of the NaDCA solution.

In summary, we can control the size of CMs utilising both precursor concentration and piezo disk frequency in agreement with the USP literature and theory. However, results indicate that it is easier to achieve control by just altering the precursor concentration due to the linear behaviour demonstrated above.

3.3.4.3 Surface chemistry and Functionalisation of carbon microspheres

FTIR spectra on CMs indicated the presence of both sp^2 and sp^3 carbon materials, via aromatic carbon stretching modes, aromatic C-H stretching modes, aliphatic C–H stretching modes and methyl bending modes all being present. FTIR spectra also indicated the presence of C-O stretching modes which can be assigned to COO^- groups on the CM surface. Zeta potential data supported this, with negative potentials obtained at all pH values tested, thus indicating a negative surface charge. These results suggest that carbon materials do not undergo complete decarboxylation when they undergo pyrolysis in our USP system. This could be due to carboxylation occurring in the furnace due to the presence of steam at 700 °C. This could be confirmed by performing very short lived heat treatment experiments on the CMs in an inert atmosphere at 700 °C, followed by FTIR experiments. If a drastic reduction in C-O stretching is observed, it would support this hypothesis. If no change is observed, it would indicate that these groups are stable on the carbon surface.

Functionalisation experiments were performed on the CM surface utilising diazonium salt chemistry with three different terminal groups. FTIR data showed drastic changes to spectra obtained for the $-SO_3$ and $-CH_3$ terminating groups. However, whilst an appropriate peak change was observed for the –COOH chemistry, it was challenging to attribute this to covalent grafting due to the presence of substantial peaks in this region on the bare sample. Correspondingly, a relative change of the particle Zeta potential was observed as summarised in table 3.3; the direction of the observed shifts in zeta potential upon functionalisation supports the FTIR results. More negative potentials after both $-COO^-$ and $-SO_3^-$ functionalization is what would be expected for an increase in the density of Arrhenius acid surface groups. Importantly here, the relative difference of the SO_3^- chemistry is greater than that for the $-COO^-$. This is expected if one is to consider that SO_3H is a much stronger acid than COOH and will dissociate more in an aqueous environmentv[28]. So it would be expected to contribute to a more negative charge on CM surface. Coupling the Zeta potential and

FTIR data together, we can conclude that we have successfully functionalised CM surfaces using diazonium grafting reactions.

Terminus group	Potential Difference (mV), pH(3-9)
-COOH	-2.8 ± 0.5 mV
$-SO_3H$	-5.9 ± 0.8 mV
$-CH_3$	+1.0 ± 0.15 mV

Table 3.3: Average Zeta potential difference after surface functionalisation of CMs

These results are of great significance when considering the role CMs might have in any application as a transport module for various molecules and particles. By varying the size, porosity and even the surface chemistry it is possible to tailor design CM transport modules for use in very differing environments.

3.4 Conclusions

We have successfully synthesized spherically shaped carbon particles using USP techniques. We have demonstrated that by changing the precursor solution it is possible to obtain CMs with different morphologies, surface area and porosity. We obtained CMs from LiDCA which were highly spherical, mesoporous morphology and a surface area of 1040 m^2/g. We obtained CMs from NaDCA and KDCA which were both approximately spherical, macroporous morphology and with surface areas of 544 and 618 m^2/g respectively. Our results showed that it is possible to leverage precursor concentration and piezo disk frequency in order to achieve particle size control over CMs. This was demonstrated for both NaDCA and LiDCA produced particles. It has been demonstrated the carbon centres making up the different CM consists of both sp^2 and sp^3 carbon materials, with COO^- surface chemistry moieties also being present. We have also confirmed via FTIR and Zeta potential measurements that it is possible to functionalise and modify the surface of the CM surface using Diazonium salt chemistry.

These results could have implications with regard to potential applications for CMs as transport vehicles in biochemistry far beyond what is discussed in this report [29].

References

(1) Skrabalak, S. E.; Suslick, K. S. *Journal of the American Chemical Society* **2006**, *128*, 12642.

(2) Skrabalak, S. E.; Suslick, K. S. *Journal of Physical Chemistry C* **2007**, *111*, 17807.

(3) Colavita, P. E.; Sun, B.; Tse, K. Y.; Hamers, R. J. *Journal of the American Chemical Society* **2007**, *129*, 13554.

(4) Allongue, P.; Delamar, M.; Desbat, B.; Fagebaume, O.; Hitmi, R.; Pinson, J.; Saveant, J. M. *Journal of the American Chemical Society* **1997**, *119*, 201.

(5) D'Amour, M.; Bélanger, D. *The Journal of Physical Chemistry B* **2003**, *107*, 4811.

(6) Hermans, A.; Seipel, A. T.; Miller, C. E.; Wightman, R. M. *Langmuir* **2006**, *22*, 1964.

(7) Brunauer, S.; Emmett, P. H.; Teller, E. *Journal of the American Chemical Society* **1938**, *60*, 309.

(8) Barrett, E. P.; Joyner, L. G.; Halenda, P. P. *Journal of the American Chemical Society* **1951**, *73*, 373.

(9) Sing, K.; Everett, D.; Haul, R.; Moscou, L.; Pierotti, R. *Pure Appl. Chem* **1985**, *57*, 603.

(10) Ferrari, A.; Robertson, J. *Physical Review B* **2000**, *61*, 14095.

(11) Casiraghi, C.; Ferrari, A. C.; Robertson, J. *Physical Review B* **2005**, *72*.

(12) Ferrari, A. C.; Robertson, J. *Physical Review B* **2000**, *61*, 14095.

(13) Akhter, M.; Chughtai, A.; Smith, D. *Applied Spectroscopy* **1985**, *39*, 143.

(14) Smith, D.; Chughtai, A. *Colloids and Surfaces A: Physicochemical and Engineering Aspects* **1995**, *105*, 47.

(15) Socrates, G. *Wiley* **2001**.

(16) Moreno-Castilla, C.; Lopez-Ramon, M.; Carrasco-Marın, F. *Carbon* **2000**, *38*, 1995.

(17) Yang, J.; Zou, L.; Choudhury, N. R. *Electrochimica Acta* **2012**.

(18) Suganuma, S.; Nakajima, K.; Kitano, M.; Kato, H.; Tamura, A.; Kondo, H.; Yanagawa, S.; Hayashi, S.; Hara, M. *Microporous and Mesoporous Materials* **2011**, *143*, 443.

(19) Rivera-Utrilla, J.; Bautista-Toledo, I.; Ferro-Garcia, M. A.; Moreno-Castilla, C. *Journal of Chemical Technology and Biotechnology* **2001**, *76*, 1209.

(20) Berne, B.; Pecora, R. *Dover Publications, Mineola, New York*.

(21) Chu, B. *Laser Light Scattering: Basic Principles and Practice, 2007*.

(22) Johnson, S. A.; Gabriel, D. A. *Laser Light Scattering, 1994*.

(23) Yoshikawa, M.; Katagiri, G.; Ishida, H.; Ishitani, A.; Akamatsu, T. *Journal of applied physics* **1988**, *64*, 6464.

(24) Bubenzer, A.; Dischler, B.; Brandt, G.; Koidl, P. *Journal of applied physics* **1983**, *54*, 4590.

(25) Lang, R. J. *Journal of the Acoustical Society of America* **1962**, *34*, 6.

(26) Barreras, F.; Amaveda, H.; Lozano, A. *Experiments in Fluids* **2002**, *33*, 405.

(27) Lozano, A.; Amaveda, H.; Barreras, F.; Jorda, X.; Lozano, M. *Journal of Fluids Engineering-Transactions of the Asme* **2003**, *125*, 941.

(28) Baranton, S.; Bélanger, D. *The Journal of Physical Chemistry B* **2005**, *109*, 24401.

(29) Duffy, P.; Magno, L. M.; Yadav, R. B.; Roberts, S. K.; Ward, A. D.; Botchway, S. W.; Colavita, P. E.; Quinn, S. J. *Journal of Materials Chemistry* **2012**, *22*, 432.

Chapter 4

Synthesis of Metal/Carbon composites via Green Electroless Deposition

Composite materials are of interest because they can potentially combine the properties of their respective components in a manner that is useful for specific applications [1]. Here, we report on the use of coffee as a low-cost, green reductant for the room temperature formation of catalytically active, supported metal nanoparticles. This chapter describes the characterisation of these composites using various techniques, followed by experimental results demonstrating the catalytic activity of the composite materials synthesized.

4.1 Introduction

In this chapter we report on the use of coffee as a low-cost, green reagent for electroless deposition at room temperature. We have leveraged the reduction potential of coffee in order to grow Pd and Ag nanoparticles at the surface of porous carbon microspheres (CM) synthesized via ultraspray pyrolysis. We have characterized the structure, morphology and composition of these palladium/carbon (Pd/CM) and silver/carbon (Ag/CM) composite microspheres using a combination of Scanning Electron Microscopy (SEM), Energy Dispersive X-ray Spectroscopy (EDS), X-ray diffraction (XRD) and thermogravimetric analysis (TGA). Finally, in order to demonstrate that the resulting electrolessly deposited Pd^0 and Ag^0 nanoparticles display typical surface chemistry for the corresponding metal, we show that the Pd/CM and Ag/CM composites are catalytically active in Suzuki coupling and reduction reactions, respectively. Our results show that coffee can be used as a green reducing agent in surface catalysed electroless deposition and that carbon supported nanoparticles obtained via this new methodology display good performance as heterogeneous catalysts for organic synthesis. On the light of our reactivity studies we also discuss the potential consequences of using natural extracts in the synthesis of metallic nanoparticles for catalytic applications.

4.1.1 Carbon support material

CM's previously synthesised (See section 3.2.2) were selected as the scaffold for a metal nanoparticle/carbon composite material. They have potential for use in an ED synthesis to obtain nanoparticle for several reasons. FTIR spectra of the CMs indicated the presences of –COOH groups on the surface. Following on from the work of Metz et al and others [2-4], these groups should provide an excellent anchoring location for noble metallic catalytic seed particle at a carbon surface. Furthermore, catalytic seed

anchoring can potentially be managed, if necessary by utilising surface chemistry controls previously demonstrated. Also, the tuneable pore sizes could be leverage as a template for controlling nanoparticle growth. As mass transport and diffusion play a role in particle growth kinetics, having CM's with high-specific surface areas and porosities could be an advantage leveraged for creating different nanostructures. See section 1.5.3 for a detailed discussion on methods for obtaining nanoparticles via ED.

4.1.2 Reduction of metal ions using coffee

Recently, Varma and co-workers [5,6] have shown that coffee solutions can be used to reduce M^{n+} ions to form nanoparticles in solution. The exact identity of the active reducing agent in the coffee remains unclear, although it has been hypothesized that either caffeine [5] or polyphenols [6,7] could be responsible for metal reduction. In fact, previous work has shown that other components of coffee that are unrelated to caffeine have a reduction potential sufficiently negative to spontaneously reduce $PdCl_4^{2-}$ and $Ag(NH_3)_2^+$ ions in solution [8]. Also, Gentry et al has demonstrated the use of hydroquinone as a reducing agent for Ag ions on pre-existent Ag clusters [9].

The main advantage of nanoparticle synthetic strategies based on natural extracts as reductants is the environmentally benign nature of the reducing agents. However, a potential drawback of such an approach consists in the simultaneous presence of several natural compounds in the reductant mixture; in the case of coffee, solutions contain a complex mix of proteins, lipids, polysaccharides, small organic molecules and inorganic compounds [10]. Many of these molecules can strongly physisorb and cap metallic nanoparticles, thus blocking surface sites and potentially limiting their applications in areas such as catalysis or sensing.

4.2 Experimental

4.2.1 Materials and reagents

Tin chloride dihydrate (96%, Fisher), palladium chloride (Fisher), silver nitrate (99% Sigma), sodium borohydride (98% Sigma), sodium hydroxide (97% Sigma), dichloroacetic acid (99% Sigma), trifluoroacetic acid (TFA, 99% Sigma), ammonia (28% Romil), 4-nitrophenol (95% BDH), hydrochloric acid (37.5% Sigma), Bromotoluene (98% Aldrich), phenylboronic acid (97.0% Aldrich) sodium carbonate (99.5% Fisher), methanol (99.99% Pharmco-Aaper), tetrahydrofuran (THF, 99.9% Sigma), hexanes (99.9%, Fisher), and decaffeinated coffee (Nescafe Original decaff) were used as received.

4.2.2 Synthesis of carbon and metal/carbon microspheres

CMs were synthesized using ultrasonic spray pyrolysis as previously reported in section(3.2.2) [11,12]. CMs were generated from a 1.5 M solution of NaDCA. The preparation of Ag/CM composite particles consisted of three steps: (a) sensitization with tin chloride, (b) nucleation of Ag^0 at the CM surface and (c) growth of Ag^0 particles using coffee. CMs were added to 25 mL of a 0.050 M $SnCl_2$ solution in 0.070 M aqueous TFA, to a final CM concentration of 0.2400 g L^{-1}; the CM suspension was briefly sonicated and left at room temperature for 30 min to allow for adsorption of Sn^{2+} ions at the CM surface. The suspension was then filtered and washed with water and ethanol. CMs were then placed in 10 mL of a 0.003 M $Ag(NH_3)_2^+$ solution (ammoniacal silver nitrate or Tollens' reagent), sonicated for 5 s and left for 30 min to allow for Ag^0 to nucleate at the surface. A solution of decaffeinated coffee was prepared by adding 1.0 g of coffee powder to 200 mL of water and filtered using 0.45 μM nylon membranes; 40 mL of this coffee solution were added to the 10 mL CM suspension in $Ag(NH_3)_2^+$ solution at room temperature and left to react for 5 min. The

resulting Ag/CM composite particles were then washed to remove silver salts and excess nanoparticles via centrifugation/washing cycles in Millipore water and ethanol. The preparation of Pd/CM composites was carried out as for Ag/CM microparticles except for the use of an acidified 5 x 10^{-3} M $PdCl_2$ solution (pH 1) instead of ammoniacal silver solution. Control experiments that omitted the Sn - sensitisation step were carried out in identical manner, except for immersion of CM's into a $SnCl_2$ solution.

4.2.3. Reactivity studies

4.2.3.1 Ag/CM reactivity

Nitroaromatic reduction reactions were carried out inside a UV - Vis cuvette at room temperature. A freshly prepared 0.0103 g L^{-1} dispersion of Ag/CM in a 1.0 x 10^{-2} M aqueous $NaBH_4$ solution was placed in a cuvette. 4-Nitrophenol was added to a final concentration of 1.0 x 10^{-5} M to the cuvette, which was stirred vigorously and placed inside the UV-Vis spectrometer. Spectra in the region 280-500 nm were taken at regular time intervals in order to monitor changes in 4-nitrophenol concentration. Control experiment containing pristine CMs were ran to ensure CMs had no effect on the measurement.

4.2.3.2 Pd/CM reactivity

Coupling reactions were carried out by mixing 1.0 mg of Pd/CM, 122.0 mg (1 mmol) phenylboronic acid, 171.0 mg (1 mmol) 4-bromotoluene, and 116.0 mg (2 mmol) Na_2CO_3 in 20 mL of a 2:2:1 methanol:H_2O:THF solution in a sealed plastic vial. The reaction vial was agitated overnight on a mechanical shaker table at room temperature. The Pd/CM catalysts were removed by centrifugation. The reaction

products were extracted with hexanes, dried with magnesium sulphate, and then put on a rotary evaporator to remove excess solvent. The dried solid product was dissolved in methanol and analyzed by Gas-Chromatography-Mass Spectrometry (GC-MS), as previously reported [13].

4.2.4. Characterization techniques

Scanning electron microscopy: SEM was performed at an accelerating voltage of 10 keV using a Zeiss Ultra microscope equipped with an Energy Dispersive X-ray Spectroscopy (EDS) detector (Oxford Instruments INCA system with silicon drift detector (SDD)). Samples were prepared by drop casting on Si wafers from dispersions of the composite powder. Elemental analysis was carried out using the commercial protocol provided with the EDS detector at an accelerating voltage of 20 KeV. This approach has been shown to provide semiquantitative estimates with relative error ≤ 25% [14]. **Thermal Gravimetric Analysis:** TGA measurements were performed using a Perkin-Elmer Pyris 1 TGA using air as a carrier gas and a heat ramp of 10 °C min^{-1}. Thoroughly washed samples at least 1 mg in weight were used for TGA studies. Samples were held at 200 °C in order to desorb physisorbed water prior to initiating the measurement ramp; masses were normalised to the weight of carbon particles at 200 °C. **X-ray diffraction**: XRD was carried out on a Siemens D500 diffractometer with monochromated Cu Ka radiation; pattern analysis was carried out using commercial XRD software (EVA, Bruker). Samples were prepared by supporting Metal/CM composites on nylon membranes. **UV-Vis**: UV-VIS spectra of nitro - aromatics were obtained on a Shimadzu UV-2401PC. Measurements were taken at a rate of 120 nm per second at 0.2nm intervals and a slit width of 1nm. **Gas Chromatography - Mass Spectrometry**: GC- MS was performed using an Agilent model 6890 gas chromatograph coupled with a model 5973 mass spectrometer in order to identify and quantify the Suzuki coupling reaction products. GC-MS samples were separated on a

HP-5MS column, using an injection temperature of 50 °C, followed by a 10 °C ramp per minute to 250 °C with a final 4 min hold.

4.3. Results

The results will be laid out in two parts: i) Results for synthesis and characterisation of the metal/composites, ii) Results for the catalytic activity of the Metal/Carbon composites materials. These sections will be followed by a discussion section.

4.3.1. Synthesis and characterisation of metal/CM composites

Characterisation of Metal/CM composites will be discussed in this section. How the chemistry of each step in figure 4.1 effects the resultant composite material will be examined followed by subsequent characterisation of Metal/Carbon composites obtained.

4.3.1.1 Synthesis and characterisation of activated CM

In order to obtain metal/carbon composite microspheres, CMs underwent a two step sensitisation and activation protocol [15].

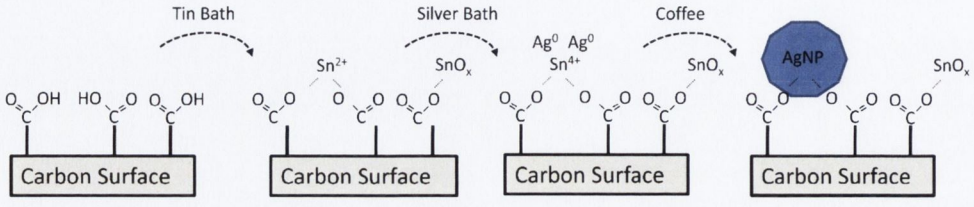

Figure 4.1: Process for synthesizing Ag nanoparticles supported onto a carbon microsphere surface.

Figure 4.1 shows a schematic representation of what is happening at the surface. First, the carbon surface was sensitised in a solution of Sn^{2+} ions. The Sn^{2+} ion is known to undergo complexation and ion-exchange at carbon surfaces containing carboxylate groups [3]. The Sn^{2+} ion acts as a pathway for achieving anchoring of noble metallic catalytic particle seeds on the surface. After washing of CM's, a galvanic exchange was carried out with $PdCl_4^{2-}$ or $Ag(NH_3)_2^+$ ions in solution and the Sn^{2+} ion located on the CM surface. Equations 4.1, 4.2 and 4.3 indicate that this exchange is thermodynamically favoured due to $PdCl_4^{2-}$ and $Ag(NH_3)_2^+$ both having a higher reduction potential than the Sn^{4+}/Sn^{2+} redox couple [15-17].

$$Sn^{2+} \rightleftharpoons Sn^{4+} + 2e^- \qquad E_0 = -0.151\ V \qquad \text{(eqn 4.1)}$$

$$[PdCl4]^{2-} + 2e^- \rightleftharpoons Pd^0 + 4Cl^- \qquad E_0 = +0.591\ V \qquad \text{(eqn 4.2)}$$

$$[Ag(NH_3)_2]^+ + e^- \rightleftharpoons Ag^0 + NH_3 \qquad E_0 = +0.38\ V \qquad \text{(eqn 4.3)}$$

This galvanic exchange results in the formation of catalytic Pd^0 and Ag^0 metallic centres on the CM's surface and the production of Sn^{4+} ions as shown in figure 1 [18-20].The metallic centres will act as our catalytic source for further ED and NP synthesis.

These metallic centres can subsequently serve as sites for further reduction of the metallic salt in solution by use of a reduction agent. In this work, the reducing agent was commercial decaffeinated coffee. Figure 4.2a and b shows the result of silver and palladium reduction using coffee at an activated CM surfaces. Metallic particles and clusters can be clearly seen in the SEM images. Figure 4.2a shows metallic silver nanoparticle aggregates obtained by this method, which were found to have sizes in the range 100 - 200 nm and consist of individual smaller particles approximately 30 nm in diameter. Figure 4.2b shows small and well dispersed Pd^0 nanoparticles with diameters of approximately 25 nm with little or no observed aggregation. However, SEM images also showed Pd and Ag particles which were not anchored to any carbon surface, which indicated that homogeneous reduction occurs in the ED solution. This is

not unexpected, as Varma et al used this protocol specifically to reduced M^{n+} ions from solution, in order to form nanoparticles [5,6].

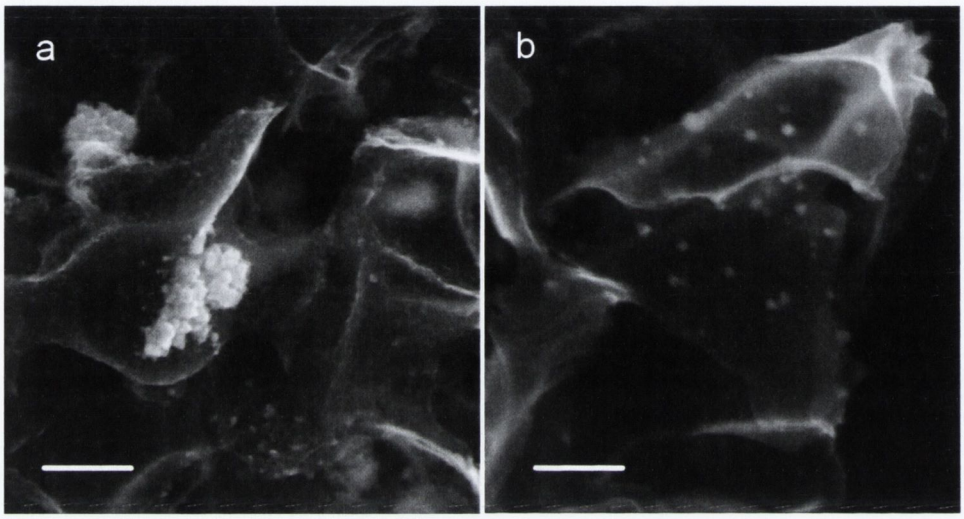

Figure 4.2: Typical SEM images of the Ag (a) and Pd (b) carbon microspheres obtained by using coffee as a reductant, 3 mmol solution $Ag(NH_3)_2$ (a) and (b) 5 mmol solution $PdCl_2$; Scalebar = 200 nm.

However, these unanchored particles could suggest that metallic particles seen in Figure 4.2a and 4.2b are homogeneously produced and simply settle on the carbon particle surface. As SEM sample were prepared via drop cast method, this mechanism and interpretation was entirely possible. To prove that particles seen on CM surface were produced via heterogeneous catalysis, Control experiments that omit the Sn sensitisation step during the synthesis were performed. Figure 4.3a shows Ag/C performed without sensitisation, this led to the formation of few large Ag aggregates up to 800 nm in diameter, most of which were found to be in suspension instead of being anchored onto the CM surface. Similarly, figure 4.3b shows the omission of the sensitization step during Pd deposition. This led to the formation of unsupported Pd nanoparticles 20 - 40 nm in diameter, with very few particles appearing on the CM surface. These particles are in the same size range as unsupported particles observed while using sensitisation techniques for composite

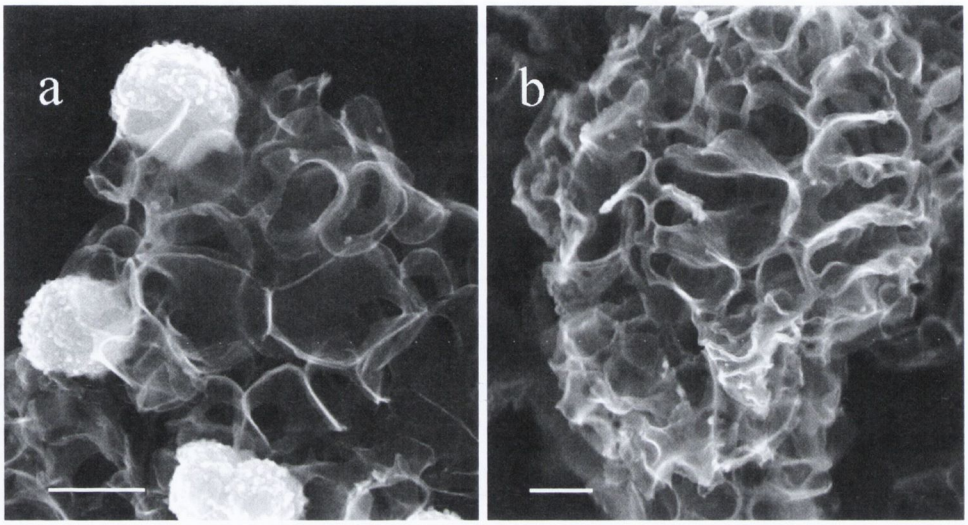

Figure 4.3: Control experiments excluding Sn sensitisation step for Ag/CM (a) and Pd/CM (b) composite synthesis; scalebar = 500 nm.

production. These results coupled together indicate that both heterogeneous and homogeneous reductions are occurring simultaneously in the deposition solution. Control experiments also indicate that Sn sensitization plays an important role in controlling surface immobilisation of the metal nanoparticles formed at carbon microspheres interfaces.

To the best of our knowledge, sensitisation and activation procedures have never been performed on CM's synthesized from USP before. Further characterisation and investigation was performed on the sensitisation process, in order to understand how it affects metal NP size and distribution on the CM surface. Due to the surface chemistry of the CM's (See section 3.3.3), sensitisation and activation chemistries were not expected to perform identically to previously reported experiments on carbon fibres and carbon nanotubes. Therefore, Sn^{2+} sensitisation was performed at three concentrations for 30 min, followed by subsequent activation in a solution of 30 x 10^{-3} M $PdCl_2$ for 30 min. The $PdCl_2$ concentration was increased for these experiments to eliminate any effects on the system due to limited metallic ion concentration. Metallic

ion exhaustion due to increased nucleation at higher Sn^{2+} is possible, resulting in bath failure and inaccurate results. Also, competitive homogeneous reductions could potentially consume more metal ions, making this a valid concern for the experiment. Figure 4.4a-c shows SEM images demonstrating the surface of the CMs after undergoing this procedure for 8, 50 and 100 mmol solutions of Sn^{2+} respectively. Firstly, figure 4.4 demonstrates that CMs surfaces can be modified by the sensitisation and activation processes. Growth of small spherical particles is clearly visible on the CM surfaces for all three sensitisation conditions. These particles are not visible on pristine CMs surfaces imaged in section 3.3.1 indicating that the growth is a direct result of the sensitisation and activation steps. Secondly, the images demonstrate that Sn^{2+} ion concentration has an effect on the extent of catalytic seed nucleation for the given reaction time of 30 mins performed for sensitisation and activation. From comparing the 8, 50 and 100 mmol samples above, it is observed that increased surface modification occurs in the sample with higher Sn^{2+} concentration. Not many metallic nucleating sites can be observed in 8 mmol sample when comparing to 50 and 100 mmol, indicating that initial Sn^{2+} concentration is an important parameter for achieving adequate and successful catalytic seeding on carbon surfaces produced from USP. Also, surface modification appears greater in the 100mmol sample when compared to the 50 mmol, however the difference is not as clearly defined as in samples shown in figure 4.4a and b. The resolution limitations of the SEM make this assertion difficult to quantify when looking at particles so small, particularly for samples with significant modification like b and c. This makes the conclusions above semi-quantitative. However, from many CMs observed via SEM the assertion holds true and images are representative of the activated/reduced samples as a whole. See section 4.3.3.1 for discussion.

Sensitised and activated samples were each subsequently reduced in a solution of coffee to produce the Pd/C composite material for each condition in Figure 4.4a-c.

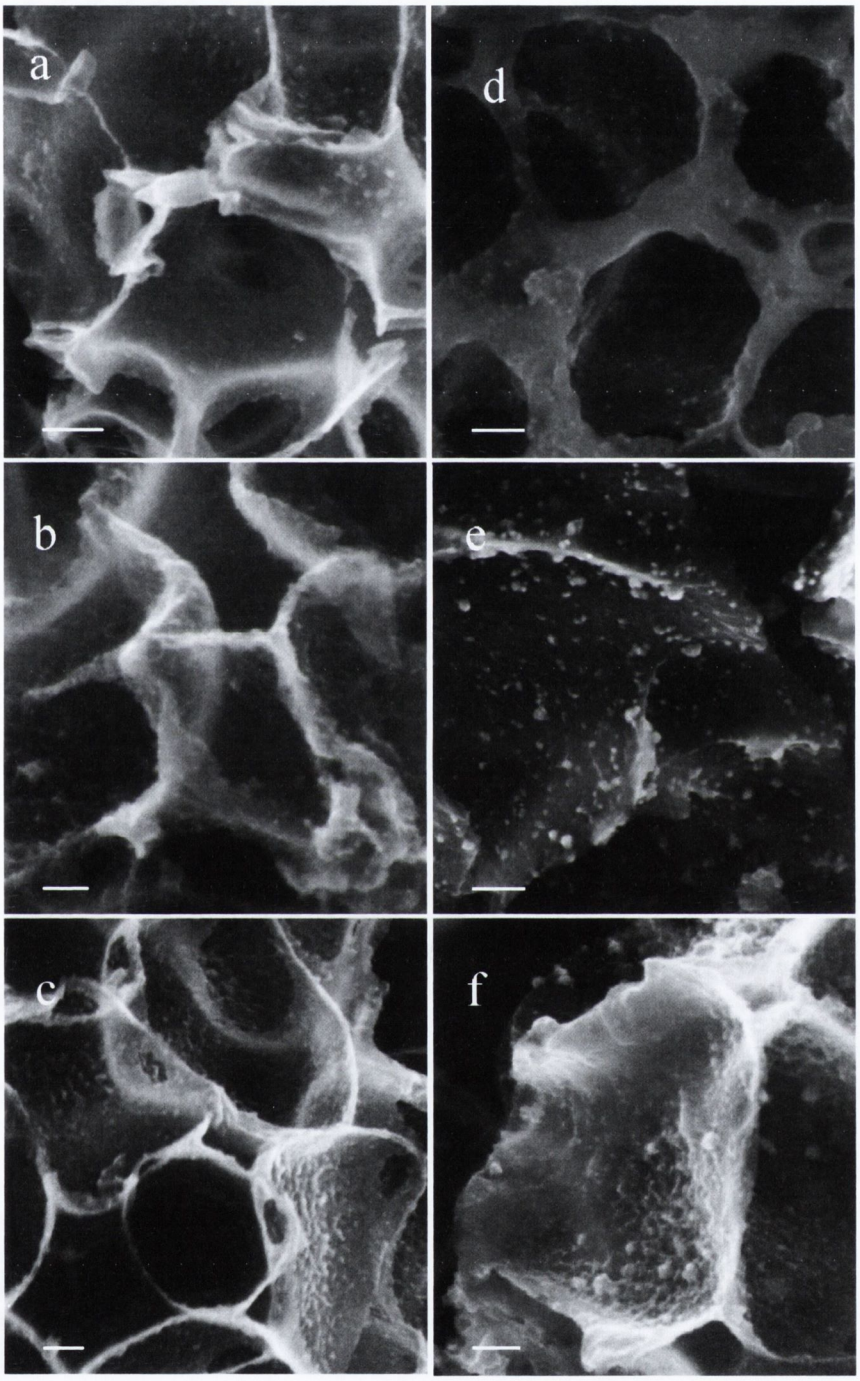

Figure 4.4:(a-c) Surface modification caused by sensitisation and activation using 8 mmol (a), 50 mmol (b) and 100mmol (c) Sn^{2+} in the sensitisation step. Figure 4(d-f) Resulting electroless depositions from activations observed in figure 4.4a-c, respectively. Scalebar = 100 nm, except b = 50 nm

This was performed to help understand, the role that the sensitisation step has on nucleation of catalytic seed particles and subsequently, the effect this has on metallic particles post reduction. Figure 4d-f demonstrates the three conditions seen in figure 4.4a-c undergoing ED via reduction by coffee. Comparing figure 4.4d and e, a significant difference in dispersion of the metallic particle on the CM surface is observed between the two samples. In Figure 4.4d, particles are approximately 4-15nm in size, with particles located relatively far apart, dispersed and not aggregated. Figure 4.4e shows particles which are again in the 4-15nm particle size range. However, in this sample catalytic seed particles are more concentrated at the surface when compared to the 8 mmol samples. Also, deposition occurs in such a concentrated manner that many clusters consisting of multiple nanoparticles are observed to form on the CM surface. Each cluster appears to consist of nanoparticles in the 10-20nm range. Figure 4.4f shows reduction after the 100 mmol sensitisation with Sn^{2+}. This sample has similar properties to the 50 mmol sample. Particles are again observed in the 10-20nm range, with many particles being grouped together in the form of nanoparticle aggregates. Again, due to the qualitative analysis performed, it is impossible to say with certainty whether nucleation of higher density occurs on the 100 mmol sample as compared to the 50 mmol, however, it is clearly evident that greater difference is observed between samples d and e in the above figures. These results indicate that the sensitisation step influences the density of growth for metallic particles with greater concentrations of Sn^{2+} resulting in more particles and particle aggregates. It was also observed that particle size appears to not exceed 40 nm indicating that although Sn does have a role in initial growth rates, it may not be the determining factor for ultimate particle size in ED chemistry displayed here.

Images from figures 4.2b and 4.4e show samples which had the same sensitisation step but differed in $PdCl_2$ concentration. This resulted in different dispersions of Pd nanoparticles at the CM surface, with sample 4.2b having no visible clusters of NPs and much less particle nucleation when compared to 4.4e. As both samples had the same

initial Sn^{2+} concentration, this indicates that metallic ion concentration does have an effect on the dispersion of metallic nanoparticles formed at the CM surface.

Figure 4.5a and 4.5b show composite synthesis of Ag/C composite material with identical sensitisation steps for two different concentrations of 0.3 and 30 mmol $Ag(NH_3)_2^+$ respectively.

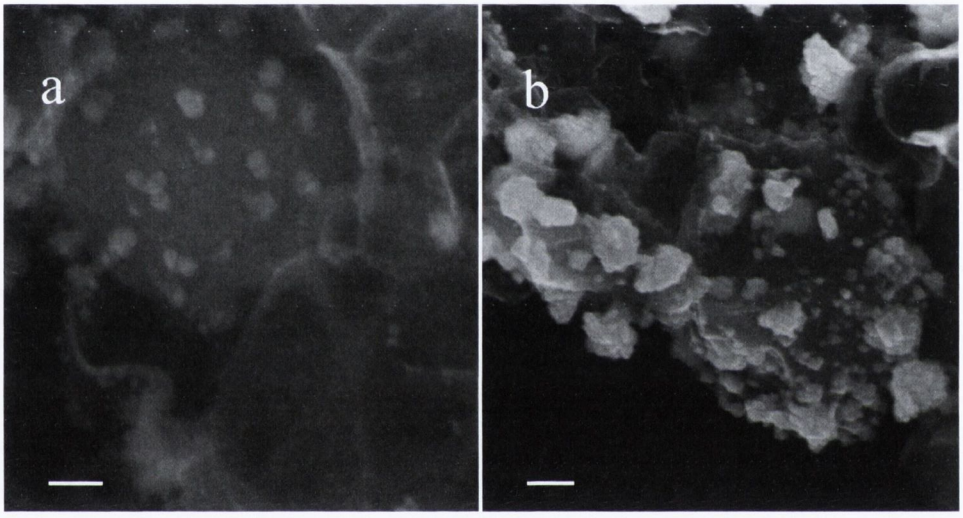

Figure 4.5: Ag/CM synthesized using 0.3 mmol (a) and 30 mmol (b) $Ag(NH_3)_2^+$;scalebar (a) = 100 nm Scalebar (b) = 200nm

These figures can be directly compared to figure 4.2a where 3 mmol concentration was used. Figure 4.5a-b show nucleated NPs at the CM surface for both concentrations, indicating that Ag/C synthesis is possible at multiple concentrations over these ranges. For both figures, particles are approximately 30 nm in diameter which is comparable to NPs synthesized using the 3 mmol concentration. However, cluster size appears to vary between the samples. Cluster sizes of sub 100 nm for the 0.3 mmol soln, 100 – 200 nm for the 3 mmol soln and greater than 200 nm for the 30 mmol soln are observed. Importantly, all these clusters consist of NPs which have a diameter of approximately 30 nm, indicating a limit to particle growth and size. Results are summarised in table 4.1.

Metal conc (mmol)	Particle size (nm)	Cluster size (nm)	Cluster density (Rel)
0.3	30	> 100	Low
3	30	100 – 200	Med
30	30	< 200	High

Table 4.1: Summary of the effect of metal ion concentration on particle growth at the CM surface

The table suggests that metal ion concentration is not the limiting parameter for particle size of Ag^0 over these concentration ranges. However, particle density over the CMs surface can be controlled and influenced by varying the metallic ion concentration. Also, Particle sizes in clusters for both Pd^0 and Ag^0 particles indicate that some other limiting parameter is responsible for restrictive NP particle growth, which is unrelated to metal ion or Sn^{2+} concentration.

Figure 4.6a, b shows typical XRD patterns obtained from Ag/CM and Pd/CM composite microspheres, respectively. Figure 4.6a shows reflections at 38.12°, 44.28° and 64.46°, respectively. These peaks can be matched with the (111), (200) and (220) reflections characteristic of fcc silver, (JCPDS file no. 04- 0783) [21,22]. A small peak is observed at 32.5° which can be assigned to the (111) peak of Ag_2O, indicating the presence of a surface oxide layer. Figure 4.6b shows reflections at 40.12°, 46.66° and 68.10° respectively. These peaks can be matched to the (111), (200) and (220) reflections characteristic of fcc palladium, (JCPDS file no. 05-681). XRD measurements of bare CMs showed that the carbon scaffold only contributes a broad background to the pattern. No peaks associated to tin-containing species could be detected in XRD patterns, thus suggesting that tin remaining after sensitization is mostly present in non-crystalline form. The distance d, between the Miller planes associated with each of these reflections can be calculated using Bragg's law (Eq 4.4)[23].

$$n\lambda = 2dSin\theta \qquad \text{(eqn 4.4)}$$

Here, λ is the wavelength of the X-ray radiation source, θ is the diffraction angle and n is an integer relating to the order of the reflection. The 2θ value of the angle of the

detector with respect to the incident direction of radiation shown in the data above is used to obtain θ for the Bragg equation.

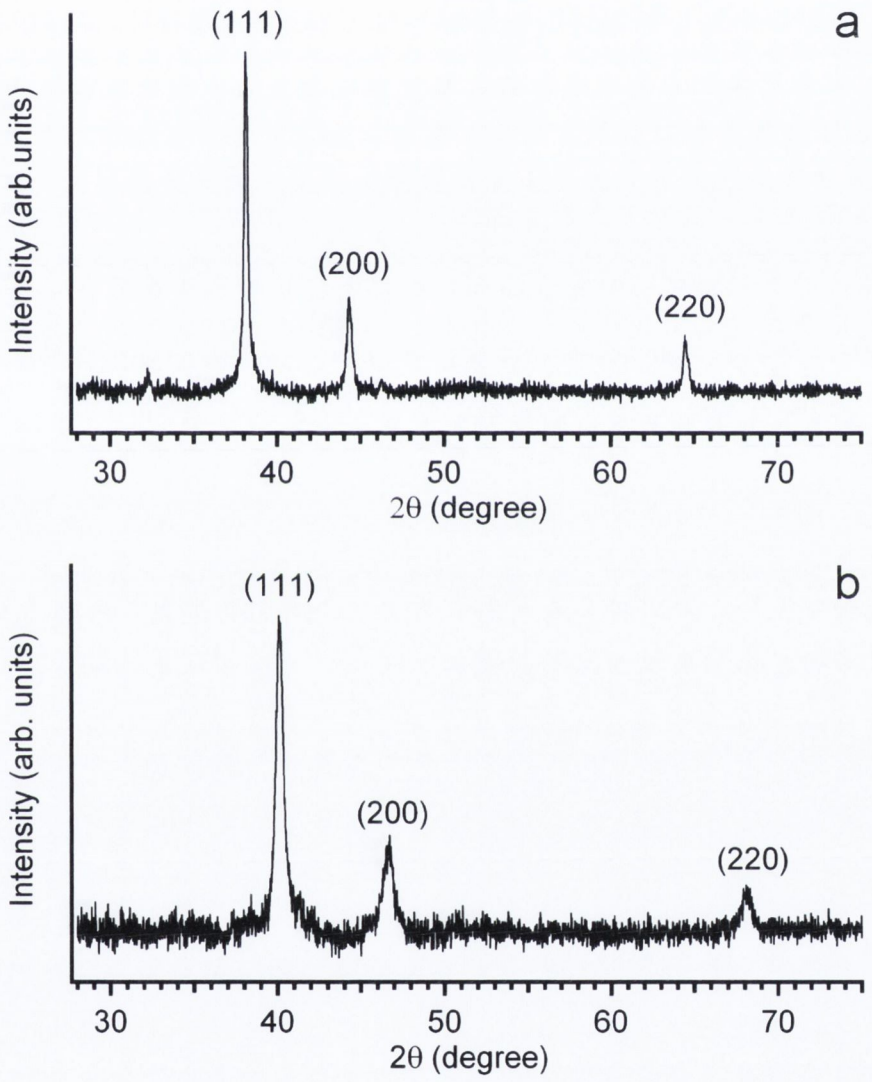

Figure 4.6: XRD patterns obtained from the Ag/CM (a) and Pd/CM (b) samples.

Also, for the data above, n will be equal to one. The value d can then be used to calculate the lattice constants for a tetragonal elementary cell using eqn 4.5 [23].

$$\frac{1}{d^2} = \frac{(h^2 + k^2)}{a^2} + \frac{l^2}{c^2} \qquad \text{(eqn 4.5)}$$

Where, h, k and l are the miller indices of the peak, and the cell lattice constants are denoted by a and c. For cubic cells a = c, therefore, for the data above, eqn 4.5 can be reduced to eqn 4.6.

$$c = \sqrt{d^2(h^2 + k^2 + l^2)} \qquad \text{(eqn 4.6)}$$

Where c is the lattice constant of a cubic crystal cell. Utilising this, the three reflections from figure 4.6a yield an average lattice constant of 4.086 Å for the Ag/C composite, matching the literature values for metallic fcc silver. The reflections from fig. 4.6b yield an average lattice constant of 4.89 Å for the Pd/C composite, matching the literature value of 3.8908 Å for metallic fcc palladium. In summary, XRD results indicate that the particles deposited at the CM surface via green electroless deposition protocols contain metallic Pd and Ag particles.

In order to determine the metal loading of metal/CM composites we carried out TGA and EDS measurement; Figure 4.7 shows TGA data for bare CMs, Ag/CMs and Pd/CMs obtained in air in the range 200-900 °C. The curve for bare CMs shows that mass loss due to oxidation occurs in the range 450-650 °C with the largest mass loss rate occurring at 624 °C. In this temperature range the mass loss can be attributed to the combustion of the graphitic carbon scaffold. A residual mass of (3.0 ± 2.0)% at 900 °C is due to insoluble inorganic salts/oxides formed during NaDCA pyrolysis. TGA curves obtained from Ag/CM shows a maximum mass loss rate at 624 °C, in agreement to that observed in the case of bare CMs.

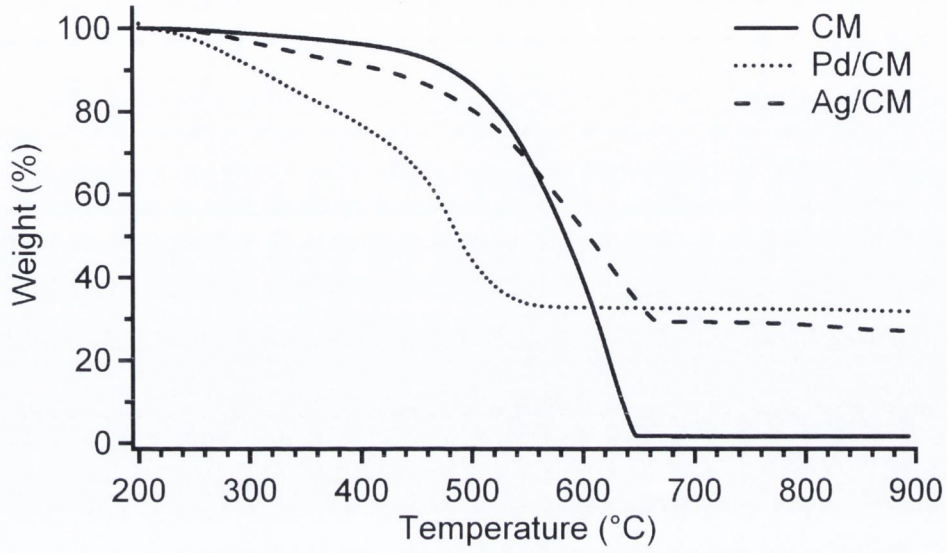

Figure 4.7: TGA curves obtained in air for pristine CMs, Ag/CM and Pd/CM composites.

In the case of Pd/CM samples, the maximum mass loss rate occurs at a significantly lower temperature of 483 °C. This is in agreement with previous reports showing that Pd nanoparticles are catalytically active towards oxidation of carbon fibers and particles [24]. The residual mass obtained from Ag/CMs and Pd/CMs after oxidation at 900 °C was (30 ± 2.0)% and (36 ± 4)%, respectively. These values are larger than those obtained from bare CMs, as expected of particles having undergone sensitization, activation and nanoparticle deposition. Since tin remains as Sn^{4+} at the surface after sensitization steps [25], we can assume that the excess residual mass consists of SnO2 [26,27] and Ag^0 or Pd^0 particles. Although both Ag and Pd metal form oxides when heated in air, these oxides decompose at temperatures below 900 °C [28-30], the end-point temperature in TGA curves reported in Fig. 8. Therefore, we can attribute any residual mass remaining to (a) electrolessly deposited nanoparticles in the form of metallic Ag^0 or Pd^0 and (b) SnO_2 species due to remaining Sn^{4+} after the sensitisation step. EDS analysis of the Ag/CM and Pd/CM composite microspheres shows that they contain tin: 70.2% and 245% for Sn/Ag and Sn/Pd (a/a%), respectively. This is due to the sensitization process, in agreement with reported studies of sensitization/activation mechanisms [25,31]. After correction of the residual masses in

Figure 8 for Sn content obtained from EDS results (assuming it arises from SnO2) and for inorganic compounds resulting from carbon pyrolysis, the estimated Ag/C and Pd/C mass ratios are (13.5 ± 1.5)% and (7.4 ± 1.0)% w/w, respectively. Ag/C ratios are comparable to loadings achieved previously by alternative methods on other carbon scaffolds [3,32-34]. Also, Pd/C loadings are in the range of those found in commercial Pd/C catalysts (5-30%). Finally, Ag/CM and Pd/CM samples show a small but noticeable mass loss in the region 285-340 °C upon oxidation, that is absent in the case of bare CMs. This result indicates that a significant amount of organic compounds remain adsorbed at the metal/CM particle surface after metal reduction and multiple particle washes. Possible implications of the presence of adsorbed organics are discussed in more detail in section 4.3.3.2.

4.3.2 Catalytic activity of metal/carbon composite materials

In order to demonstrate that nanoparticles synthesized via green electroless deposition using coffee display the characteristic interfacial chemistry of metallic nanoparticles, we carried out catalytic studies on Ag/CM and Pd/CM composites using two test heterogeneous reactions. Firstly, the catalytic reduction of p-nitrophenol is used to demonstrate the activity of the Ag/C composite. Pal et al [35] and Esumi et al [36] were the first to identify this as a suitable reaction for testing the catalytic activity of free or supported nanoparticles. Secondly, to demonstrate the catalytic activity of the Pd/CM composite materials synthesised using green strategies, we employed the Suzuki coupling reaction [37]. Suzuki coupling has been of particular interested for supported Pd catalysts and will therefore be ideal for our studies [38].

4.3.2.1. Reduction of 4-nitrophenol using Ag/CM composites

We investigated the activity of Ag/CM composites in the catalytic reduction of 4-nitrophenol to 4-aminophenol by sodium borohydride. The reduction is thermodynamically favourable (E_0 for 4-NP/4-AP = – 0.76 V and H_3BO_3/BH_4^- = –1.33 versus NHE [35]), however, the reduction rate of 4-nitrophenol is negligible in aqueous solutions of $NaBH_4$. Kinetics are catalysed by the presence of noble metal nanoparticles [39-41]. Figure 4.8 shows time-dependent UV - Vis spectra of Ag/CM aqueous suspensions containing 1.0 X 10^{-2} M NaBH4, after injection of 4-nitrophenol to 1.0 X 10^{-5} M concentration. UV - Vis spectra have been corrected due to scattering contributions from the carbon microsphere suspension according to published methods [42].

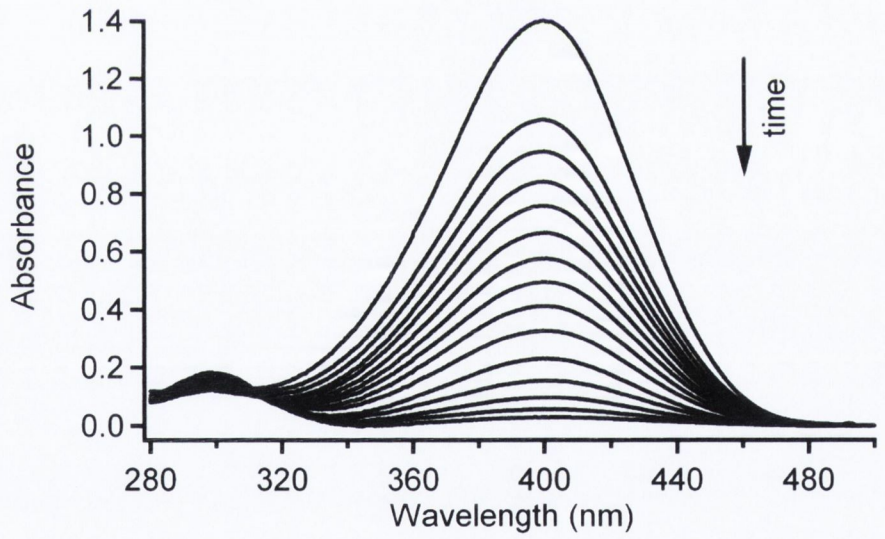

Figure 4.8: Evolution of the UV-Vis absorption spectra of 4-nitrophenol in the presence of 1.0 x 10^{-2} M $NaBH_4$ and Ag/CM particles as a function of reaction time; all spectra were corrected for scattering [42]. The first spectrum was taken immediately afterinjection of 4-nitrophenol, whereas the last spectrum was taken after 27 min.

The maximum at 400 nm is characteristic of 4-nitrophenolate ions in solution [23,36]. The peak decreased rapidly after injection into the Ag/CM:NaBH4 suspension, indicating that the arylnitro group is consumed over time. The graph also shows the appearance of a peak at 290 nm, which is attributed to the formation of 4-aminophenol [23,36,39,41], thus confirming that the nitroaromatic compound is reduced to its corresponding arylamine. Control experiments confirmed that no reduction takes place in the presence of $NaBH_4$ or carbon microspheres alone, only when Ag/CM composite particles were used in suspension. These results indicate that the reduction is due to the catalytic activity of supported Ag NPs and that the Ag NPs surface is accessible to species in solution. As $NaBH_4$ is in excess with respect to 4-nitrophenol then its can be assumed that it has a constant concentration and the reaction rate becomes pseudo-first-order with respect to the 4 - nitrophenol [36,43,44].

$$\frac{dc_t}{dt} = -k_{app} c_t \qquad \text{(eqn 4.7)}$$

Since the absorbance at 400 nm is proportional to the concentration of 4-nitrophenol in solution then eqn 4.8 can be used to determine the rate of reduction in solution.

$$\frac{A_t}{A_0} = \frac{C_t}{C_0} \qquad \text{(eqn 4.8)}$$

Figure 4.9 shows a logarithmic plot of A_t/A_0 where A_t and A_0 are the absorbances at 400 nm at time t and zero, respectively. An apparent rate coefficient k_{app} was calculated near time zero from linear fits of curves such as the one in Figure 10 yielding k_{app} = 0.0015 ± 0.0002 s^{-1}. After normalization of k_{app} by the molar concentration of silver in our suspensions (1.2 X 10^{-5} M), we obtain a specific rate coefficient k = 122 ± 16 s^{-1} M^{-1}, which is within the range of values observed for polymer-stabilized Ag nanoparticles (~ 25 nm) obtained at similar NaBH4 concentrations [45], albeit much lower than values originally reported by Pradhan et al. for bare Ag nanoparticles [39].

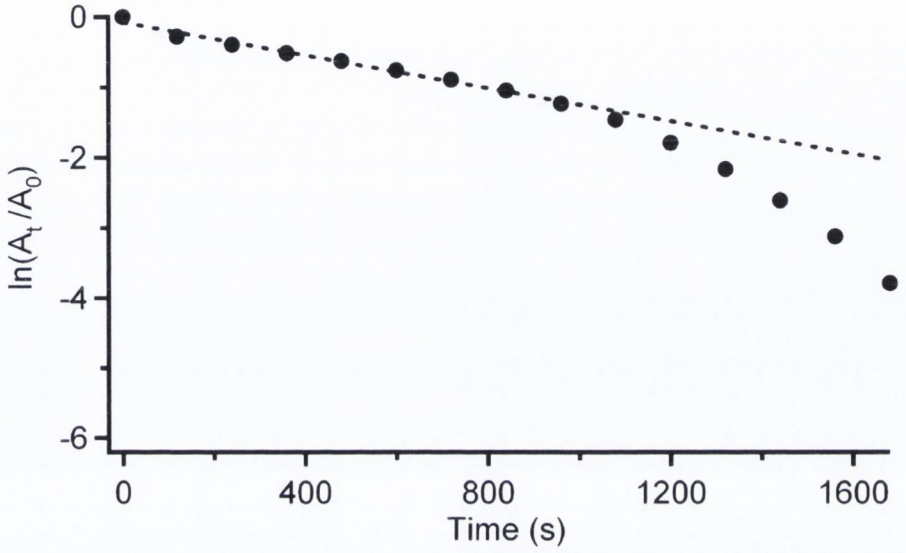

Figure 4.9: Logarithmic plot of the normalized absorbance change as a function of time. The linear fit near time zero was used to calculate the rate coefficient for the reduction reaction.

This suggests that, although we cannot exclude the presence of a partially blocking adsorbed layer, metallic surface sites at the carbon-supported Ag aggregates are highly available to catalyse heterogeneous reactions.

4.3.2.2 Suzuki coupling using Pd/CM composites.

Suzuki reaction experiments in order to determine the catalytic activity of the Pd/C were carried out at Albion College (USA) by Lyndsay Taylor and Dr. Kevin Metz.

Pd/C particles were tested as catalysts using the Suzuki coupling reaction of phenylboronic acid with bromotoluene. Specifically, we explored the coupling reaction between phenylboronic acid and bromotoluene, which yields methylbiphenyl as displayed in Figure 4.10. This reaction, performed in triplicate, resulted in a 40 ± 10% yield of the desired product.

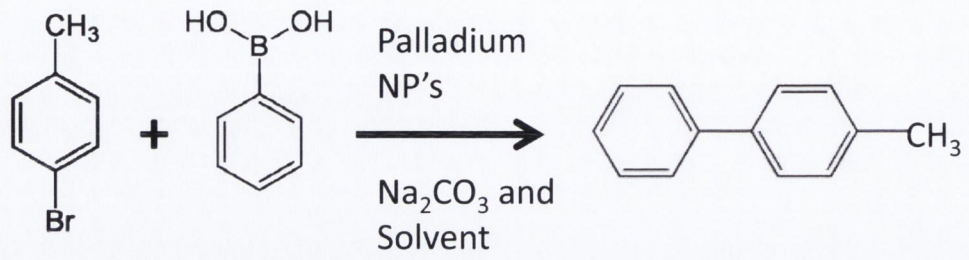

Figure 4.10: Suzuki reaction between 4-bromotoluene and phenylboronic acid, run for 18 h at room temperature. Yields of 40 ± 10% were achieved, even upon the third use of the Pd/CM catalysts.

Furthermore, the same Pd/CM particles used three times sequentially displayed no loss in catalytic activity. Control experiments using bare carbon microspheres yielded no product. Our results are consistent with the range of previously reported catalytic activities for supported palladium nanoparticles utilized for the Suzuki reaction. For example, Kantam et al. reported yields between 10% and 90% for the coupling reaction illustrated in Figure 4.10 (room temperature, varied solvents, 12 h) catalysed by nanopalladium on a layered double hydroxide support (LDH-Pd0) [46]. Yields in Suzuki reactions are known to be sensitive to the combination of solvents and base used [46], and also depend on the reaction temperature and type of aryl-halide used [37]. Therefore, differences between our yields and reported yields can be the result of variations in reaction conditions, the presence of adsorbed molecules at the Pd surface, or a combination of these two factors. In summary, these results suggest that our composite system displays a performance comparable to that of previously reported supported Pd nanoparticle systems.

4.3.3 Discussion and summary

Silver and Palladium nanoparticle were successfully grown on CM surfaces via heterogeneous reduction using green electroless deposition. Competing homogeneous reduction occurs simultaneously leading to unsupported NPs. Crucial to the catalytic studies in this report it was possible to remove unsupported NPs via centrifugation as demonstrated in Figure 4.11. However, this does lead to concern about the current efficiency of synthesizing NP/Composites using this particular approach but results are promising for first time green electroless deposition.

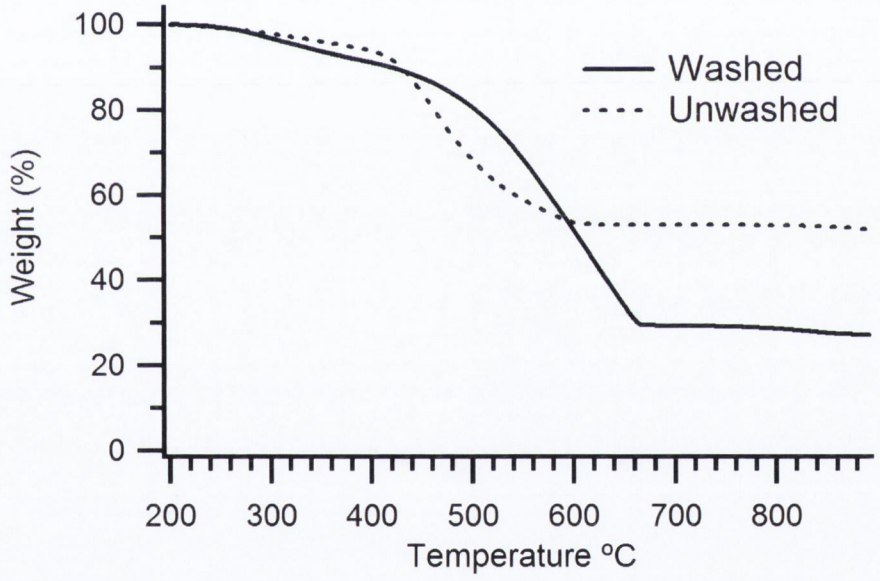

Figure 4.11: TGA curves for washed and unwashed Ag/C, Difference can be attributed to unsupported particles.

The sensitisation step was found to influence the extent of catalytic seed nucleation on the CM surface. Metallic ion concentration in solution was found to influence the cluster size and dispersion of particles for both metal composites. Particle size was found to be limited by some parameter other than those above. The crystalline and metallic nature of the particles located at the carbon surface was confirmed via XRD.

The loadings due to heterogeneous catalysis were calculated to be (13.5 ± 1.5)% and (7.4 ± 1.0)% w/w, for the Ag/C and Pd/C materials respectively. Both composites were shown to be catalytically active. In this section, we discuss these results, implications and suggest some further experiments that may need to be performed to confirm assertions.

4.3.3.1 Effect of Sensitisation step on composites

Firstly, it was determined that sensitisation step is vital for surface immobilisation of the metal nanoparticles formed at carbon microspheres. Also, initial increases in surface modification and catalytic seed nucleation due to increased Sn^{2+} concentration, indicates increased adsorbed Sn^{2+} at the carbon surface, allows adsorption of more Pd^{2+} species at the surface during activation. However, subsequent concentration increases caused only minor modifications, indicate that there may be a limit to Sn and Pd adsorption at the carbon surface. This would suggest that there are a limited number of sites on the CM surface to which Sn^{2+} can complex. These results are consistent with experiments performed by Khoperia et el at glass surfaces for similar sensitisation and activation protocols [47]. Performing TGA on carbon samples after sensitisation/activation for the various Sn^{2+} concentrations would quantitatively confirm all of the above qualitative statements. Increased palladium absorption via activation led to an increase in the number of particles and particle clusters that were synthesised at the CM surface via ED. TGA would again, be a facile method for quantifying this qualitative observation.

For both Ag and Pd composites, it was observed that metallic ion concentration had an effect on the dispersion of particles and particle clusters at the CM surface. Increased concentration was linked with an increase in the number and size of particle clusters. However, no particle size increase was observed. This can be explained by capping of the metal particles with oxidized polyphenols/caffeine hypothesized by Moulton et al

[6]. Capping of the particles could limit transport to the surface inhibiting further catalytic reduction from happening at the surface. TGA results shown in figure 4.7 support this hypothesis via significant combustion of organic mass in the 285-340 °C regions. TGA results for Pd activated CMs have significantly less mass loss in this region than the Pd/C composite, indicating organic compounds from the coffee are responsible. SERS experiments carried out by the Colavita group on the Ag/C support this hypothesis (data not shown). However, it cannot be confirmed if the organic materials are in the form of a capping agent on the metallic surface, adsorbed onto the highly porous carbon scaffold or both. Further control, TGA experiments with coffee, pristine carbon and activation carbon could offer more insight into which surfaces the organic materials are adsorbed onto, offering insight into whether organic capping agents are responsible for particle size limits.

4.3.3.2 Characterisation of composites, loadings and homogeneous catalysis

XRD data supports the presence of metallic silver and palladium in the composite material, Wen et al and other research groups demonstrated the effectiveness of XRD for characterising Silver nanostructures [21,22]. Furthermore, EDS mappings shown in figure 4.12, match highest Ag concentrations to particles observed via SEM on the CM surface. This suggests that particles observed on the CM surface are directly responsible for peaks observed via XRD. EDS mappings also indicated Pd presence but sample instability and drift didn't allow determination of a location for highest Pd concentration.

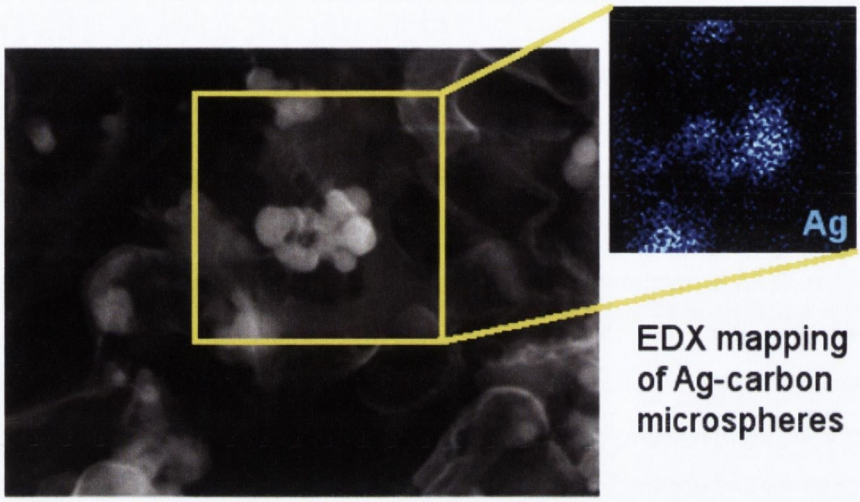

Figure 4.12: EDX mapping placing highest concentrations of Ag to locations where particles are observed at the CM surface

However, XRD further supports that nanoparticles are responsible for the observed peaks due to peak broadening for both samples. Three main factors contribute to peak broadening in diffraction experiments: defects, strain between grains and crystallite size. Under the assumption that crystallite size is the dominant broadening mechanism, the Scherrer equation can be used to estimate crystallite size as shown in equation 4.9:

$$\tau = \frac{K\lambda}{\beta Cos\theta} \qquad \text{(eqn 4.9)}$$

Where K is the Scherrer constant (0.87-1), λ is the X-ray wavelength, β is the line broadening at full width half maximum (FWHM) in radians, θ is the Bragg angle and τ is the average dimension of the ordered crystallite domain. Using the (111) peaks from figures 4.6a - b we obtain crystalline sizes of 31nm and 17nm for the Ag/C and Pd/C composites respectively. As particle size is limited to approx 30 nm, crystalline sizes indicates that metallic particles on the composite material are highly crystalline. Eqn 4.9 indicates increased broadening would correspond to decreasing crystallite size. As

obtained crystallite sizes are near to particle size limits, this indicates broadening here is mostly from contributions in the crystallite domain size.

Under current reaction conditions, the estimated Ag/C and Pd/C mass ratios are (13.5 ± 1.5)% and (7.4 ± 1.0)% w/w. Showing TGA/EDS as a quick and effective method for obtain loading for particles nucleated on carbon supports via ED. However the results in section 4.3.1.1 above would suggest that it would be possible to increase or decrease metallic loadings obtained on the carbon support. These results also indicate that there is a potential limit to particle loadings due to limits on the absorbance of Sn at the carbon surface and subsequent capping of particle growth. TGA/EDS experiments coupled with rigorous numbers of composites produced from varying reaction conditions would confirm this. These experiments would indicate over what range the loadings can be strictly controlled and what the maximum potential particle loading would be for both composites materials.

Kinetic experiments confirmed that both composite materials are catalytically active. However, Ag/CM kinetic results yielded a k_{app} which was less than unsupported Ag-NPs of similar size synthesis by Pal et el [39]. This difference can be explained by two possible mechanisms.

i)

The apparent rate constant k_{app} is found to be proportional to the total surface area S available in the metal nanoparticles [48-50]. Using this, eqn 4.7 can be expanded to eqn 4.10.

$$\frac{dc_t}{dt} = -k_{app}c_t = -k_1 S c_t \qquad \text{(eqn 4.10)}$$

Where S is the total surface area normalised to volume of metallic particles. For Ag/CM, metallic particles were observed in the form of NP clusters. NP aggregation is known to inhibit reaction rates for surface reaction due to the loss of accessible surface area for the same unit volume when comparing to discrete particles. This

hypothesis could be checked by performing catalytic experiments at various silver loadings. It was observed that as loadings increase, the size and number of particle cluster increase. However, as particle size is capped, the ratio of particle volume to theoretical surface area should remain relatively constant. Hence, linear relationships with normalised surface area and rate constant K observed by other researchers would be expected if the total surface area was accessible [50]. If the normalised rate constant decreased with increasing metal loadings, it would suggest increased clustering, confirming the hypothesis.

ii)

The second mechanism is a reduced rate of electron transfer. Electron transfer occurs at the metallic surface, Borohydride ions react with the surface of the nanoparticles and transfer a surface hydrogen species [51,52]. Simultaneously, 4 - Nitrophenol molecules are adsorbed on the surface of the nanoparticles and undergo reduction by the surface hydrogen species. The rate of electron transfer at the metal surface can be influenced by two steps: (a) diffusion of 4-nitrophenol to the metal surfaces and diffusion of 4-aminophenol away from the surface and (b) interfacial electron transfer. In general, this means the rate constant K_{app} can be split into two terms as shown in eqn 4.11[41].

$$k_{app}^{-1} = k_{surf}^{-1} + k_{diff}^{-1} c^{-1} \qquad \text{(en 4.11)}$$

It has been demonstrated that the use of stabilising agents, surfactants and supports can influence the kinetics of catalysis [36,45,53]. It has been proposed that these differences are linked to part (b) of the above eqn. Therefore, the presence of any capping layer or surface molecules would lower k_{app} for the composites. This kinetic data coupled with the TGA demonstrating the presence of organic materials, adds weight to the hypothesis by Varma et al that oxidized polyphenols/caffeine cap nanoparticle growth [6].

However, many researchers have reported an induction time to catalysis, attributed to diffusion-controlled adsorption of species onto the metallic surface [54-56]. In our experiments no induction time was observed for the methods used indicating accessible catalytic surfaces. Signori et al suggest that diffusion of the BH_4^- to the surface to create the surface hydrogen species, is the initiation step. In our experiments, the Ag/C was placed in the Borohydride, followed by addition of the 4 – NP, allowing the Borohydride to initiate on the surface whilst the 4-np injection was being prepared. Repeating our experiments, with the addition of Borohydride as the last step could give insight into Signori's hypothesis if a t_0 time is observed for this experiment.

It is possible that borohydride reduces oxidized polyphenols, removing the organic capping layer, allowing reaction without a t_0. As Borohydride has a greater reduction potential than caffeic acid, chlorogenic acid, Caffeine and hydroquinone at all pH values, this could indicate why catalytic activity was hindered in ED process limiting particle size but metal surface is readily available for catalysis. Immersing the composite in borohydride, followed by washings would open up the metallic surfaces to reaction. Further experiments by re-immersion in a metal solution, followed by coffee would confirm the above theory. If particles on the CM increase in size, borohydride has interacted with some surface layer. If they remain the same it disproves the theory showing borohydride doesn't remove any capping layer.

4.4 Conclusions

We have synthesized Ag/CM and Pd/CM composite particles using porous carbon microparticles as scaffolds for electroless deposition and decaffeinated coffee as a reducing agent. Our methodology shows that this mild and environmentally benign reductant can be used for the synthesis of surface supported metal nanoparticles, thus expanding its use beyond solution based nanoparticle synthesis [5,6]. We also confirmed the viability of CM synthesized via USP for use as a support material. To our knowledge, this is the first time sensitisation, activation and electroless deposition protocols have been performed on such CMs. We confirmed the suitable of these materials for catalytic seed nucleate and subsequent ED protocols which could have implications beyond the ED chemistries used in this report.

Both Ag/C and Pd/C composite microspheres were tested in order to assess their activity as heterogeneous catalysts for organic synthesis. We found that in both cases suspensions of our composite microparticles displayed the characteristic chemistry of metallic silver and palladium nanoparticles thus indicating that, after deposition at the carbon scaffold, metallic particles offer available reactive surface sites. The reaction rates observed for Suzuki coupling and nitroaromatic reduction reactions, based on calculated metal loadings, suggest that metal/CM composites reported in this work offer excellent performance compared to similar Ag and Pd supported nanoparticle systems.

References

(1) Astruc, D.; Lu, F.; Aranzaes, J. R. *Angewandte Chemie International Edition* **2005**, *44*, 7852.

(2) Metz, K. M.; Tse, K. Y.; Baker, S. E.; Landis, E. C.; Hamers, R. J. *Chemistry of Materials* **2006**, *18*, 5398.

(3) Zhang, P.; Shao, C.; Zhang, Z.; Zhang, M.; Mu, J.; Guo, Z.; Liu, Y. *Nanoscale* **2011**, *3*, 3357.

(4) Metz, K. M.; Colavita, P. E.; Tse, K.-Y.; Hamers, R. J. *Journal of Power Sources* **2012**, *198*, 393.

(5) Nadagouda, M. N.; Varma, R. S. *Green Chemistry* **2008**, *10*, 859.

(6) Moulton, M. C.; Braydich-Stolle, L. K.; Nadagouda, M. N.; Kunzelman, S.; Hussain, S. M.; Varma, R. S. *Nanoscale* **2010**, *2*, 763.

(7) Sivaraman, S. K.; Elango, I.; Kumar, S.; Santhanam, V. *Current science* **2009**, *97*, 1055.

(8) Markovic, J. D.; Ignjatovic, L. M.; Markovic, D. A.; Baranac, J. M. *Journal of Electroanalytical Chemistry* **2003**, *553*, 169.

(9) Gentry, S. T.; Fredericks, S. J.; Krchnavek, R. *Langmuir* **2009**, *25*, 2613.

(10) G. Debry *Composition of coffee, in: Coffee and Health, John Libbey Eurotext, Paris,* , 1994.

(11) Duffy, P.; Magno, L. M.; Yadav, R. B.; Roberts, S. K.; Ward, A. D.; Botchway, S. W.; Colavita, P. E.; Quinn, S. J. *Journal of Materials Chemistry* **2012**, *22*, 432.

(12) Skrabalak, S. E.; Suslick, K. S. *Journal of the American Chemical Society* **2006**, *128*, 12642.

(13) Zhou, W.-J.; Wang, K.-H.; Wang, J.-X.; Gao, Z.-R. *Tetrahedron* **2010**, *66*, 7633.

(14) Ritchie, N. W. *Scanning* **2012**.

(15) Mallory, G. O.; Haydu, J. B. *American Electroplaters and Surface Finishers Society, Orlando, FL* **1990**.

(16) Goia, D. *New Journal of Chemistry* **1998**, *22*, 1203.

(17) Lide, D. R. *CRC Handbook of Physical Constants*; CRC Press, 1998.

(18) Menon, V. P.; Martin, C. R. *Analytical Chemistry* **1995**, *67*, 1920.

(19) Kim, J. Y.; Byk, T. V.; Cho, S. H.; Noh, C.-H.; Song, K. Y.; Kim, J. M.; Gaevskaya, T. *Electrochemical and solid-state letters* **2006**, *9*, H118.

(20) Yu, S.; Welp, U.; Hua, L. Z.; Rydh, A.; Kwok, W. K.; Wang, H. H. *Chemistry of Materials* **2005**, *17*, 3445.

(21) Lu, L.; Kobayashi, A.; Kikkawa, Y.; Tawa, K.; Ozaki, Y. *The Journal of Physical Chemistry B* **2006**, *110*, 23234.

(22) Wen, X.; Xie, Y.-T.; Mak, W. C.; Cheung, K. Y.; Li, X.-Y.; Renneberg, R.; Yang, S. *Langmuir* **2006**, *22*, 4836.

(23) Rashid, M. H.; Mandal, T. K. *The Journal of Physical Chemistry C* **2007**, *111*, 16750.

(24) Shter, G.; Shindler, Y.; Matatov-Meytal, Y.; Grader, G.; Sheintuch, M. *Carbon* **2002**, *40*, 2547.

(25) Charbonnier, M.; Alami, M.; Romand, M. *Journal of applied electrochemistry* **1998**, *28*, 449.

(26) Patel, P.; Kim, I.-S.; Maranchi, J.; Kumta, P. *Journal of Power Sources* **2004**, *135*, 273.

(27) Song, P.; Wen, D. *The Journal of Physical Chemistry C* **2009**, *113*, 13470.

(28) Fergus, J. W.; Mallipedi, C. V.; Edwards, D. L. *Composites Part B: Engineering* **1998**, *29*, 51.

(29) Chang, G.; Zheng, X.; Chen, R.; Chen, X.; Chen, L.; Chen, Z. *Acta Physico-Chimica Sinica* **2008**, *24*, 1790.

(30) Zhang, H.; Gromek, J.; Fernando, G. W.; Marcus, H. L.; Boorse, S. *Journal of phase equilibria* **2002**, *23*, 246.

(31) Ang, L.; Hor, T. A.; Xu, G.; Tung, C.; Zhao, S.; Wang, J. *Carbon* **2000**, *38*, 363.

(32) Yuan, W.; Jiang, G.; Che, J.; Qi, X.; Xu, R.; Chang, M. W.; Chen, Y.; Lim, S. Y.; Dai, J.; Chan-Park, M. B. *The Journal of Physical Chemistry C* **2008**, *112*, 18754.

(33) Chi, Y.; Zhao, L.; Yuan, Q.; Yan, X.; Li, Y.; Li, N.; Li, X. *Journal of Materials Chemistry* **2012**, *22*, 13571.

(34) Gao, C.; Li, W.; Jin, Y. Z.; Kong, H. *Nanotechnology* **2006**, *17*, 2882.

(35) Ghosh, S. K.; Mandal, M.; Kundu, S.; Nath, S.; Pal, T. *Applied Catalysis A: General* **2004**, *268*, 61.

(36) Esumi, K.; Isono, R.; Yoshimura, T. *Langmuir* **2004**, *20*, 237.

(37) Miyaura, N.; Suzuki, A. *Chemical Reviews* **1995**, *95*, 2457.

(38) Karousis, N.; Tsotsou, G.-E.; Evangelista, F.; Rudolf, P.; Ragoussis, N.; Tagmatarchis, N. *The Journal of Physical Chemistry C* **2008**, *112*, 13463.

(39) Pradhan, N.; Pal, A.; Pal, T. *Langmuir* **2001**, *17*, 1800.

(40) Murugadoss, A.; Chattopadhyay, A. *Nanotechnology* **2008**, *19*, 015603.

(41) Herves, P.; Pérez-Lorenzo, M.; Liz-Marzán, L. M.; Dzubiella, J.; Lu, Y.; Ballauff, M. *Chemical Society Reviews* **2012**, *41*, 5577.

(42) Sassaroli, A.; Fantini, S. *Physics in Medicine and Biology* **2004**, *49*, N255.

(43) Tang, S.; Vongehr, S.; Meng, X. *Journal of Materials Chemistry* **2010**, *20*, 5436.

(44) Wunder, S.; Polzer, F.; Lu, Y.; Mei, Y.; Ballauff, M. *The Journal of Physical Chemistry C* **2010**, *114*, 8814.

(45) Signori, A. M.; Santos, K. d. O.; Eising, R.; Albuquerque, B. L.; Giacomelli, F. C.; Domingos, J. B. *Langmuir* **2010**, *26*, 17772.

(46) Kantam, M. L.; Subhas, M.; Roy, S.; Roy, M. *Synlett* **2006**, *2006*, 0633.

(47) Khoperia, T.; Tabatadze, T.; Zedgenidze, T. *Electrochimica Acta* **1997**, *42*, 3049.

(48) Mei, Y.; Sharma, G.; Lu, Y.; Ballauff, M.; Drechsler, M.; Irrgang, T.; Kempe, R. *Langmuir* **2005**, *21*, 12229.

(49) Mei, Y.; Lu, Y.; Polzer, F.; Ballauff, M.; Drechsler, M. *Chemistry of Materials* **2007**, *19*, 1062.

(50) Panigrahi, S.; Basu, S.; Praharaj, S.; Pande, S.; Jana, S.; Pal, A.; Ghosh, S. K.; Pal, T. *The Journal of Physical Chemistry C* **2007**, *111*, 4596.

(51) Liu, B.; Li, Z. *Journal of Power Sources* **2009**, *187*, 527.

(52) Guella, G.; Patton, B.; Miotello, A. *The Journal of Physical Chemistry C* **2007**, *111*, 18744.

(53) Jana, N. R.; Sau, T. K.; Pal, T. *The Journal of Physical Chemistry B* **1999**, *103*, 115.

(54) Zeng, J.; Zhang, Q.; Chen, J.; Xia, Y. *Nano Letters* **2009**, *10*, 30.

(55) Kuroda, K.; Ishida, T.; Haruta, M. *Journal of Molecular Catalysis A: Chemical* **2009**, *298*, 7.

(56) Sarkar, S.; Sinha, A. K.; Pradhan, M.; Basu, M.; Negishi, Y.; Pal, T. *The Journal of Physical Chemistry C* **2010**, *115*, 1659.

Chapter 5

Synthesis of Fe/Fe_xO_y nanoparticles on porous carbon microspheres: Structure and surface reactivity

Composite materials are of interest because they can potentially combine the properties of their respective components in a manner that is useful for specific applications. Here, we report on the use of Sodium hypophosphite and Dimethylamine borane as reductants for formation of supported metal nanoparticles. This chapter describes the characterisation of these composites using various techniques, followed by experimental results that show potential applications of the composite materials synthesized.

5.1 Introduction

There has been great interest in synthetic methods that yield supported iron and iron oxide nanoparticles in order to prevent aggregation and improve their transport properties, handling and surface reactivity (See Section 1.3.2 for more detail). Other research groups have supported unmodified nanoparticles on solid materials, such as clays [1], carbon [2-4] and silica particles [5], so that they can be readily handled/delivered while preserving their surface chemistry.

In this chapter we report on the use of two electroless deposition (ED) methods for the synthesis of carbon-supported iron/iron oxide (Fe/Fe_xO_y) nanoparticles. We have used carbon porous microspheres synthesized via ultraspray pyrolysis as carbon scaffolds for the nucleation and growth of iron nanoparticles (See Chapter 3). The best ED method was determined via Scanning Electron Microscopy (SEM). Subsequently, we characterized the structure, morphology and composition of Fe/Fe_xO_y composite microspheres using a combination of Scanning Electron Microscopy (SEM), thermogravimetric analysis (TGA), X-ray diffraction (XRD) and X-ray absorption spectroscopies (EXAFS and XANES). The ED approach resulted in a composite Fe/Fe_xO_y/carbon microsphere of narrowly dispersed size and little to no unsupported iron NPs. Finally, we show that these Fe/Fe_xO_y/CM composite particles display surface reactivity towards the remediation of Cr(VI), a toxic pollutant, suggesting that these are promising materials for the removal of water pollutants from aqueous solution.

5.1.1 Electroless deposition of Iron

ED procedures for the depositions of iron and iron alloy based films have received relatively little attention in the scientific literature when compared to metals such as

Cu, Ni and Au. Most researchers have attributed this lack of attention to iron based films to the difficulty of ED Fe deposition when compared to other metals. The cause of this difficulty has been attributed to many factors. Fujita et al indicated that the challenges may stem from the low catalytic activity of Fe, hindering the autocatalysis needed for successful ED [6]. Other researchers have indicated that low stability due to oxidation in air may be another reason for ED researchers avoiding Fe in favour of other depositions [7]. Finally, the reduction potential of Fe^{2+} is low and therefore it is hard to balance thermodynamic instability with kinetic stability in the plating bath. In this chapter we utilise two methods based on Fe ED baths by Drovosekov et al [7] and Nakanishi et al [8], hereby denoted as method A and method B respectively, as summarised in table 5.1.

Component	Method A	Method B
Metal Species	Fe^{2+}	Fe^{3+}
Reducing agent	Sodium Hypophosphite	DMAB
Chelating agent	Glycine	None
Buffering agent	NH_4Cl	None
Temperature	90 °C	80°C
pH	10.5	8

Table 5.1: Demonstrating the components of Methods A and B

These methods are vastly different, containing differing metal ion sources and reducing agents. Method A utilises Fe^{2+} whereas method B utilised Fe^{3+}. Both metals have differing reduction potentials and will perform differently. Method A uses Sodium Hypophosphite whereas method b uses DMAB. However, both are different and could lead to differing Iron based deposits. The next largest difference is that Method A utilises Glycine as a chelating agent whereas method B does not use one at all. Glycine complexes with Fe ions as described in eqn 5.1 [9].

$$Fe(H_2O)_6^{m+} + nGly \longleftrightarrow Fe(H_2O)_{6-n}(gly)_n^{m+} \qquad \text{eqn 5.1}$$

Where n = 1, 2, 3 and m = 2, 3. Complexation with Glycine stabilises solutions of Fe ions by competing with the complexation of OH^- ions, inhibiting precipitation of colloidal iron oxides and subsequent decomposition of solution. This indicates that use of a chelating agent such as Glycine is essential at higher pH ranges when using Fe ions in an ED bath. The next difference in baths is that Method A utilises ammonia solution to adjust the bath pH to 10.5. Therefore, in method A, NH_4Cl is utilised as a buffer agent as the NH_4^+ ammonium ion will be present as the conjugate acid as shown in eqn 5.2.

$$NH_3 + H_2O \leftrightarrow OH^- + NH_4^+ \qquad \text{eqn 5.2}$$

These differences will be discussed later in section 5.4 when the performance of the two methods in synthesising Fe/Fe_xO_y nanoparticles on porous CMs will be evaluated.

5.2 Experimental

5.2.1 Materials and reagents

Reagent grade tin chloride dihydrate (96%; Fisher), palladium chloride (Fisher), sodium hydroxide (97%, Sigma), dichloroacetic acid (DCA, 99%, Sigma Aldrich), sulphuric acid (95%), hydrogen peroxide (30%, Sigma), sodium hypophosphite (97%, Sigma), ammonium chloride (99%, Sigma), Glycine (97%, Sigma), ammonium hydroxide solution (30%, fluka), iron (II) sulphate (97%, sigma), dimethylamine borane complex (DMAB, 97%, Sigma), trifluoroacetic acid (TFA, 99%, Sigma), iron(III) sulphate hydrate (97%, Sigma), sodium dichromate dihydrate (99.5%, Sigma).

Amorphous carbon samples used for XPS and X-ray diffraction studies were prepared via magnetron sputtering deposition techniques, as previously described by Cullen et al [10]. Amorphous carbon thin films were subsequently immersed in piranha solution

(3 : 1, H_2SO_4 to H_2O_2) in order to increase the number of carboxylic acid moieties at their surface

5.2.2 Composite material synthesis

Activated Carbon microsphere (CMs) synthesis: CMs were synthesized using ultrasonic spray pyrolysis as previously reported in section 3.2.2 [11,12]. CMs were generated from a 1.5 M solution of NaDCA. A solution of 0.050 M $SnCl_2$ in 0.070 M trifluoroacetic acid was prepared and CMs were added to a final concentration of 0.2400 g L^{-1} and sonicated to obtain a uniform dispersion. CMs were left in the solution for approximately 30 min, subsequently filtered through 0.45 mM nylon membranes and washed with water and ethanol. CMs were then dispersed via sonication in a 5.6 X 10^{-3} M solution of $PdCl_2$ acidified to pH 1 via addition of HCl. After 30 min in this solution CMs were washed via multiple cycles of centrifugation and gentle stirring in Millipore water.

ED using Method A: Water was heated up to 90 °C in a reflux apparatus prior to adding iron (II) sulphate to a concentration of 0.050 M, followed by addition of Glycine to a concentration of 0.20 M and subsequent addition of ammonium chloride to a concentration of 2.0 M. Freshly sensitized and activated CMs were then added to the hot solution to a concentration of approximately 0.1200 g L^{-1}, to which sodium hypophosphite was added to a final concentration of 0.10 M. The CM dispersion was left at 90 °C for 1.5 h under reflux, constant stirring and under an Ar flow. Aliquots were withdrawn at various time intervals and placed drop cast on silicon wafers for SEM measurements.

ED utilising Method B: Water was heated up to 80 °C in a reflux apparatus prior to adding iron (III) sulphate to a concentration of 4.4 X 10^{-4} M; a typical batch size in our experiments was 50 mL. Freshly sensitized and activated CMs were then added to the

hot solution to a concentration of approximately 0.1200 g L^{-1}, to which DMAB was added to a final concentration of 0.070 M. The CM dispersion was left at 80 °C for 1.5 h under reflux, constant stirring and under an Ar flow. The iron-modified CMs filtered and washed with abundant degassed water and ethanol prior to drying and further characterization; samples were kept under an Ar flow at all times during filtering, washing and drying.

5.2.3 Characterization

Scanning Electron Microscopy (SEM): was performed at an accelerating voltage of 10 keV using a Zeiss Ultra microscope equipped with an Energy Dispersive X-ray Spectroscopy (EDS) detector (Oxford Instruments INCA system with silicon drift detector (SDD)). Samples were prepared by drop casting on Si wafers from dispersions of the composite powder. Elemental analysis was performed using the EDS detector with an accelerating voltage of 20 KeV. ***X-ray photoelectron spectroscopy (XPS):*** was performed under ultrahigh vacuum on an Omicron system with base pressure 1 x 10^{-10} bar, equipped with a monochromatized Al Kα source and a multichannel detector. ***X-ray diffraction (XRD):*** was carried out on a Siemens D500 diffractometer with monochromated Cu Kα radiation; pattern analysis was carried out using commercial XRD software (EVA, Bruker). Samples were prepared by supporting Metal/CM composites on nylon membranes. ***Thermal Gravimetric Analysis (TGA):*** measurements were performed using a Perkin-Elmer Pyris 1 TGA, using air as a carrier gas and a heat ramp of 10 °C min^{-1} from 25 °C to 900 °C including two 5 min long isothermal steps at 100 °C and 200 °C. ***Brunauer–Emmett–Teller (BET):*** analysis was performed using a Quantachrome Nova Station using a multi-point BET plot [13]. The sample was pretreated at 30 °C under vacuum for 24 h prior to analysis using N_2 as the adsorbing gas. ***UV-Vis:*** spectra of chromate anions were obtained on a Shimadzu UV-2401PC. Measurements were taken at a rate of 120nm per second at 0.2nm intervals and a slit width of 1nm. ***Extended X-ray Absorption Fine Structure (EXAFS):*** spectra were

collected at the SAMBA beamline at SOLEIL synchrotron [14]. The beamline was operated with a Si (220) double-crystal sagittal focusing monochromator. A pellet of pure Fe/CM powder was measured in transmission at the Fe K-edge; the pellet was checked for homogeneity with X-rays to estimate possible thickness errors. Data were analyzed using Horae [15] and FEFF8.4 [16]. FEFF theoretical standards were tested versus experimental Fe_2O_3 and bcc-Fe standards. Maghemite, hematite and magnetite XANES standards were recorded on BM30 (ESRF) and calibrated on a Fe foil and a hematite standard to match spectra recorded on SAMBA (SOLEIL). ***Cr(VI) removal studies:*** A 12.9 mg L^{-1} Cr(VI) solution was degassed via ultrasonic treatment. Freshly prepared Fe/CM particles were added to 20 mL of this Cr(VI) solution, in order to achieve a final composite concentration of 0.165 g L^{-1}. The suspension was then kept under an argon atmosphere with constant stirring for the duration of our studies; the solution remained at neutral pH over the course of adsorption reactions. Aliquot samples were withdrawn at various time intervals. Subsequent quenching of the reaction was performed via filtration of the solution through 0.45 μM nylon membrane filters. The Cr(VI) concentration was measured via UV-Vis spectroscopy by monitoring the absorbance at 339 nm, according to a method developed by McCreery and co-workers [17]. Control adsorption experiments were carried out using 0.070 g L^{-1} suspensions of pristine carbon microspheres; this concentration was found to yield an equivalent particle number density to that used in Fe/CM adsorption experiments, as determined via TGA.

5.3 Results and discussion

The results section will consist of three parts. Part (i) Reports results on the characterisation of the sensitisation and activation steps; Part (ii) Shows results of experiments using method A; Part (iii) Shows results of experiments using method B. Subsequent characterisation and adsorption experiments for Fe/Fe_xO_y composite

materials will be shown. These sections will be followed by a discussion of the results, with suggestions for supplemental and follow-up experiments.

5.3.1 Characterisation of activation steps

In order to obtain iron nanoparticles supported on carbon microspheres, CMs underwent a two-step process of sensitization and activation prior to iron reduction at their surface via an electroless process. The proposed mechanism for the sensitization and activation steps are discussed in detail in section 4.3.1 [18]. Briefly, an exchange of Sn^{2+} ions at the carbon surface occurs, thanks to the presence of charged oxidized groups, such as carboxylates. Second, a reduction of Pd^{2+} to Pd^{0} that takes place at the adsorbed Sn^{2+} sites, leading to the formation of small metallic Pd particles. These Pd^{0} sites then serve as catalytic centers for the electroless deposition of metals.

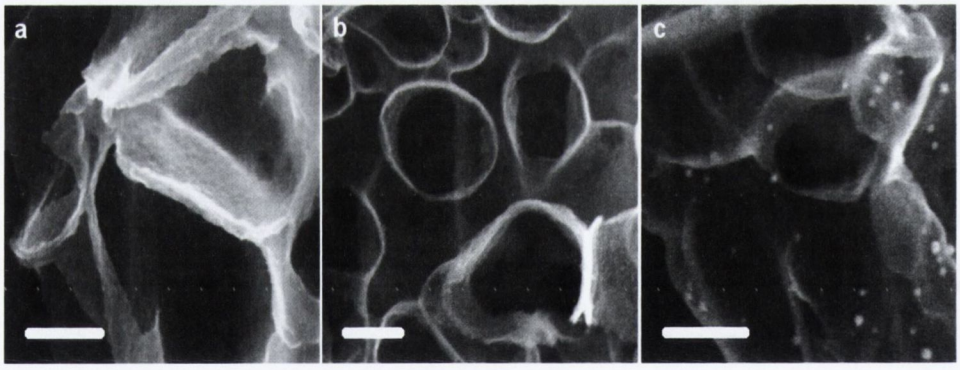

Figure 5.1: SEM images of the surface of carbon microspheres as prepared (a), after sensitization in a Sn^{2+} solution (b), and after activation in a Pd^{2+} solution (c); scale bar =200 nm. After activation it is possible to observe the formation of small clusters decorating the surface of the carbon scaffold.

Figure 5.1a–c show the modifications observed at the surface of CMs after each of these steps for the concentrations of $SnCl_2$ and $PdCl_2$ utilised. After sensitization with Sn^{2+} we observe no morphological changes at the carbon surface, as shown by

comparing the bare carbon surface in Figure 5.1a with the image after sensitization in Figure 5.1b. After the activation by immersion in the Pd^{2+} solution, formation of small clusters <5 nm in size is observed, as illustrated in Figure 5.1c. These results are also consistent with the hypothesis proposed in section 4.3.3, where it was observed that less dense clusters of nucleation sites form for lower $SnCl_2$ concentration and less nucleated sites due to lower $PdCl_2$ concentration. Obtaining small particles like those observed in figure 5.1c is consistent with the works of Kind et al for similar palladium systems where 5 nm islands of Pd metal where observed to form on aminothiolate layer on an Au(111) surface utilising ED [19].

Chemical changes taking place during the sensitization/activation steps at the surface, were investigated via XPS measurements. Figure 5.2 shows an XPS spectrum obtained on a graphitic amorphous carbon surface after the same sensitisation/ activation steps described above. The spectrum shows the characteristic C 1s peak arising from the underlying carbon film at 284.5 eV [10]. The 3d doublet of Pd is visible at 340.5 and 335.5 eV, confirming the presence of metallic Pd at the carbon surface, probably with small amounts of adsorbed oxygen [18,20,21]. The Pd 3p doublet is also visible at 532/560 eV, but it overlaps with the O 1s peak at approximately the same binding energy [22]. The spectrum also shows a doublet at 486.5/495.0 eV that we assign to Sn 3d arising from oxidized tin species [23,24]. Our results are consistent with previous XPS studies of the two-step sensitization/activation process on insulating materials, that show that oxidized tin species remain at the surface together with metallic Pd [18]. XPS data in Figure 5.2 together with SEM characterization shown in Figure 5.1 therefore suggest that a two-step sensitization/activation process on CMs leads to the formation of Pd^0 catalytic seeds at carbon surfaces.

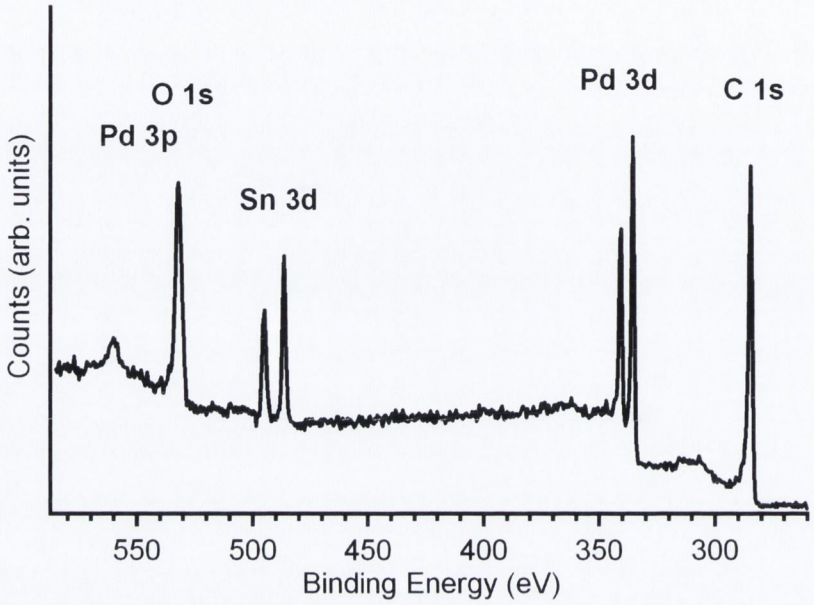

Figure 5.2: XP spectrum of carbon microspheres after undergoing the two step sensitization/activation process that nucleates Pd^0 nanoparticles at the carbon surface (a SEM image of these samples in shown in Figure 5.1c).

5.3.2. Iron deposition utilising method A

In this section the results of ED on CM using method A will be examined. The effects of various bath parameters on homogeneous and heterogeneous processes will be examined

5.3.2.1 Synthesis of Fe/Fe_xO_y CMs using Method A

After sensitization/activation, carbon microspheres were immersed in a solution containing Fe^{2+} at 90 °C, to which sodium hypophosphite was added in order to reduce Fe^{2+}. Figure 5.3a and b show the results of using protocol A on activated CMs for 1 h.

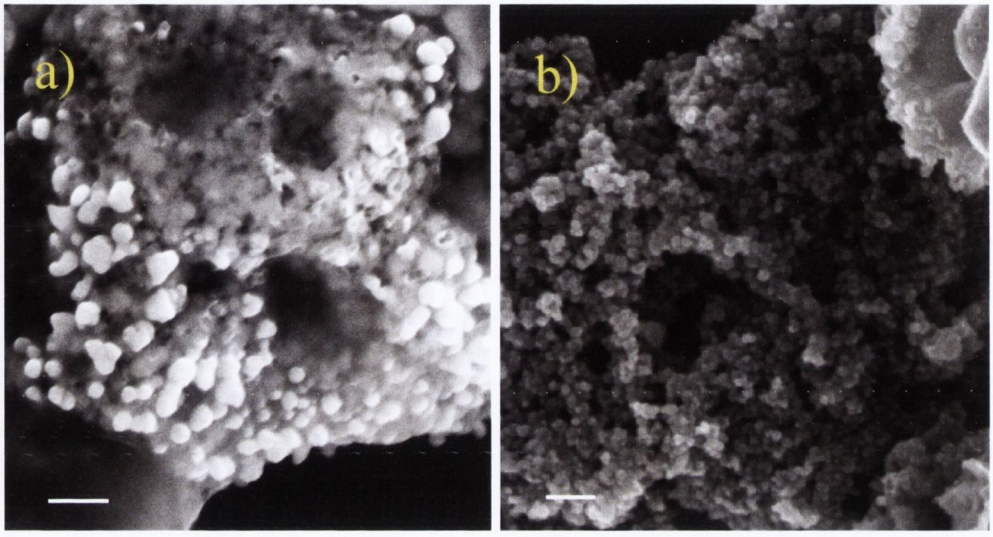

Figure 5.3: SEM image showing CM samples after deposition in hypophosphite and Fe^{2+} showing a) the heterogeneous reaction occurring on the CM surface and b) colloidal particles present which represent the bulk of the sample; Scale bar = 200 nm.

The image show metallic nanoparticles of approximately 100 nm in size growing from the CM surface. However, it does appear that these particles are semi coalesced into a layer, indicating that growth has proceeded beyond the nanoparticle formation range and into the uniform film deposition regime on the CM surface under these conditions. Most of the CMs found after growth using method A for 1 h are completely covered by the metallic layer. In addition to the structures shown in Figure 5.3a we also found an abundance of unsupported particles that cluster around the microsphere scaffolds. This is shown in figure 5.3b which provides an example of a microsphere with a large quantity of unanchored excess particles at its surfaces. This indicates that homogeneous reactions are simultaneously occurring in the ED solution utilising method A. By comparing figure 5.3a and b, the particles produced in homogeneous processes don't appear to have the same morphology as those synthesized at the CM surface. However, care must be given when drawing any conclusions of material difference based from difference in SEM imagery as the surrounding environment can influence how particles appear on SEM. Different rates of charging of sample due to the differing environments of the particles could be responsible. Particles in figure 5.3a

are located on the CM surface which is in contact with the silicon whereas particles from 5.3b are in contact with each other and the wafer directly. This could also justify the differing responses observed. This will be discussed further in the discussion section.

Separation of heterogeneous and homogeneous materials is a serious challenge in further studies on the composite using this protocol. Due to the magnetic properties of Fe and Fe oxides materials, removal of excess particles via centrifugation (as achieved in chapter 4) was not be successful as CM and excess particle aggregates are simply extracted together from the. In order to understand whether method A could be adapted to preferentially yield supported nanoparticles, we decided to alter bath parameters: iron concentration, reductant concentration, temperature and pH. The result of these changes was assessed qualitatively based on examination of SEM images of modified microparticles and their supernatant; quantitative determinations were found to be challenging due to the tendency of iron deposits to aggregate. Figure 5.4 shows the Fe/CM structures obtained after growth using 0.0125 mM iron solutions (all other parameters being equal). We found that at lower iron concentration the growth reduced is reduced at the CM surface. It was observed that ED growth was restricted to smaller particular growth with no metallic layer formation observed. This indicates that iron concentration can influence heterogeneous reductions and the extent to which they occur. However, whilst across the sample a reduction in homogeneous processes was observed, significant quantities of unanchored excess iron remained. This indicated that the homogeneous process was also influenced by the iron concentration.

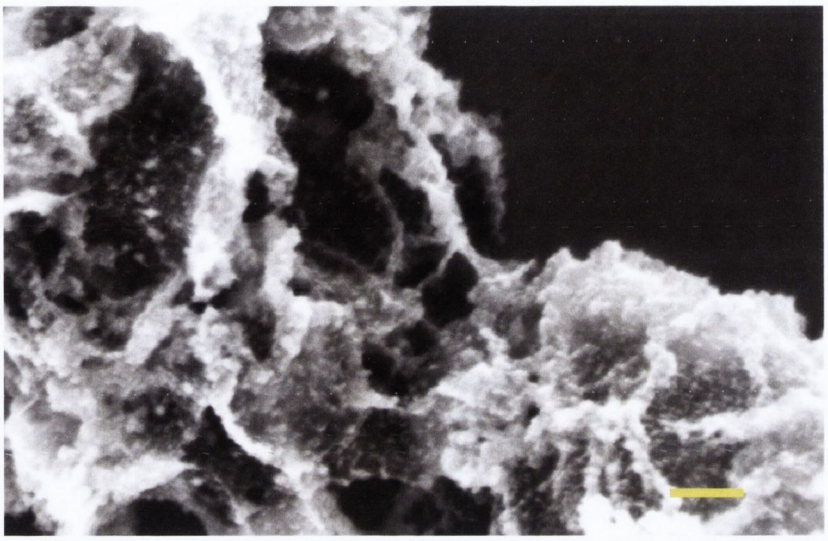

Figure 5.4: SEM images showing CM surface after utilising method A with 0.0125 M Fe^{2+} in solution. Scale bar = 200 nm.

Figure 5.5 shows the CM surface after using method A with a reduced sodium hypophosphite concentration. By reducing sodium hypophosphite concentration in method A to 0.025 M, a reduction in particle growth at the CMsurface is observed, indicating that hypophosphite can influence the rate of heterogeneous reduction. However, across the sample it did not appear to have had an impact on the quantity of unanchored particles, indicating that hypophosphite may not have a role in the formation of observed unanchored particles and this may not be a parameter to change in order to achieve supported particles only.

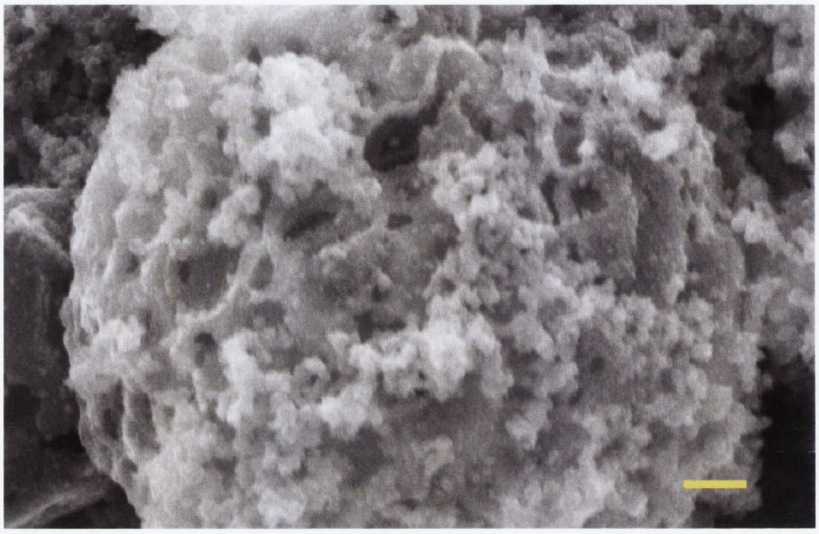

Figure 5.5: SEM images showing CM surface after utilising method A with 0.025 M sodium hypophosphite concentration in solution. Scale bar = 200 nm

Figure 5.6 shows method A performed at room temperature. It was observed that excess unanchored particles are still present in the sample, indicating that temperature over this range is not an important parameter in the prevention of homogenous processes occurring in the ED bath.

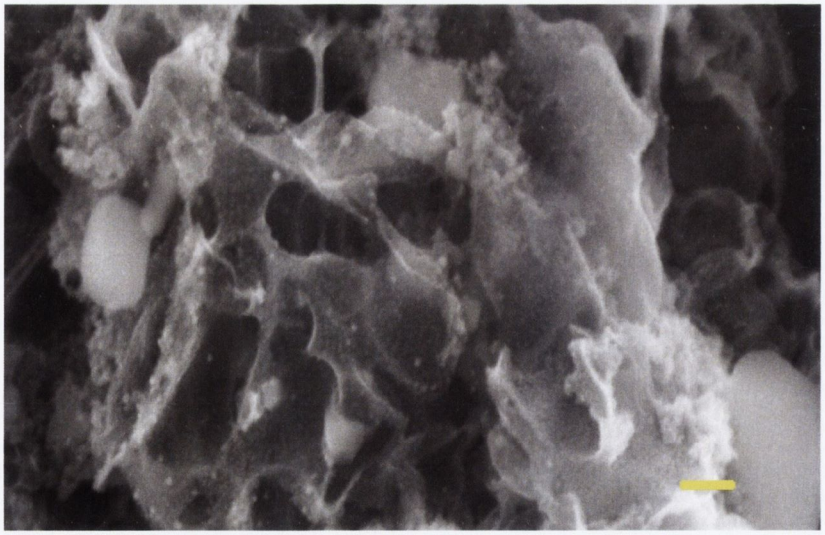

Figure 5.6: SEM images showing CM surface after utilising method A at room temperature. Scale bar = 200 nm

However, no metallic particles bound onto a CM surface which could not be attributed to aggregation with unanchored particles are observed, indicating that for the heterogeneous reduction to occur, higher temperatures are needed. Figure 5.7 shows method A performed at pH 6, no heterogeneously reduced particles on the CM surface were observed, indicating that pH value is important for heterogeneous reduction. In fact, across this sample, no CM was observed with clearly heterogeneous particle growth occurring on the surface which could not be attributed to the activation process and subsequent Pd^0 formation. Also observed in this sample was a significant reduction in the quantity of unanchored particles, although noticeable quantities still remained.

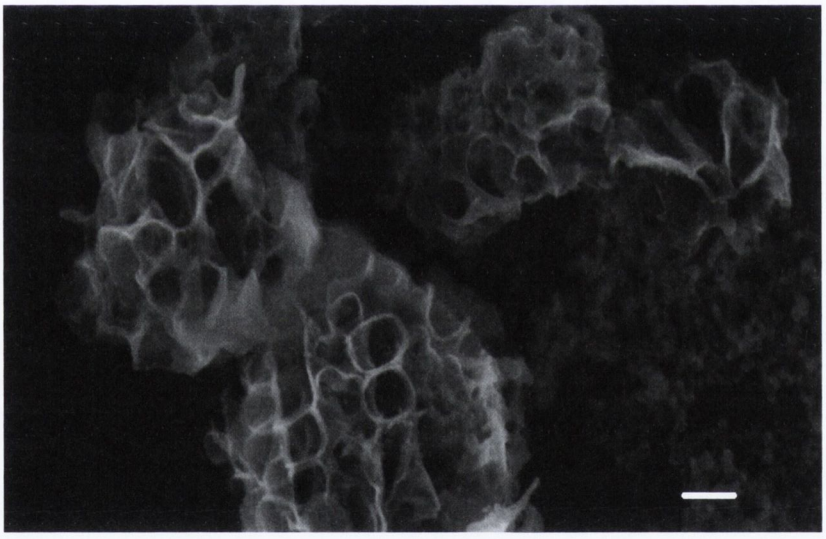

Figure 5.7: SEM images showing CM surface after utilising method A at pH value 6. Scale bar = 300 nm

This indicating that pH may be used to gain a measure of control over the homogeneous processes. However to this date, a composite material using a modified version of method A without significant contamination from homogeneously produced particles has not been obtained. Due to potential interference from irremovable homogeneous Fe species, further characterisation of

this composite material was made impossible at this time. The results from these samples are summarised in table 5.4 and are discussed in more detail in section 5.3.4.

5.3.3 Iron deposition utilising method B

Characterisation of Metal/CM composites obtained using method B will be discussed in this section. The nature of the metallic particles in the composite will be examined, followed by experiments demonstrating the removal capacity of the composite utilising Cr(VI).

5.3.3.1 Synthesis and characterisation of Fe/Fe_xO_y CMs using method B

After sensitization/activation, carbon microspheres were immersed in a solution containing Fe^{3+} at 80 °C, to which DMAB was added in order to lead to the reduction of Fe^{3+}. Figure 5.8a and b show the CM surface after 0.5 and 1.5 h, respectively, in the iron deposition solution. The images show the presence of nanoparticles uniformly covering the CM surface. Importantly, samples have been observed with little or no unanchored particles in the sample, indicating that homogeneous processes are not occurring at a significant rate in this ED solution over the reaction time.

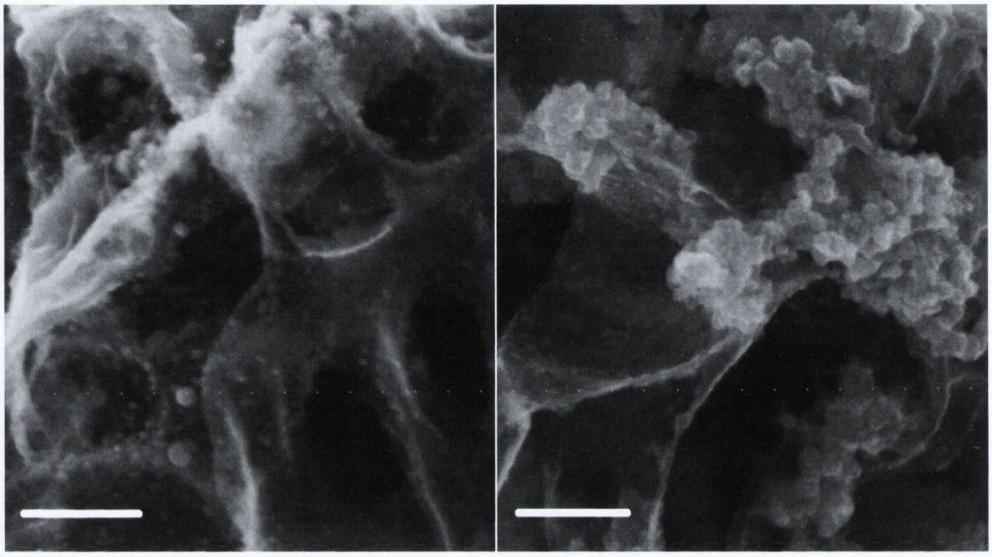

Figure 5.8: Typical SEM images of CMs obtained after deposition in DMAB/Fe^{2+} solution after 0.5 h (a) and after 1.5 h (b); scale bar = 200 nm. The size of primary particles increases with deposition time. (c) Size distribution of iron clusters obtained after 1.5 h of deposition.

After 0.5 h in the deposition bath there is a large population of particles <5 nm in diameter that accounts for the majority of particles that can be discerned in the images, as well as larger particles with a diameter of 13 ± 4 nm, as measured from SEM images. After 1.5 h nanoparticles increase in size to a diameter of 27 ± 8 nm with these primary particles often forming into aggregates that remain anchored at the carbon surface. Figure 5.9 shows the size distribution of particles obtained after 1.5 h in the DMAB/Fe^{3+} bath, determined from SEM images. The nanoparticles that decorate the porous carbon microspheres are not evident prior to the iron deposition step, thus suggesting that particle growth occurs due to electroless deposition of an iron-containing species.

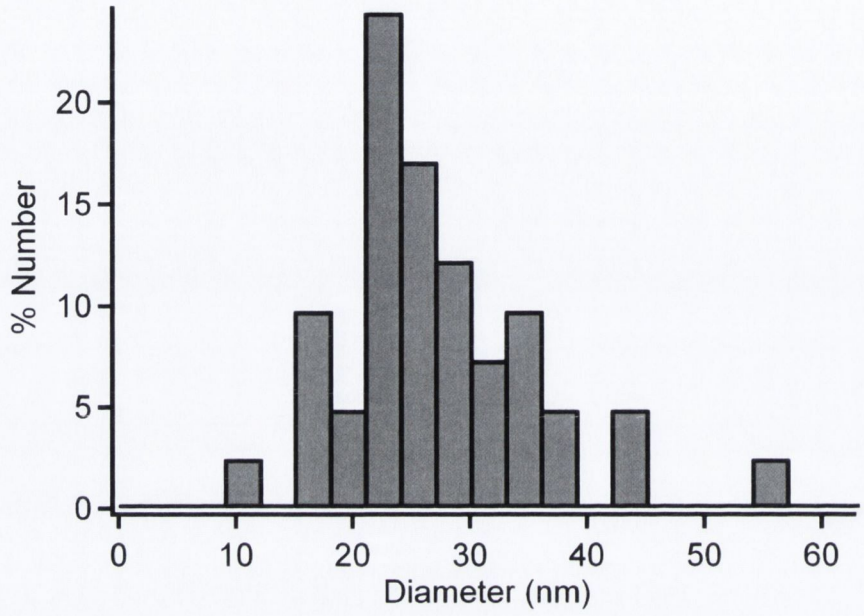

Figure 5.9: Size distribution of iron particles obtained after 1.5 hr deposition.

The composition of metal/carbon composite microspheres was investigated first via powder XRD measurements on Fe-decorated carbon samples. Figure 5.10 shows an XRD pattern of composite Fe/CM powders obtained after 1.5 h deposition. The pattern clearly shows the presence of iron oxides: the lines at 30.2°, 35.5°, 43.2°, 53.6° and 57.1° match the characteristic (220), (311), (400), (422) and (511) reflections of magnetite (Fe_3O_4; JCPDS file no.19 629) or maghemite (γ-Fe_2O_3; JCPDS file no. 25-1402) [25,26] and yielded a lattice constant of 8.37 °A, a value that falls between those of maghemite and magnetite [27]. Both of these oxides have spinel structure and yield similar XRD patterns which cannot be easily distinguished [28]. Additional broad lines suggest that other oxide phases with poor crystallinity contribute to the XRD pattern.

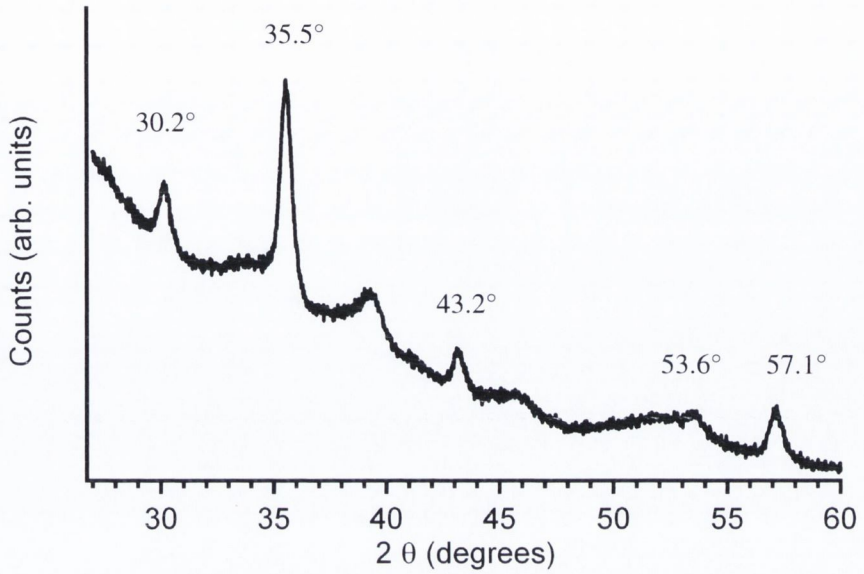

Figure 5.10: XRD pattern obtained after sensitization/activation and deposition in DMAB/Fe^{3+} solutions for 1.5 h on activated CM powders

XAS measurements and EXAFS analysis were carried out at the Synchrotron SOLEIL, Orday, France by our collaborator Dr. Emiliano Fonda.

In order to better understand composition and structure of Fe/CM particles, we carried out X-ray absorption spectroscopy (XAS) measurements. In contrast with XRD, XAS can provide structural and composition information independently from the presence of long range order and is therefore better suited for characterizing disordered iron and iron oxide phases. Furthermore, XAS is sensitive to metal oxidation state and can be used to distinguish oxide phases with similar lattice structures as is the case with maghemite and magnetite [29]. We measured the XAS spectrum of Fe/CM and of iron oxide standards; Fe/CM samples were prepared under the same conditions, dried and kept in air for several weeks prior to XAS measurements. The absorption edge jump was used to estimate an iron content of 14 ± 1% by weight, the pellet was checked for homogeneity with X-rays to estimate possible thickness errors. Figure 5.11 shows the Fe K-edge absorption threshold obtained from our sample compared to standards.

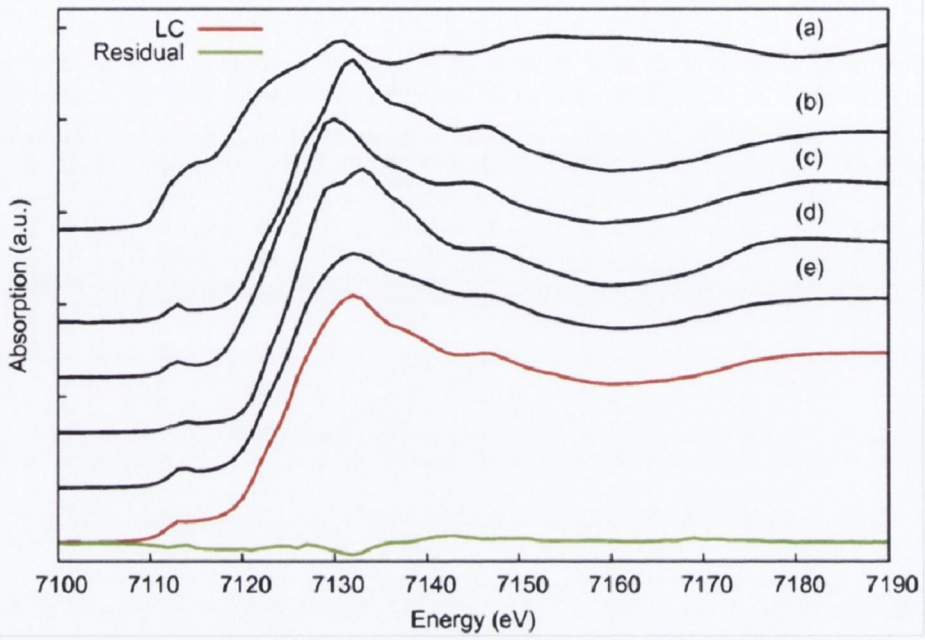

Figure 5.11: Fe K-edge absorption threshold obtained from (a) a-Fe, (b) hematite, (c)magnetite and (d) maghemite standards compared to that of (e) Fe/CM. The linear combination (LC) fit with the parameters reported in Table 1 and the residual are drawn in the bottom traces.

A linear combination fit of the normalized XANES spectrum including all combinations of metallic iron, hematite, maghemite and magnetite was performed and the results are shown in Table 5.2. Under all models, the magnetite is excluded, while hematite and maghemite have similar weights with a non negligible fraction of α-Fe. These results indicate that Fe is present mainly in two forms Fe^{3+} and Fe^{0}.

Components	Fraction
α - Fe	0.18 (0.5)
Hematite (Fe2O3)	0.38 (0.5)
Maghemite (v-Fe2O3)	0.44 (0.5)
Magnetite (Fe3O4)	0.00 (0.5)

Table 5.2: Results of a linear combination fit on XANES data of Fe/CM sample. Error bar is reported in brackets.

EXAFS data analysis was performed in R-space including single scattering contributions of Fe_2O_3 and α-Fe up to 0.35 nm. Figure 5.12 shows a comparison of model and data in k-space (Figure 5.12a) and R-space (Figure 5.12b). Again, it is possible to distinguish the presence of α-Fe mixed with one or more Fe^{3+} oxides. Several parameters where constrained as far as physically meaningful. The α-Fe fraction was left free as well as the lattice parameter, this means that coordination numbers and distances for Fe1 and Fe2 in Table 5.3 are linked by a factor. A similar approach has been used for the oxide phase, but since its signal is stronger, distances of separate shells are left independent in the refinement. It is unlikely to definitely distinguish between maghemite [30] and hematite on the basis of this fit, but it is tempting to compare distances reported in Table 5.3 with those reported for micro or nano maghemite particles by Corrias et al [31]: Fe–O1 at 0.192 nm, Fe–Fe1 at 0.299 nm, Fe–Fe2 0.344 nm, while the same authors found for hematite: Fe–O1 at 0.194 nm, Fe–O2 at 0.210 nm, Fe–Fe1 at 0.289 nm, Fe–Fe2 at 0.297 nm, Fe–Fe3 at 0.336 nm, Fe–Fe4 at 0.370 nm and Fe–Fe5 at 0.398 nm. The correspondence of the EXAFS data of the oxide fraction with micro or nano maghemite is striking.

Path	C.N.	R (nm)	s2 (10^{-5} nm^2)
O1 (oxide)	4.6(9)	0.195(2)	13(3)
Fe1 (a-Fe)	0.7(2)	0.251(2)	7(1)
Fe2 (a-Fe)	C.N.(Fe1)/8 X6	0.290(3)	
Fe3 (oxide)	2.6(5)	0.299(2)	
Fe4 (oxide)	C.N.(Fe3)	0.343(2)	

Table 5.3: Summary of scattering paths obtained from a best fit of the EXAFS spectrum of Fe/CM powders

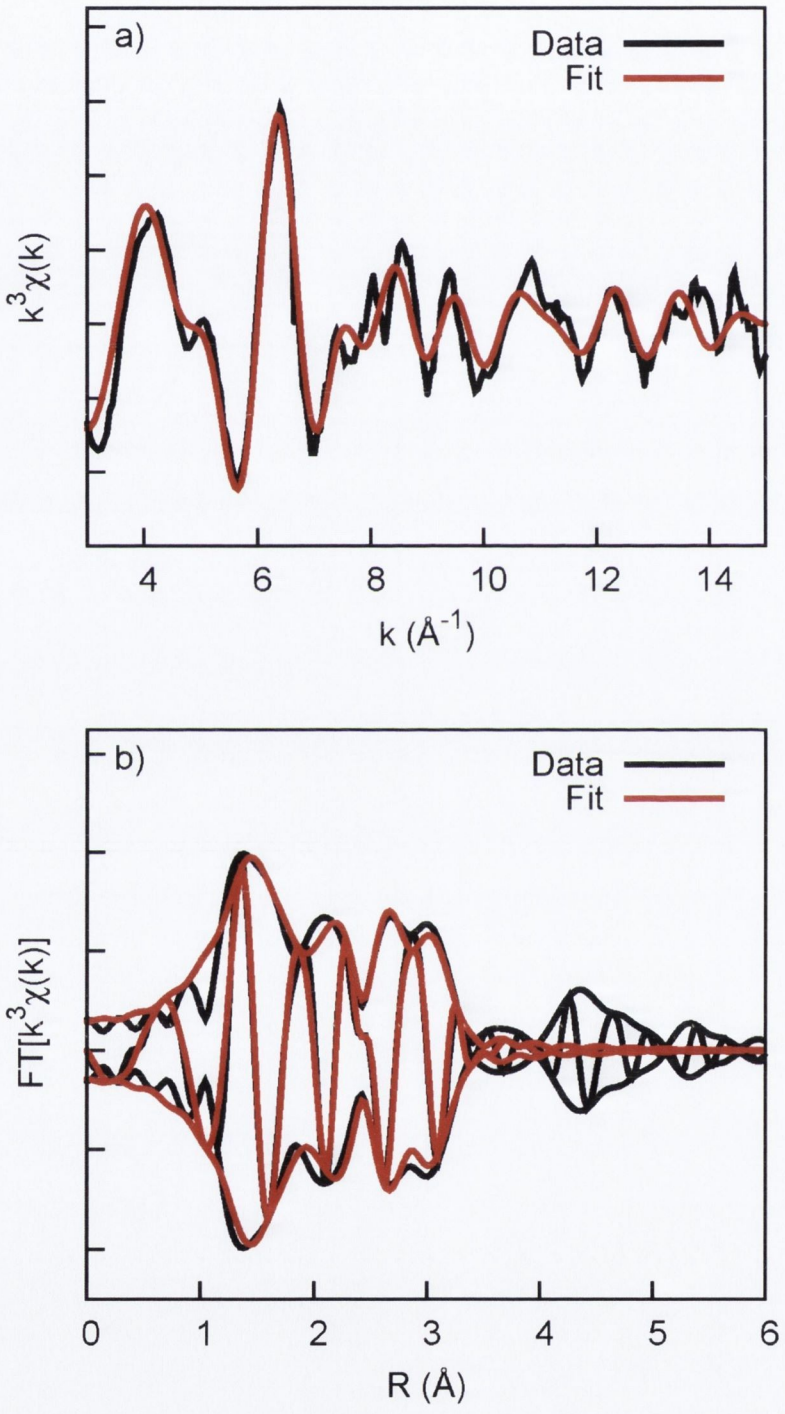

Figure 5.12: k3-weighted EXAFS data of Fe/CM compared to the fitting curve in k-space **(a)** and R-space **(b)**. The model did not include distances larger than 0.35 nm.

Assignment of the oxide phase to maghemite is also in agreement with XRD patterns which did not show the presence of hematite in electrolessly deposited Fe/CM samples. Finally, results confirm the presence of at least 12 ± 3% of Fe^0 which is in good agreement with the fraction reported in Table 5.2 obtained from XANES data. Taking into account a 14% (w/w) iron content, this result suggests that the Fe^0 content of the composite is approximately 1.7% by weight; this value is below typical limits of detection for XRD of crystalline phases in amorphous matrices (>2%) [32] and it could explains our inability to resolve Fe^0 lines in XRD patterns of Fe/CM particles (Figure 5.10).

5.3.3.2 Removal of Cr(VI)

Following the structural characterisation of Fe/CM microspheres we investigated their properties for the removal of pollutants. The removal of Cr(VI) species, in particular, is of utmost importance in water treatment processes due to the toxic properties of this high-valent metal species; carbon particles, iron and iron oxides have all been used in order to remediate Cr(VI) contaminated waters. Therefore, we decided to investigate whether our composite particles, which contain these three types of materials, could remove Cr(VI) from aqueous solutions. The removal curves shown in Figure 5.13 show that when Fe/CM composite microspheres are added to an aqueous solution of Cr(VI), the concentration of this pollutant decreases as a function of time in the aqueous phase. In order to compare the removal capacity of Fe/CM particles to that of bare carbon microspheres, we carried out control adsorption experiments using pristine CMs. The concentration of carbon particles used in the controls was chosen in order to match the number density of Fe/CM used in Cr(VI) adsorption experiments. Figure 5.13 shows the result of a control experiment using pristine carbon microsphere suspensions. The adsorption curve indicates that the maximum removal capacity of an equivalent quantity of carbon microspheres is lower than that of Fe/CM particles, indicating that the Fe/Fe_xO_y phase on the composite material is active in Cr(VI) removal and increases overall performance.

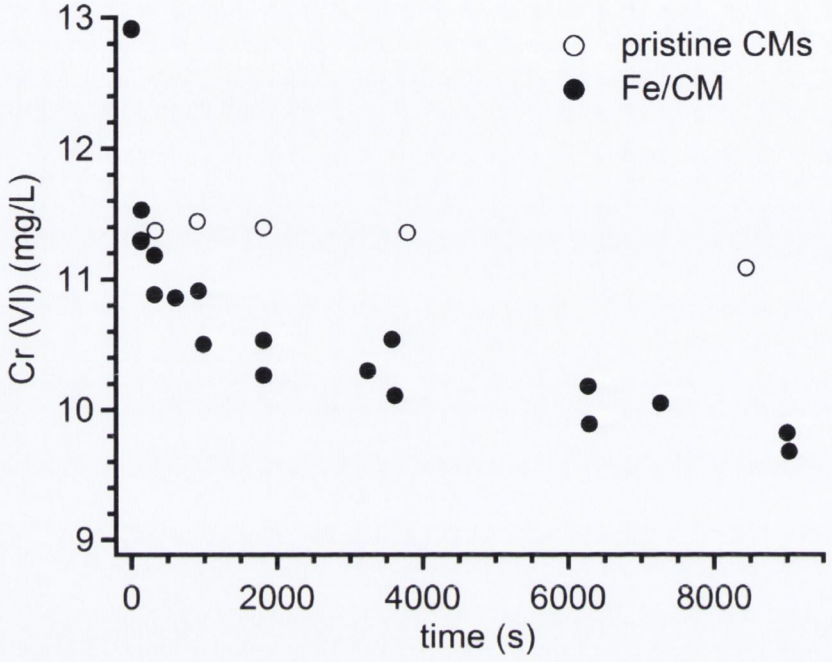

Figure 5.13: Cr(VI) removal from solution as a function of time for pristine CM and Fe/CM particles

An interpolation of adsorption curves using exponentials yielded maximum adsorption capacities for carbon microspheres and Fe/CM particles under our experimental conditions of (22 ± 1) mg g^{-1} and (20 ± 2) mg g^{-1}, respectively. The adsorption capacity of pristine carbon microspheres is within the range of carbon adsorbents [33] and comparable to that of activated carbon particles [34,35]. This result suggests that carbon particles prepared via USP from NaDCA precursors are promising reactive/adsorbing scaffold materials for Cr(VI) removal. See section 5.3.4.2 for more in depth analysis and discussion of Cr(VI) removal

5.3.4 Discussion and summary

Fe/Fe_xO_y nanoparticles were successfully grown on CM surfaces via heterogeneous reduction using two different ED methods. However, method A was not characterised further due to competing homogeneous reactions occurring simultaneously in solution. Various conditions in this ED bath were varied in order to determine the source of the homogeneous reactions. Method B proved more suitable for further characterisation due to a lack of unsupported particles. Subsequently, the size and morphology of nanoparticles grown via ED method B could be studied. It was found that increased duration in the plating solution influenced particle size. The crystalline and metallic nature of the particles located at the carbon surface was confirmed via XRD and EXAFS measurements. The loadings due to heterogeneous catalysis were calculated to be (13.5 ± 1.5)% w/w, for the $Fe/Fe_xO_y/C$ materials. The composite was shown to be active in the removal of Cr(VI) from aqueous solutions. In this section, we discuss these results, implications and suggest some further experiments that may need to be performed to confirm assertions.

5.3.4.1 Method A

Firstly, it was determined that it is possible to produce composite materials via ED techniques using method A. However, homogeneous reactions limit the experimentation, characterisation and applications of this composite. SEM images indicated that heterogeneous and homogeneous processes could follow different pathways. Table 5.4 supports this statement by the various changes made to the components in the ED solution, affecting the two processes in different manners. Table 5.4 indicates that heterogeneous deposition is affected by temperature, pH, metal ion concentration and reducing agent concentration, in agreement with the literature for heterogeneous reductions using hypophosphite. Many researchers have reported that changes in the concentration of hypophosphite or Fe ion concentration results in a change in deposition rate onto flat surfaces [7,36,37].

Condition	Effect on Heterogeneous process	Effect on Homogeneous process
Standard method	100nm particles/layer	significant quantities
Reduced Fe ion Conc	Reduced particle size	Reduced quantities
Reduced H_2PO_3 Conc	Reduced particle size	Normal
pH varied to 6	No particles	Vastly reduced quantities
Room temperature	No particles	Normal

Table 5.4: Summary of ED conditions for method A

It has also been shown that for Fe baths, hypophosphite does not become active as a reducing agent on catalytic surfaces until the temperature increases above 50 °C, supporting our observation of no heterogeneous activity at room temperature. This result is in stark contrast to homogeneous processes which are observed to occur at room temperature. Coupling this with hypophosphite concentration not affecting the amount of unsupported particles produce indicates that the homogeneous process is independent of the reducing agent, supporting the hypothesis that the homogeneous and heterogeneous processes follow different pathways. A proposed pathway for homogeneous deposition is discussed below.

The table shows that the increased concentration of OH^- ions and Fe^{2+} ions increased the rate of homogeneous reactions in the ED bath. Using this observation, eqn 5.3 demonstrates the well documented process of Fe ions undergo precipitation reactions in basic solutions [38]. Such precipitate reactions occur at room temperature and would explain all of the properties for homogeneous particles observed above. However, in method A the Glycine is present as a chelating agent

$$Fe^{2+}{}_{aq} + 2OH^-{}_{aq} \rightarrow Fe(OH)_{2\,s} \qquad \text{eqn 5.3}$$

in order to increase the solubility and stability of Fe ions, in an effort to minimise and prevent such precipitation reactions represented in eqn 5.3. However, control experiments performed with no Glycine present confirmed its activity as a stabilising agent due to rapid ED bath decomposed occurring, with visible solution turbidity and precipitation of a dark solid. Figure 5.14 shows on SEM image of a sample taken from the bath after 5 min where particles with very similar morphology to colloid particles in figure 5.3b are observed to be forming in micrometer sized aggregates.

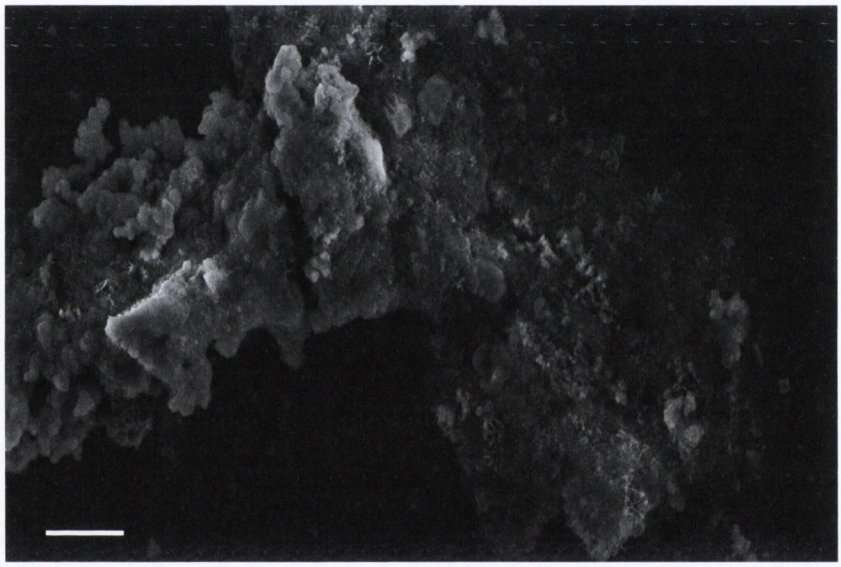

Figure 5.14: Shows the resulting decomposition of Bath A absent glycine; Scale bar = 4 μm

These results demonstrate that the presence of Glycine does not prevent bath decomposition; it merely improves the bath lifetime by slowing the kinetics of decomposition by chelating to the Fe^{2+} ion. This is effective technique for deposition on flat surfaces due to the ease of removal of unwanted colloid particles via washings and the ease of separating the plated surface from the bath. However, even at low rates of bath decomposition, these particles represent a serious challenge in further experimentation on Fe/Fe_xO_y composites using CM due to the lack of an effective separation technique for the ED bath. Control experiment using pristine CMs in a bath absent hypophosite ions could confirm the above hypothesis for the source of

unsupported particles. This would rule out heterogenous processes at the Pd^0 surface and confirm that the process can occur spontaneously at high pH without the presence of a reducing agent. Subsequent XRD measurements on the control and Method A sample could possible confirm if the same Iron oxide phase is present, confirming the theory.

5.3.4.2 Method B

Using the deposition methods of Nakanishi et al it was possible to successfully synthesis a Fe/FeO composite material. This method did not have the same problems as method A, obtaining CMs free from unsupported NPs. However, Fe^{3+} has been shown to precipitate into iron oxide/hydroxide phases as well as Fe^{2+} and considering this ED method doesn't have a chelating agent it is surprising to find a minimum of unsupported particles. Two explanations for this are the Fe^{3+} ion concentration in solution and the pH of the solution. Method B has an Fe^{3+} ion concentration of 1 mM where as Method A had a Fe^{2+} ion concentration of 0.05 M. A concentration of iron 50 times greater is not insignificant. However, even at this relative low concentration excess particles should be observable if any homogeneous reactions are taking place. This indicates the most likely reason for the lack of unsupported particles is the pH. Method B proceeds at a pH of 8 as measured in our laboratory, facilitating a vast reduction in the number of OH^- ions in solution when compared to method A which proceeds at pH 10.5. This reduction in concentration likely facilitates a decrease in the kinetic rate of the Fe precipitation reaction allowing heterogeneous deposition to dominate in the short term kinetics.

For method B it was observed that particle size increases with longer duration in the ED solution. This is in agreement with expected behaviour of ED systems. This result is supported quantitatively by figure 5.15 which shows TGA of composite samples after undergoing deposition for 0.5 hr and 1.5 hr with residual masses of 48.6% and 60.6% being obtained respectively.

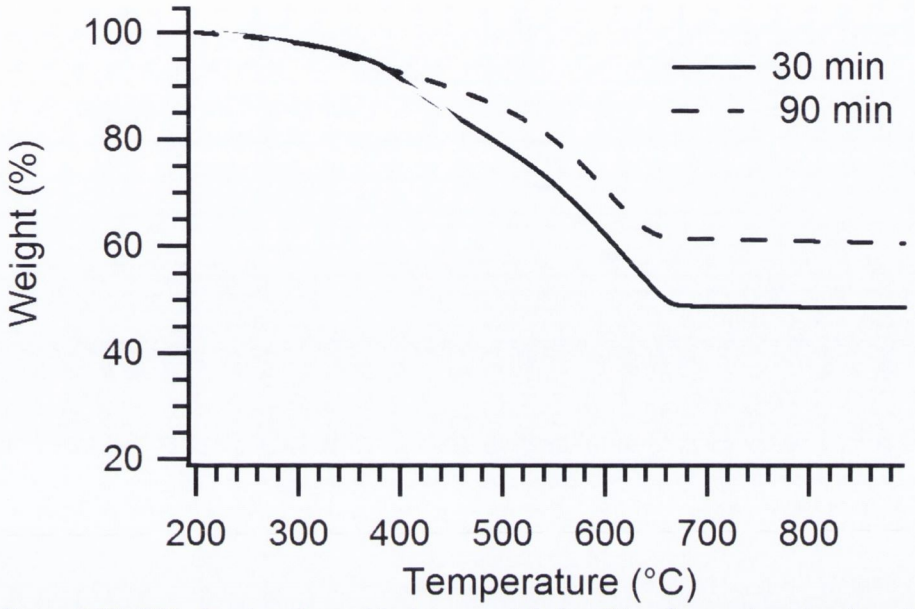

Figure 5.15: TGA showing the residual masses left for CMs after undergoing deposition for various ED times

Greater mass present in the sample with increased deposition time is likely due to continued deposition on smaller particles. However, upon trying to obtain even larger particles it was noted that particle size didn't appear to get any larger with plating times longer than 90 min, indicating that there is a limiting factor in this particular system. Figure 5.16 shows a CM after undergoing deposition for a period of 2.5 hr with particles observed in the 15 - 40nm size range, indicating that growth slows with increased particle size. Fujita et al observed similar behaviour for thin iron films electrolessly deposited using sodium Borohydride as a reducing agent [6]. They hypothesised that the reduction in growth after a short time period was due to the low catalytic activity of Iron.

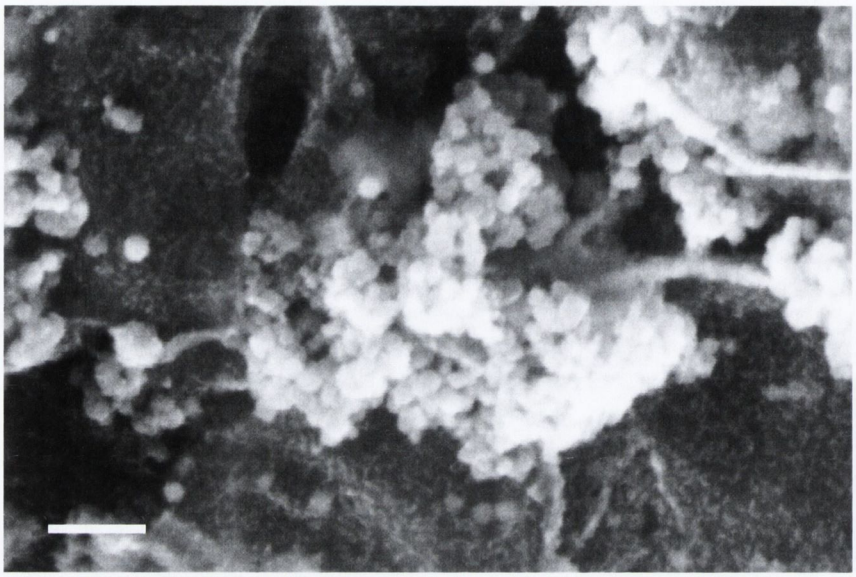

Figure 5.16: SEM showing NPs at the CM surface after 2.5 hr deposition utilising method B

As borohydride is theorised to have similar reaction mechanics as DMAB, limited catalytic activity could be responsible for the results observed above. However, care must be taking in drawing conclusions of this type, as while the mechanisms for the two reducing agents are similar, it has been stated they are not the same for catalytic surfaces such as Au and Pt [39]. Further TGA experiments for longer deposition times could confirm the extent of growth decrease and also show if a limit to particle size using method B exists.

XRD results indicated the presence of either a Maghemite or a magnetite iron oxide phase. However, XANES data excluded the presence of Fe_3O_4, indicating that the oxide layer in the XRD pattern is maghemite - Fe_2O_3. However, the presence of a Fe (bcc) phase could not be detected in any of the powder samples, as indicated by the absence of a (110) line at 44°. Figure 5.17 shows the same electroless deposition process used to deposit a film on a flat carbon substrate.

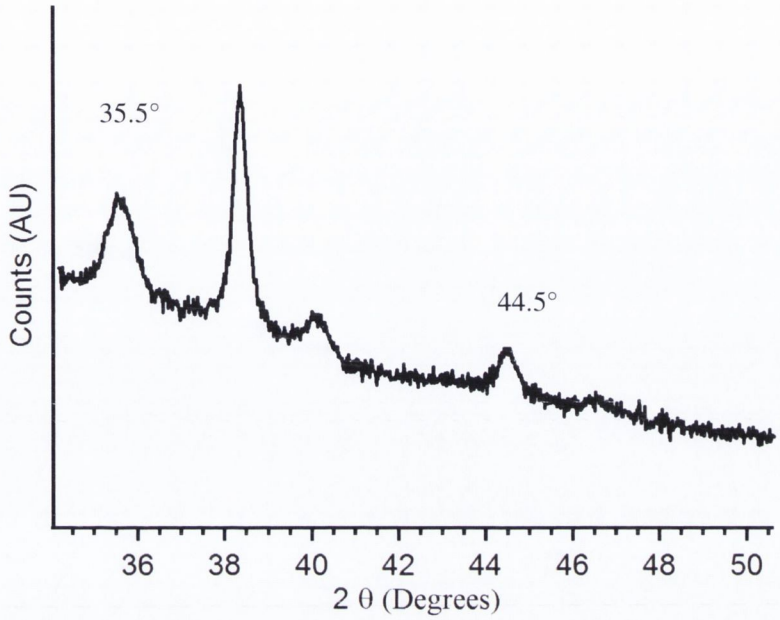

Figure 5.17: XRD of method B performed on a flat carbon surface

This pattern shows a peak at 44.5° indicating a (110) a-Fe reflection, in agreement with results by Nakanishi et al [8], indicating that Fe metal is present in the composite material. The (311) reflection for Fe_2O_3 is also observed at 35.5° indicating the presence of iron oxide. XRD results on microsphere samples therefore suggest 3 possibilities, i) metallic iron is not formed using CMs, ii) it is present below the limit of detection when CMs are used as scaffolds for electroless deposition or iii) XRD results indicating the presence of iron oxides at the carbon surface, could originate from air exposure after deposition and isolation of Fe/CM microspheres [40] or even result from metal hydroxide formation during DMAB electroless deposition [8,41,42]. XANES results coupled with Figure 5.17 exclude possibility i) via the detection of an Fe^0 phase. Considering that Nakashima et al detected no oxide phase using the same protocol and that XANES CM samples exposed to air for several days still had a significant amount of Fe^0 present, it is likely that ii) and iii) are both occurring for the XRD measurements. Furthermore, figure 5.17 shows an oxide peak at 35.5° which Nakashima et al don't observe, indicating that post ED oxidation is likely to be occurring in our samples,

further supporting iii). An experiment with the XRD measurement being run on a sample that is enclosed in an inert atmosphere could confirm the above statements unequivocally if a peak at 44° becomes resolved with no oxide peaks for a flat surface. However, to this date this measurement has proved difficult to perform.

EDS line mappings shown are Figure 5.18. Ideally a long time 2d mapping would have been performed here. However, sample drift did not allow for long time measurements so quick line scan measurements were taken.

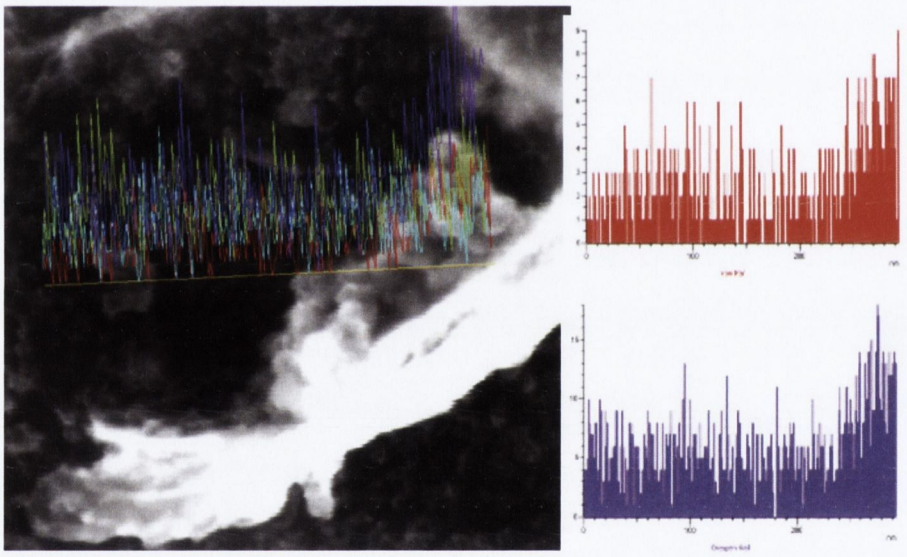

Figure 5.18: EDX linescan performed on composite material with the red scan representing counts for iron and purple representing oxygen

The count number is very low, however there is just enough to discern a match of highest Fe and O concentrations with particles observed via SEM on the CM surface. This suggests that particles observed on the CM surface are directly responsible for peaks observed via XRD. XRD further supports that nanoparticles are responsible for the observed peaks due to peak broadening which indicates small crystalline domain size, not indicative of layers or thin films. Coupling EDS/XRD/XANES and EXAFS, it is possible to conclude that Fe/Fe_xO_y particles have been grown via ED at the CM surface.

Experiments were performed on the composite material which indicated that the composite material has increased removal capacity per CM for Cr(VI) comparing to pristine CMs. Normalization by the specific surface area of NaDCA particles yielded a maximum surface density value for adsorbed Cr at the pristine carbon surface of (46 ± 2) μg m^{-2}. The BET area of Fe/CM particles was found to be 335 m^2 g^{-1}, thus yielding a maximum surface density of adsorbed Cr of (60 ± 6) μg m^{-2}. This result indicates that the surface of Fe/CM composite particles is ~30% more effective on average than that of carbon alone at capturing Cr(VI) from solution under the same conditions. Both metallic Fe^0 and iron oxides can contribute to the removal of Cr(VI) from solution albeit via different mechanisms. Metallic iron can reduce Cr(VI) to less mobile Cr(III) species, as shown by the work of numerous groups on the use of iron nanoparticles in water remediation [43-46]. The reductive properties of iron nanoparticles can also be enhanced via Pd-doping of iron nanoparticles [45], however, it is not possible to establish whether Pd present in our particles enhances the removal capacity of Fe/CM composites, based on the present results alone. Iron oxides can remove metal contaminants via a process of surface complexation and ion exchange [47-49]; hydrated iron oxide surfaces are, in fact, excellent at complexing and sequestering both Cr(VI) and Cr(III) species from solution and have been extensively used in the treatment of waste waters contaminated with chromate [28]. Assuming that the enhanced adsorption observed in Figure 5.13 arises entirely from the presence of Fe_2O_3, and using %weight contents determined via XANES, we can estimate that the removal capacity of Fe_2O_3 oxides in Fe/CM particles is approximately 46 mg g^{-1}. This value is extremely high compared to typical Cr(VI) removal capacities: Zhong et al [49] for instance, reported values of 3.86 mg g^{-1} and 4.75 mg g^{-1} for pure maghemite and hematite nanostructures, whereas Hu et al [50] achieved maximum removals of 20 mg g^{-1} for synthesized maghemite nanoparticles. This suggests that higher surface availability due to anchoring at the carbon scaffold and/or a simultaneous reductive removal mechanism might contribute to the high adsorption capacities observed for our supported Fe/Fe_xO_y particles. Experiments using a contaminant which reacts to the

reductive performance of Fe^0 alone and not iron oxide would give more insight into which iron phases are responsible for the various degrees of Cr(VI) removal. The removal of nitrate by Fe^0 is well documented and removal of nitrate by iron (III) oxide phases does not readily occur [51-54]. Hence, this would be an ideal reaction for further experimentation and study of the composite material.

5.4 Conclusions

We have confirmed the metallic nature of the Pd islands observed on the CM surface via XPS experiments. We have shown that ED methods can be used to deposit iron nanoparticles at the activated surface of porous carbon microspheres. We have demonstrated that methods used by Drovosekov et al are currently unviable on CM surfaces due to significant amounts of inseparable unsupported NPs. However, the methods proposed by Nakashima et al did not have this problem and were suitable for further characterisation. We have used a combination of electron microscopy, X-ray photoelectron spectroscopy, X-ray diffraction and X-ray absorption techniques in order to determine morphology and composition of the resulting inorganic nanoparticles. We showed that the nanostructured deposits obtained via ED consist of mixed metallic and oxide phases. Analysis of X-ray absorption edge and fine structure (XANES and EXAFS) were essential in order to both detect the presence of metallic iron and to determine that the majority of the oxide phase consisted of maghemite as supported by XRD data. Adsorption experiments indicate that Fe/CM particles prepared via ED are highly effective at removing chromate from aqueous solutions. Fe/CM particles were shown to perform better than the carbon scaffold alone. The Cr(VI) removal mechanism is expected to result from the combination of reductive and adsorptive processes, given that Fe^0, maghemite and carbon are all present and potentially active towards chromate capture from solution. These mixed material microspheres appear to be promising for the design of new adsorptive/reactive agents in environmental remediation. Furthermore, we envision that the ability to anchor Fe/FeOx

nanoparticles at carbon microparticle surfaces could be advantageous in order to improve handling, aggregation and transport properties of nanosized iron-based materials.

Reference

(1) Son, Y.-H.; Lee, J.-K.; Soong, Y.; Martello, D.; Chyu, M. *Chemistry of Materials* **2010**, *22*, 2226.

(2) Lee, J.; Lee, D.; Oh, E.; Kim, J.; Kim, Y. P.; Jin, S.; Kim, H. S.; Hwang, Y.; Kwak, J. H.; Park, J. G. *Angewandte Chemie* **2005**, *117*, 7593.

(3) Schrick, B.; Hydutsky, B. W.; Blough, J. L.; Mallouk, T. E. *Chemistry of Materials* **2004**, *16*, 2187.

(4) Atkinson, J. D.; Fortunato, M. E.; Dastgheib, S. A.; Rostam-Abadi, M.; Rood, M. J.; Suslick, K. S. *Carbon* **2011**, *49*, 587.

(5) Zheng, T.; Zhan, J.; He, J.; Day, C.; Lu, Y.; McPherson, G. L.; Piringer, G.; John, V. T. *Environmental Science & Technology* **2008**, *42*, 4494.

(6) Fujita, N.; Tanaka, A.; Makino, E.; Squire, P. T.; Lim, P. B.; Inoue, M.; Fujii, T. *Applied surface science* **1997**, *113*, 61.

(7) Drovosekov, A.; Ivanov, M.; Lubnin, E. *Protection of metals* **2004**, *40*, 89.

(8) Nakanishi, T.; Masuda, Y.; Koumoto, K. *Journal of crystal growth* **2005**, *284*, 176.

(9) Mandado, M.; Cordeiro, M. *Journal of Computational Chemistry* **2010**, *31*, 2735.

(10) Cullen, R. J.; Jayasundara, D. R.; Soldi, L.; Cheng, J. J.; Dufaure, G.; Colavita, P. E. *Chemistry of Materials* **2012**, *24*, 1031.

(11) Duffy, P.; Magno, L. M.; Yadav, R. B.; Roberts, S. K.; Ward, A. D.; Botchway, S. W.; Colavita, P. E.; Quinn, S. J. *Journal of Materials Chemistry* **2012**, *22*, 432.

(12) Skrabalak, S. E.; Suslick, K. S. *Journal of the American Chemical Society* **2006**, *128*, 12642.

(13) Brunauer, S.; Emmett, P. H.; Teller, E. *Journal of the American Chemical Society* **1938**, *60*, 309.

(14) V. Broise, E. F., S. Belin, L. Barthe, C. La Fontaine, F. Langlois, M. Ribbens and F. Villain, SAMBA.

(15) Ravel, B.; Newville, M. *Journal of synchrotron radiation* **2005**, *12*, 537.

(16) Ankudinov, A.; Nesvizhskii, A.; Rehr, J. *Physical Review B* **2003**, *67*, 115120.

(17) Xia, L.; Akiyama, E.; Frankel, G.; McCreery, R. *Journal of The Electrochemical Society* **2000**, *147*, 2556.

(18) Charbonnier, M.; Alami, M.; Romand, M. *Journal of applied electrochemistry* **1998**, *28*, 449.

(19) Kind, H.; Bittner, A. M.; Cavalleri, O.; Kern, K.; Greber, T. *The Journal of Physical Chemistry B* **1998**, *102*, 7582.

(20) Wertheim, G.; DiCenzo, S.; Buchanan, D. *Physical Review B* **1986**, *33*, 5384.

(21) Ishii, D.; Nagashima, T.; Udatsu, M.; Sun, R.-D.; Ishikawa, Y.; Kawasaki, S.; Yamada, M.; Iyoda, T.; Nakagawa, M. *Chemistry of Materials* **2006**, *18*, 2152.

(22) Kim, K. S.; Gossmann, A.; Winograd, N. *Analytical Chemistry* **1974**, *46*, 197.

(23) Paparazzo, E.; Fierro, G.; Ingo, G.; Zacchetti, N. *Surface and Interface Analysis* **1988**, *12*, 438.

(24) Ansell, R.; Dickinson, T.; Povey, A.; Sherwood, P. *Journal of The Electrochemical Society* **1977**, *124*, 1360.

(25) Grabs, I.-M.; Bradtmöller, C.; Menzel, D.; Garnweitner, G. *Crystal Growth & Design* **2012**, *12*, 1469.

(26) Sun, Y.-k.; Ma, M.; Zhang, Y.; Gu, N. *Colloids and Surfaces A: Physicochemical and Engineering Aspects* **2004**, *245*, 15.

(27) Schwertmann, U.; Cornell, R. M. *Iron oxides in the laboratory*; John Wiley & Sons, 2008.

(28) Cornell, R. M.; Schwertmann, U. *The iron oxides: structure, properties, reactions, occurrences and uses*; Wiley. com, 2003.

(29) Espinosa, A.; Serrano, A.; Llavona, A.; de la Morena, J. J.; Abuin, M.; Figuerola, A.; Pellegrino, T.; Fernández, J.; Garcia-Hernandez, M.; Castro, G. *Measurement Science and Technology* **2012**, *23*, 015602.

(30) Pecharromán, C.; González-Carreno, T.; Iglesias, J. E. *Physics and Chemistry of Minerals* **1995**, *22*, 21.

(31) Corrias, A.; Ennas, G.; Mountjoy, G.; Paschina, G. *Physical Chemistry Chemical Physics* **2000**, *2*, 1045.

(32) Sarsfield, B.; Davidovich, M.; Desikan, S.; Fakes, M.; Futernik, S.; Hilden, J.; Tan, J.; Yin, S.; Young, G.; Vakkalagadda, B. *Advances in X-ray Analysis* **2006**, *49*, 322.

(33) Owlad, M.; Aroua, M. K.; Daud, W. A. W.; Baroutian, S. *Water, Air, and Soil Pollution* **2009**, *200*, 59.

(34) Babel, S.; Kurniawan, T. A. *Chemosphere* **2004**, *54*, 951.

(35) Han, I.; Schlautman, M. A.; Batchelor, B. *Water Environment Research* **2000**, 29.

(36) Huang, G.-F.; Huang, W.-Q.; Wang, L.-L.; Zou, B.-S.; Wang, Q.-L.; Zhang, J.-H.; Fe, E. *INTERNATIONAL JOURNAL OF ELECTROCHEMICAL SCIENCE* **2008**, *3*, 145.

(37) Ruscior, C.; CroialĂ, E. *Journal of The Electrochemical Society* **1971**, *118*, 696.

(38) Misawa, T.; Hashimoto, K.; Shimodaira, S. *Corrosion science* **1974**, *14*, 131.

(39) Finkelstein, D. A.; Mota, N. D.; Cohen, J. L.; Abruña, H. D. *The Journal of Physical Chemistry C* **2009**, *113*, 19700.

(40) Li, S.; Yan, W.; Zhang, W.-x. *Green Chemistry* **2009**, *11*, 1618.

(41) Balci, S.; Bittner, A.; Schirra, M.; Thonke, K.; Sauer, R.; Hahn, K.; Kadri, A.; Wege, C.; Jeske, H.; Kern, K. *Electrochimica Acta* **2009**, *54*, 5149.

(42) Krutskikh, V.; Ivanov, M.; Drovosekov, A.; Lubnin, E.; Lyakhov, B.; Polukarov, Y. M. *Protection of metals* **2007**, *43*, 560.

(43) Melitas, N.; Chuffe-Moscoso, O.; Farrell, J. *Environmental Science & Technology* **2001**, *35*, 3948.

(44) Ponder, S. M.; Darab, J. G.; Mallouk, T. E. *Environmental Science & Technology* **2000**, *34*, 2564.

(45) Li, X. Q.; Elliott, D. W.; Zhang, W. X. *Critical Reviews in Solid State and Materials Sciences* **2006**, *31*, 111.

(46) Xu, Y. H.; Zhao, D. Y. *Water Research* **2007**, *41*, 2101.

(47) Dzombak, D. A.; Morel, F. M. *Surface complexation modeling: hydrous ferric oxide*; Wiley New York, 1990; Vol. 393.

(48) Waychunas, G. A.; Kim, C. S.; Banfield, J. F. *Journal of Nanoparticle Research* **2005**, *7*, 409.

(49) Zhong, L. S.; Hu, J. S.; Liang, H. P.; Cao, A. M.; Song, W. G.; Wan, L. J. *Advanced Materials* **2006**, *18*, 2426.

(50) Hu, J.; Chen, G.; Lo, I. *Water Research* **2005**, *39*, 4528.

(51) Sohn, K.; Kang, S. W.; Ahn, S.; Woo, M.; Yang, S. K. *Environmental Science & Technology* **2006**, *40*, 5514.

(52) Westerhoff, P.; James, J. *Water Research* **2003**, *37*, 1818.

(53) Alowitz, M. J.; Scherer, M. M. *Environmental Science & Technology* **2002**, *36*, 299.

(54) Park, H.; Yeon, K.-H.; Park, Y.-M.; Lee, S.-J.; Lee, S.-H.; Choi, Y.-S.; Chung, Y. *Journal of Water and Environment Technology* **2008**, *6*, 35.

Chapter 6

Conclusions and future work

Herein all the main conclusions from this report will be stated. Further work and experiments will also be suggested in order to improve the work enclosed in this report for the future.

6.1 Conclusions

In this work, we can conclude that carbon microparticles synthesized utilising USP are suitable as a solid support material for nanoparticles. Hence CMs can potentially be used as a transport/delivery vehicle for NPs. Firstly, it was shown that CM synthesized using USP can be synthesised with varying morphologies and surface areas. Secondly, we demonstrated that leveraging the properties of the USP technique, it is possible to control the size of CMs. Finally, using diazonium chemistries, it was shown that CMs have a surface which has changable surface moieties and surface charge.

Next we can conclude that using electroless deposition procedures it is possible to synthesis metal/carbon composites on these CMs. It was confirmed that Ag and Pd nanoparticles were anchored onto the carbon surface using "green" electroless deposition procedures which utilised coffee as a reducing agent at room temperature. It was confirmed that the sensitisation and activation procedures are crucial in achieving surface immobilisation of the metal nanoparticles. The metal surfaces in these composite materials were shown to be still catalytically active. Pd/C was active in the Suzuki coupling and Ag/C was active in the reduction of 4-nitrophenol.

Next, it was shown that electroless deposition of Fe/Fe_xO_y nanoparticles was possible utilising DMAB as a reducing agent and Fe^{3+} as an iron source. The morphology of particles synthesized using this protocol were confirmed to contain both Fe^0 and Fe^{3+} oxidation states of iron. The carbon surface of the composite and the Fe^{3+} where shown to be active towards Cr(VI) removal from an aqueous solution.

6.2 Future work

CM transport studies in columns of porous matrices would be of benefit in showing the potential of the CMs for applications involving them as a delivery vehicle. Studies on the pristine CMs would be performed with rigour comparisons in performance to CMs with surface charge modification and size modifications. Eventually, experiments involving CMs with iron NPs on the surface would be performed.

Further work is needed to determine the effect the concentration of sensitisation and activation solutions have on the nucleation of metallic particles at the carbon surface. Qualitative observes via SEM gave a reasonable trend as discuss in chapter 4. However, TGA experiments on carbon particles after the various steps of the sensitisation, activation and ED should quantify these qualitative observations. This experiment could also be used to find the maximum metal particle loading for the composites using the protocols in this report.

Future work could be performed on the Ag/C material in order to determine if there is a capping agent present on the nanoparticle surface and the nature of any possible capping agent present. SERS experiments could potentially show the presence of any organic capping layer on the AgNP. In fact preliminary results in our group have indicated the presence of organic materials on the AgNPs in SERS experiments. Further work also needs to be done on why the activity of the AgNPs in our composite is less than unsupported NPs. Two possibilities were identified, reduced surface area access due to particles clustering and reduced access to the surface due to a capping layer. The first could be confirmed by running kinetic experiments at various metallic loadings. As all the particles are the approximately the same size and the reaction is a surface reaction, increased loading should have linear relationship with the normalised rate constant for the reaction, if clustering is not having an influence. Work needs to be done on to determine whether sodium borohydride reduces the oxidised

polyphenols, removing the capping layer in the nitrophenol reduction reactions. Immersing the composite in borohydride, followed by washings should open up the particle surface if this is the case. Further experiments by re-immersion in a metal solution, followed by coffee would confirm this if particle growth occurred. If borohydride does indeed clean the NP surface, it would allow the Ag/C surface to be cleared for Subsequent kinetic experiments. This would give insight into whether the capping layer is affecting the rate constant of the nitrophenol reduction reaction, explaining the reduced performance when compared to the unsupported NPs.

Further work could be done on proving the stated hypothesis on the source of the homogenous particles observed in Method A synthesis of the $Fe/Fe_xO_y/C$ composite. By running a control experiment with no hypophosphite present, it could potentially be shown that homogenous processes are readily occurring separate to heterogeneous processes which require a reducing agent. Running the ED bath at a pH of 9.5 instead of 10.5 could potentially limit the homogeneous processes, assuming precipitation of Fe^{2+} in a basic medium is the cause of excess particles. This could also support the hypothesis previously stated. If the homogeneous processes can be reduced enough, characterisation and activity experiments can be performed on the resultant composite to determine its potential as a reductive remediant.

Further work can be done on the characterisation of the $Fe/Fe_xO_y/C$ synthesised using method B. An XRD measurement needs to be done on the composite material with the material remaining in an inert atmosphere at all times. This will allow us to more accurately determine the composition of the metal/carbon material, supporting the XANES results which confirmed the presence of Fe^0.

Important future work needs to be done on the activity of the Fe/Fe_xO_y NPs. The experiments performed in this work were inconclusive on whether Fe^0 had a role in the removal of Cr(VI). Removal experiments performed on Nitrate as a contaminant would provide more insight into this as nitrate is removed more efficiently by Fe^0 than

Iron oxide phases. Figure 6.1 below shows preliminary results for nitrate removal using the $Fe/Fe_xO_y/C$ material and pristine CMs.

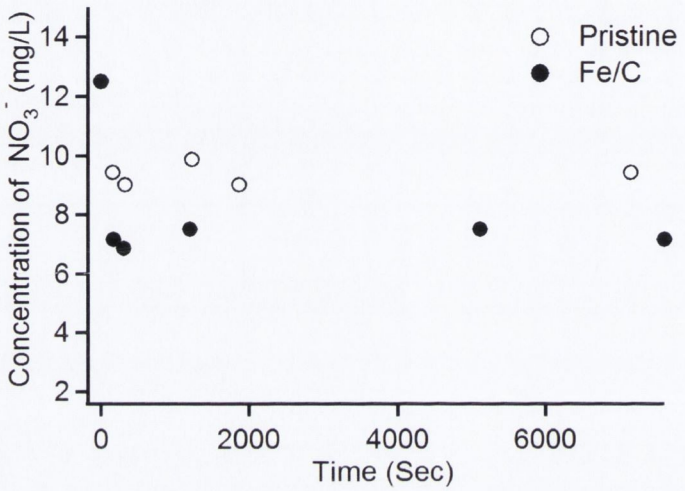

Figure 6.1: Removal of nitrate from aqueous solutions by $Fe/Fe_xO_y/C$ and pristine CMs

The figure shows promising results. Similar to the Cr(VI), the carbon surface adsorps some of the contaminant material as can be seen in the figure by the black dot series. The CMs removed 2.5 - 3 mg/L in the experiments above. However the composite material removed 5 - 5.5 mg/L after 4.5 h, 2.5 mg/l more than the pristine CMs. However, much more work needs to be performed to verify these results and obtain more accurate data. The results of these kinetic experiments coupled with XRD experiment mentioned above could have great implications for the potential applications of the composite material. The number of different contaminant species which can be potentially treated by this composite is greatly dependant on whether a significant amount of Fe^0 is present in the material. Therefore, these experiments are of particular importance moving into the future for any work done on the Fe/Fe_xO_y composite material.